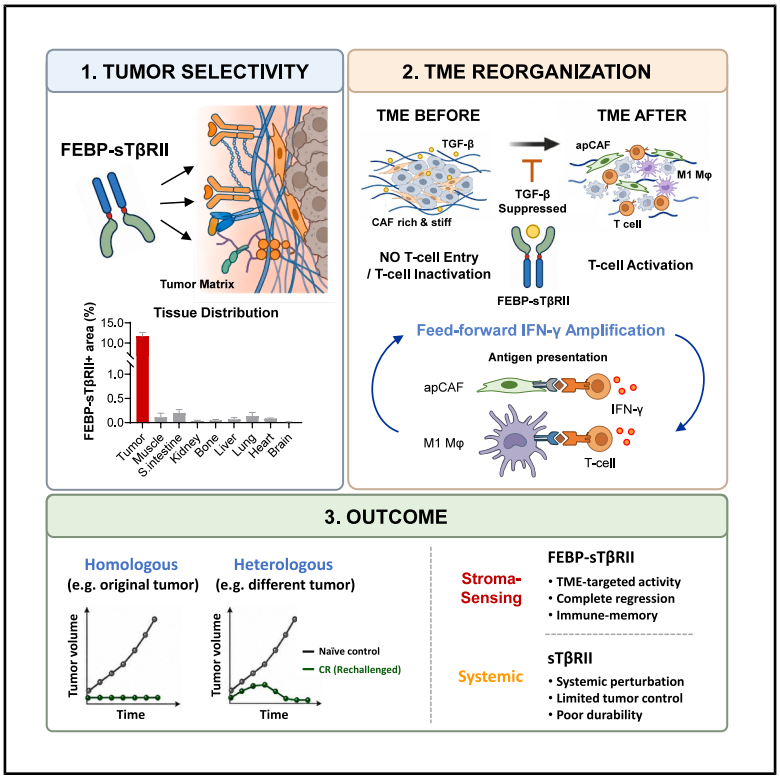
Cancer Cell

Article

A stroma-sensing TGF-β blockade reprograms CAF-myeloid niches to induce durable tumor immunity

Graphical abstract



Highlights

- FEBP-sTβRII anchors to FN-EDB-rich matrix to create a local TGF-β trap
- Matrix-targeted TGF-β blockade overcomes fibrotic immune exclusion
- IFN-γ feedback rewires CAF-myeloid niches into antigen-presenting hubs
- FEBP-sTβRII induces durable, cross-protective antitumor immunity

Authors

Dong Woo Kang, Jin Beom Bae, Seonho Yoo, ..., Junil Kim, John J. Letterio, Seong-Jin Kim

Correspondence

jasonsjkim@medpacto.com

In brief

Kang et al. show that anchoring a soluble TGF-β trap (FEBP-sTβRII) to FN-EDB-rich matrix overcomes fibrotic immune exclusion. This localized blockade drives IFN-γ-dependent CAF-myeloid reprogramming, enhances T cell infiltration, and establishes durable, cross-protective antitumor immunity.

Kang et al., 2026, Cancer Cell *44*, 2227–2248
November 9, 2026 © 2026 The Authors. Published by Elsevier Inc.
https://doi.org/10.1016/j.ccell.2026.10.007

CellPress

Cancer Cell

CellPress
OPEN ACCESS

Article

A stroma-sensing TGF-β blockade reprograms CAF-myeloid niches to induce durable tumor immunity

Dong Woo Kang,[1] Jin Beom Bae,[1] Seonho Yoo,[1] Hyejin Kim,[1] Pyunggang Kim,[2] Jaewoo Mo,[3] Jinhwan Kim,[1] Jin Su Kim,[1] Kwiyeom Yoon,[1] Ye Seon Kim,[1] Jeong Su Lee,[1] June Myoung Kim,[1] Min Gi Kang,[1] Min Jung Lee,[1] Changwon Lim,[4] Isaac Y. Kim,[5] Chang Pyo Hong,[6] Junil Kim,[3] John J. Letterio,[7,8] and Seong-Jin Kim[1,2,5,7,9,*]

[1]MedPacto, Inc., Seoul, Republic of Korea
[2]GILO Institute, GILO Foundation, Seoul, Republic of Korea
[3]Department of Bioinformatics, Soongsil University, Dongjak-gu, Seoul, Republic of Korea
[4]Department of Applied Statistics, Chung-Ang University, Seoul, Republic of Korea
[5]Department of Urology, Yale School of Medicine, New Haven, CT, USA
[6]YiPSCELL Inc., Seoul, Republic of Korea
[7]Department of Pediatrics, Case Western Reserve University, Cleveland, OH, USA
[8]The Case Comprehensive Cancer Center, Case Western Reserve University School of Medicine, Cleveland, OH, USA
[9]Lead contact
*Correspondence: jasonsjkim@medpacto.com
https://doi.org/10.1016/j.ccell.2026.10.007

SUMMARY

Transforming growth factor β (TGF-β) accumulation in the tumor microenvironment (TME) is a major barrier to durable antitumor immunity. We developed fibronectin extra domain B (FN-EDB)-binding peptide (FEBP)-soluble TβRII-Fc (sTβRII), an engineered inhibitor targeting the FN-EDB-rich tumor matrix for localized TGF-β blockade. In fibrotic, immune-excluded tumors, FEBP-sTβRII suppresses TGF-β/SMAD signaling to unleash T cell activation and IFN-γ production, thereby driving feedforward cancer-associated fibroblast (CAF)-myeloid reprogramming toward an antigen-presenting state. This coordinated remodeling relieves immune exclusion and converts the fibrotic TME into an antigen-visible ecosystem that sustains robust T cell infiltration and activation. Consequently, FEBP-sTβRII induces T cell-dependent tumor regression, expands effector-memory populations, and elicits long-term, cross-protective antitumor immunity, while minimizing peripheral transcriptional disturbances compared with systemic sTβRII. Together, these findings show that spatially targeted TGF-β blockade overcomes fibrotic immune exclusion to establish durable local and systemic tumor immunity.

INTRODUCTION

While immune checkpoint inhibitors (ICIs) significantly improve survival in some patients, most patients do not respond to these treatments.[1,2] A principal barrier is the immunosuppressive, fibrotic tumor microenvironment (TME), in which an expanded extracellular matrix (ECM) limits immune cell infiltration and drug penetration, while reinforcing tolerogenic cancer-associated fibroblasts (CAFs), myelosuppressive myeloid cells, and regulatory T cells (Treg). Among stromal cytokines, transforming growth factor β (TGF-β) functions as the dominant architect of this niche, driving myofibroblast differentiation and collagen deposition, suppressing matrix remodeling, and broadly dampening antitumor immunity, thereby providing a strong rationale for combining TGF-β blockade with ICIs.[3–11]

However, systemic TGF-β antagonists (e.g., kinase inhibitors, ligand traps, or soluble receptors) have shown inconsistent efficacy and dose-limiting toxicities and often fail to demonstrate a clear benefit over ICIs alone in randomized clinical trials.[12] A possible explanation for this failure is that signaling mediated by the high levels of TGF-β1 secreted by cancer tissues is not sufficiently suppressed in the TME by systemic TGF-β inhibitors at safe doses. This limitation has necessitated the development of TGF-β inhibitors that effectively target the TME.

Pancreatic ductal adenocarcinoma (PDAC) exemplifies the clinical need for such an approach: it is encased in a dense desmoplastic stroma populated by heterogeneous CAFs including myofibroblastic (myoCAF), inflammatory (iCAF), vascular (vCAF), and antigen-presenting (apCAF) states, each imposing distinct immunologic consequences.[13] apCAFs can license T cell responses in some contexts but, depending on ontogeny and cues, also promote Treg differentiation, underscoring how stromal state tunes tumor immunity.[14,15] Moreover, CAFs can directly engage deletional checkpoints (e.g., PD-L2-PD-1 and

This is an open access article under the CC BY license (http://creativecommons.org/licenses/by/4.0/).

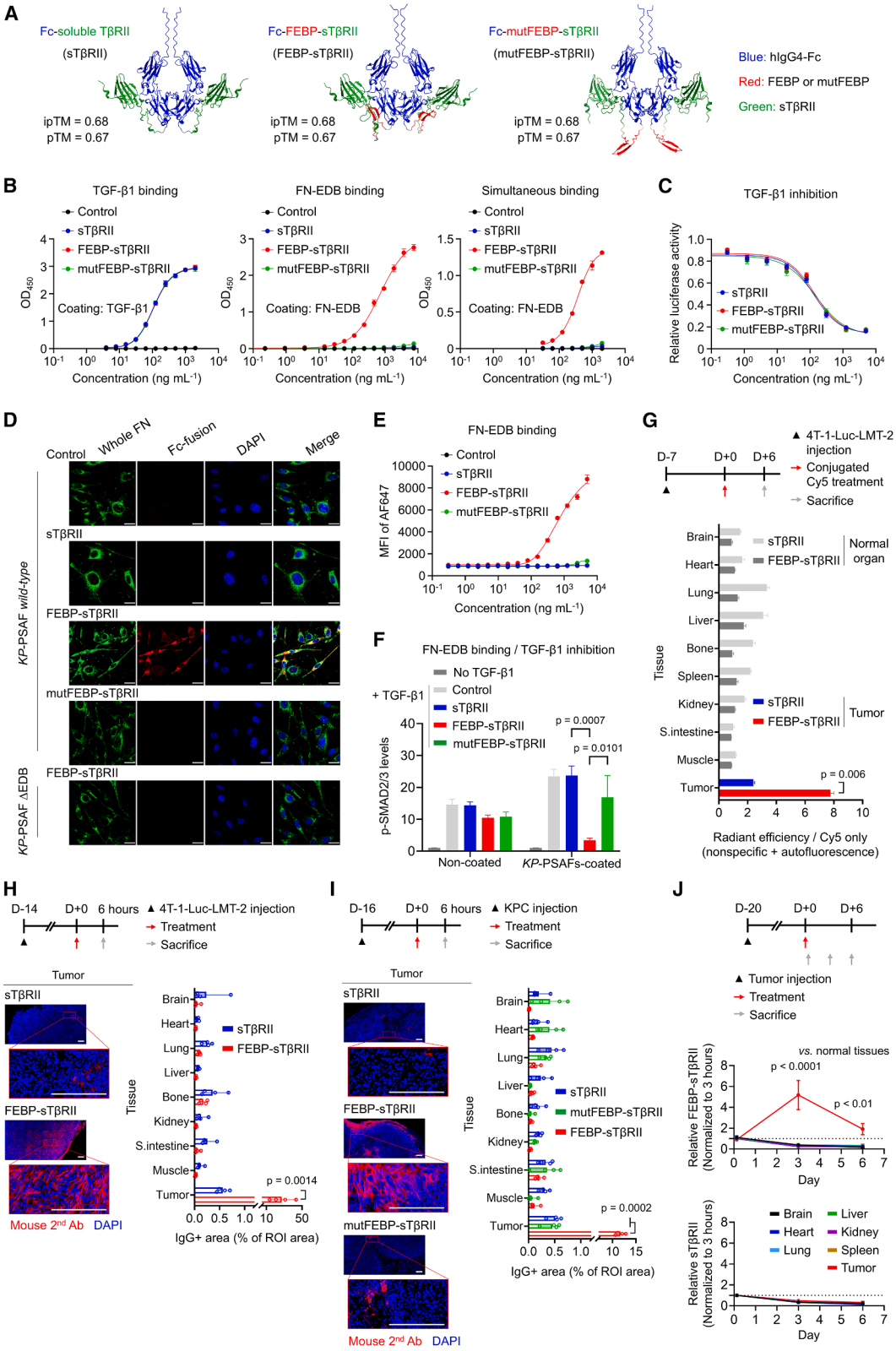


Figure 1. FEBP-sTβRII fusion proteins for tumor ECM-targeted TGF-β inhibition

(A) Schematic of FEBP-sTβRII format design, incorporating FEBP and the sTβRII at various positions relative to the Fc-region. The sTβRII and mutFEBP-sTβRII serve as controls. ipTM and pTM scores indicate the structural confidence of the predicted models.

(legend continued on next page)

FASL-FAS), coupling antigen handling to CD8$^+$ T cell attrition.[16] Together, these insights suggest that a TME-sensing TGF-β trap that accumulates within ECM-rich niches may (1) more effectively neutralize stromal TGF-β, (2) collapse myofibroblastic programs that enforce T cell exclusion, and (3) re-wire CAF/myeloid-T cell interfaces toward productive priming and recall.

In this study, we designed and characterized FEBP-sTβRII, a soluble TβRII-Fc fused to a fibronectin extra domain B (FN-EDB)-binding peptide (FEBP) that selectively accumulates in the fibroblast matrix to neutralize TGF-β *in situ*. Because most clinical TGF-β inhibitors act systemically and fail to function optimally within the ligand-rich TME, we hypothesized that anchoring a TGF-β inhibitor primarily to the tumor ECM would convert immunologically "cold" tumors into "hot" tumors, while limiting systemic pharmacodynamic engagement. Consistent with this hypothesis, our spatial targeting strategy demonstrated that restricting TGF-β inhibition to the TME is essential for unlocking the full therapeutic potential of TGF-β1 blockade without causing extensive peripheral transcriptional engagement.

RESULTS

"TME-sensing" FEBP-sTβRII effectively accumulates within the TME

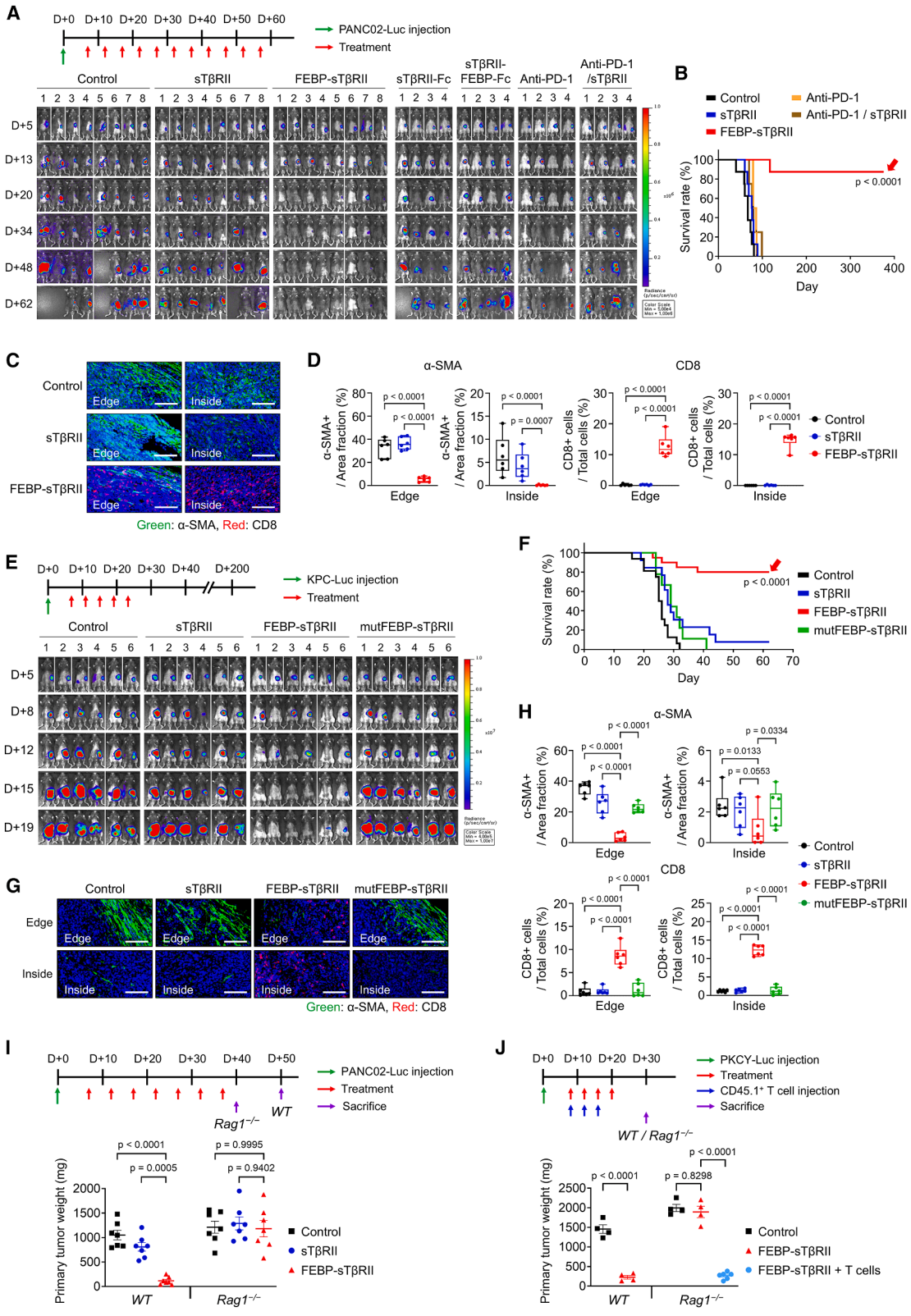
To develop TGF-β inhibitors capable of tumor-targeted delivery, we engineered several bispecific formats by fusing a synthetic soluble TβRII-Fc protein with one or more EDB-binding peptides (AP-T^{EDB}). These peptides were designed to specifically sense the alternatively spliced EDB of fibronectin, which is uniquely enriched in the ECM of the TME but virtually absent from normal adult tissues[17–19] (Figure S1A). Crucially, both the ligand-binding domain of TβRII and its ligand, TGF-β1, exhibit high evolutionary conservation across species, as does FN-EDB. Reflecting its clinical relevance, FN-EDB is markedly upregulated in multiple syngeneic mouse tumor models, aligning with The Cancer Genome Atlas (TCGA) profiles of human cancers (Figures S1B–S1E).

Structural modeling using AlphaFold3 demonstrated that positioning the FEBP between the hIgG4-Fc and sTβRII domains (Fc-FEBP-sTβRII) facilitates a distinct parallel β sheet-like alignment with FN-EDB, supported by low prediction errors in the predicted aligned error (PAE) plots (Figure S1A). Dimer predictions for all formats yielded moderate pTM (predicted TM-score) and ipTM (interface predicted TM-score) (~0.7), supporting confidence in the predicted models (Figure 1A). Due to its superior expression yield and minimal aggregation (Figures S1F and S1G), Fc-FEBP-sTβRII (FEBP-sTβRII) was selected as a clinical drug candidate. sTβRII lacking FEBP and mutFEBP-sTβRII with attenuated FN-EDB affinity were used as controls. Enzyme-linked immunosorbent assay (ELISA) demonstrated that sTβRII, FEBP-sTβRII, and mutFEBP-sTβRII exhibited comparable TGF-β1 binding and inhibitory activity (Figures 1B and 1C). However, only FEBP-sTβRII bound to FN-EDB and simultaneously engaged FN-EDB and TGF-β1 (Figure 1B). FN containing EDB is predominantly expressed *in vivo* by proliferating or activated fibroblasts and is deposited in the ECM. *K-Ras^{LA1}/TP53$^{-/-}$* primary sarcoma-associated fibroblasts (*KP*-PSAFs) serve as valuable platforms to characterize FN-EDB *in vitro* (Figure S1H). Co-immunostaining of *KP*-PSAFs confirmed recognition of FN-EDB by FEBP-sTβRII but not in FN-EDB-knockout *KP*-PSAFs. No interaction was observed between mutFEBP-sTβRII and FN-EDB (Figure 1D). FEBP-sTβRII stably bound to FN-EDB at concentrations above 100 ng/mL, whereas sTβRII and mutFEBP-sTβRII did not bind (Figure 1E). Consistent with these findings, FEBP-sTβRII markedly inhibited SMAD2/3 phosphorylation only in *KP*-PSAF-coated plates, whereas sTβRII and mutFEBP-sTβRII showed little or no effect (Figure 1F). To evaluate tumor localization, FEBP-sTβRII and control proteins were assessed in orthotopic tumor models. In long-term retention studies, FEBP-sTβRII exhibited significantly greater tumor accumulation than sTβRII in 4T-1-Luc-LMT-2 tumors (Figure 1G). In early distribution studies, FEBP-sTβRII showed enhanced intratumoral penetration in both 4T-1-Luc-LMT-2 and KPC tumors, whereas sTβRII and mutFEBP-sTβRII displayed limited tumor localization and a diffuse, nonspecific distribution in normal organs (Figures 1H, 1I, S1I, and S1J). Consistent with these findings, FEBP-sTβRII was retained in tumors for several days after administration, whereas tumor retention of sTβRII remained minimal (Figure 1J).

FEBP-sTβRII inhibits tumor growth and metastasis in ICI-resistant orthotopic breast and pancreatic cancer models

To evaluate *in vivo* antitumor efficacy, we first tested FEBP-sTβRII in the FN-EDB-high 4T-1-Luc-LMT-2 mouse breast

(B) ELISA for binding of control, sTβRII, FEBP-sTβRII, and mutFEBP-sTβRII with TGF-β1, FN-EDB, and simultaneous binding (n = 3; 3 technical replicates).
(C) CAGA12-Luc reporter assay of TGF-β-SMAD inhibition by sTβRII, FEBP-sTβRII, and mutFEBP-sTβRII (n = 3; 3 technical replicates).
(D) Immunofluorescence of whole FN (green) and the indicated Fc-fusion proteins (red) in *KP*-PSAFs with high FN-EDB expression, as well as in *FN-EDB*-depleted *KP*-PSAFs (n = 4; scale bars: 10 μm).
(E) Flow cytometric analysis of Fc-fusion protein binding to FN-EDB$^+$ *KP*-PSAFs, shown as the mean fluorescence intensity (MFI; n = 2; 3 technical replicates).
(F) p-SMAD2/3 inhibition assay in 4T-1-Luc-LMT-2 cells cultured with or without *KP*-PSAF-coated plates for 16 h, treated with control or indicated Fc-fusion proteins (6 h), and stimulated with TGF-β1 (5 ng/mL) for 1 h. p-SMAD2/3 was assessed by flow cytometry (n = 3).
(G) *In vivo* Cy5 fluorescence in organs and tumors from 4T-1-Luc-LMT-2 tumor-bearing mice following 6 days of administration with Cy5-labeled constructs was quantified (n = 3).
(H and I) Immunofluorescence analysis of the distribution of the indicated Fc-fusion proteins in tumors and multiple normal tissues from 4T-1-Luc-LMT-2 (H) and KPC-Luc (I) tumor-bearing mice, 6 h after intravenous injection at tumor sizes of 200–300 mm^3 (n = 4/group; scale bars: 200 μm). Each point represents one mouse (≥3 ROIs averaged per mouse).
(J) Time-course analysis of FEBP-sTβRII (n = 4/time point) and sTβRII (n = 3/time point) retention in tumors and normal organs. Values are normalized to the 3-h signal.
Data are presented as mean ± SD; two-way repeated-measures (RM) ANOVA (F–I; log-transformed for H and I) or two-way ANOVA (J), both with Šidák's correction.
See also Figures S1 and S8.



(legend on next page)

cancer model, which recapitulates the aggressive and highly metastatic features of triple-negative breast cancer (TNBC) (Figure S2A). FEBP-sTβRII significantly suppressed primary tumor growth, completely prevented lung metastasis, and prolonged overall survival; in contrast, systemic sTβRII, conventional ICIs, and their combination formats showed little to no therapeutic benefit (Figures S2B–S2D). Consistent with its tumor-selective localization (Figures 1G and 1H), FEBP-sTβRII markedly reduced α-SMA expression at the tumor edges, increased $CD8^+$ T cell infiltration, and robustly suppressed p-SMAD2/3 levels both at the tumor edge and within the tumor inside (Figures S2E and S2F). These results demonstrate that FEBP-sTβRII disrupts the CAF-driven stromal barrier in immune-resistant TNBC, thereby enabling immune cell infiltration into the TME.

A recent report showed that the TGF-β blockade effectively promotes TME remodeling by reducing CAF activation and alleviating stromal-induced barriers in a mouse PDAC model.[20] Therefore, we next investigated the therapeutic efficacy of FEBP-sTβRII in the PANC02 orthotopic transplant model, which exhibits minimal T cell infiltration, a dense ECM, and ICI resistance, driven by a SMAD4 impairment that strongly biases TGF-β biology toward stromal and immune suppression rather than canonical epithelial growth restraint.[21–23] FEBP-sTβRII significantly inhibited tumor growth and dramatically prolonged survival compared with the control, sTβRII, anti-PD-1 antibody, or their combination groups (Figures 2A and 2B). In contrast, Fc-sTβRII, referred to here as sTβRII, and the reverse-orientation sTβRII-Fc format showed limited activity, indicating that Fc-fused systemic TGF-β trapping alone was insufficient to overcome this immune-excluded PDAC model. The alternative sTβRII-FEBP-Fc topology, in which the sTβRII-FEBP module is positioned N terminally relative to Fc, showed minimal tumor growth suppression in the imaging-based efficacy screen and was not advanced to survival analysis (Figure 2A). These findings suggest that FEBP-sTβRII activity may be influenced by Fc-centered fusion topology, although further structure-function studies are needed to define how molecular orientation affects FN-EDB-dependent tumor retention and local TGF-β neutralization.

Histological analysis of tumors treated with FEBP-sTβRII revealed a marked decrease in α-SMA expression, particularly at the tumor edges ($p < 0.0001$), a significant increase in the total number of $CD8^+$ T cells in both the edge and the inside of tumors ($p < 0.0001$), and a strong suppression of p-SMAD2/3 levels in both regions ($p < 0.0001$) (Figures 2C, 2D, and S3A). Additional PANC02-Luc studies confirmed dose-dependent tumor suppression by FEBP-sTβRII, with clear antitumor activity emerging from 15 mg/kg and the most durable efficacy observed at 30 mg/kg, whereas mutFEBP-sTβRII failed to reproduce this pattern, even at increased doses (Figure S3B). Co-administration of the sTNFR2 fusion protein reduced the activity of FEBP-sTβRII, supporting the involvement of TNF-α-mediated inflammatory immune responses (Figure S3B). FEBP-sTβRII also reduced intratumoral TGF-β1 levels, consistent with local TGF-β pathway suppression within the TME (Figure S3C).

We next evaluated FEBP-sTβRII in two aggressive, SMAD4-intact KRAS/TP53-driven orthotopic PDAC models that recapitulate key features of human PDAC, PKCY-Luc (*Pdx1-cre;LSL-K-Ras$^{G12D/+}$;TP53$^{fl/+}$;R26^{YFP}*) and KPC-Luc (*Pdx-1-Cre;LSL-Kras$^{G12D/+}$;LSL-TP53$^{R172H/+}$*) in which canonical epithelial TGF-β tumor-suppressive circuitry may be preserved unlike in SMAD4-impaired PANC02 tumors.[24]

Both models exhibited rapid tumor progression in the control and systemic sTβRII-treated mice, whereas FEBP-sTβRII induced profound tumor regression. In PKCY-Luc tumors, a complete regression (CR) rate of 75% was achieved by day 30. Similarly, in KPC-Luc tumors, CR was observed in 4 of 6 mice by day 19, whereas sTβRII and the non-binding control, mut-FEBP-sTβRII, failed to replicate this therapeutic efficacy (Figures 2E and S3D).

This robust tumor control translated into a durable, long-term survival benefit in both models. In the PKCY-Luc model, over 90% of control and sTβRII-treated mice succumbed to disease within 10 days of treatment discontinuation; in stark contrast, 87.5% (7/8) of FEBP-sTβRII-treated mice remained

Figure 2. FEBP-sTβRII suppresses tumor growth and prolongs survival in ICI-refractory pancreatic cancer by remodeling stroma and enhancing $CD8^+$ T cell infiltration

(A–D) PANC02-Luc orthotopic model. Mice were treated with control, sTβRII (Fc-sTβRII), sTβRII-Fc, FEBP-sTβRII (Fc-FEBP-sTβRII), sTβRII-FEBP-Fc, anti-PD-1, or anti-PD-1 + sTβRII (n = 4–8/group).

(A) Tumor progression was monitored by bioluminescence imaging following treatments initiated on day 7 and administered every 5 days.

(B) Kaplan-Meier survival analysis.

(C and D) Immunofluorescence images and quantification of α-SMA (green) and $CD8^+$ T cells (red) in the tumor edge and inside regions of PANC02-Luc tumors after control, sTβRII, or FEBP-sTβRII treatment (n = 6; scale bars: 100 μm).

(E–H) KPC-Luc orthotopic model. Mice were treated with control (n = 16/group), sTβRII (n = 13/group), FEBP-sTβRII (n = 20/group), or mutFEBP-sTβRII (n = 9/group).

(E) Treatments were initiated on day 7 and administered every 4 days. Tumor progression was monitored by bioluminescence imaging.

(F) Kaplan-Meier survival analysis.

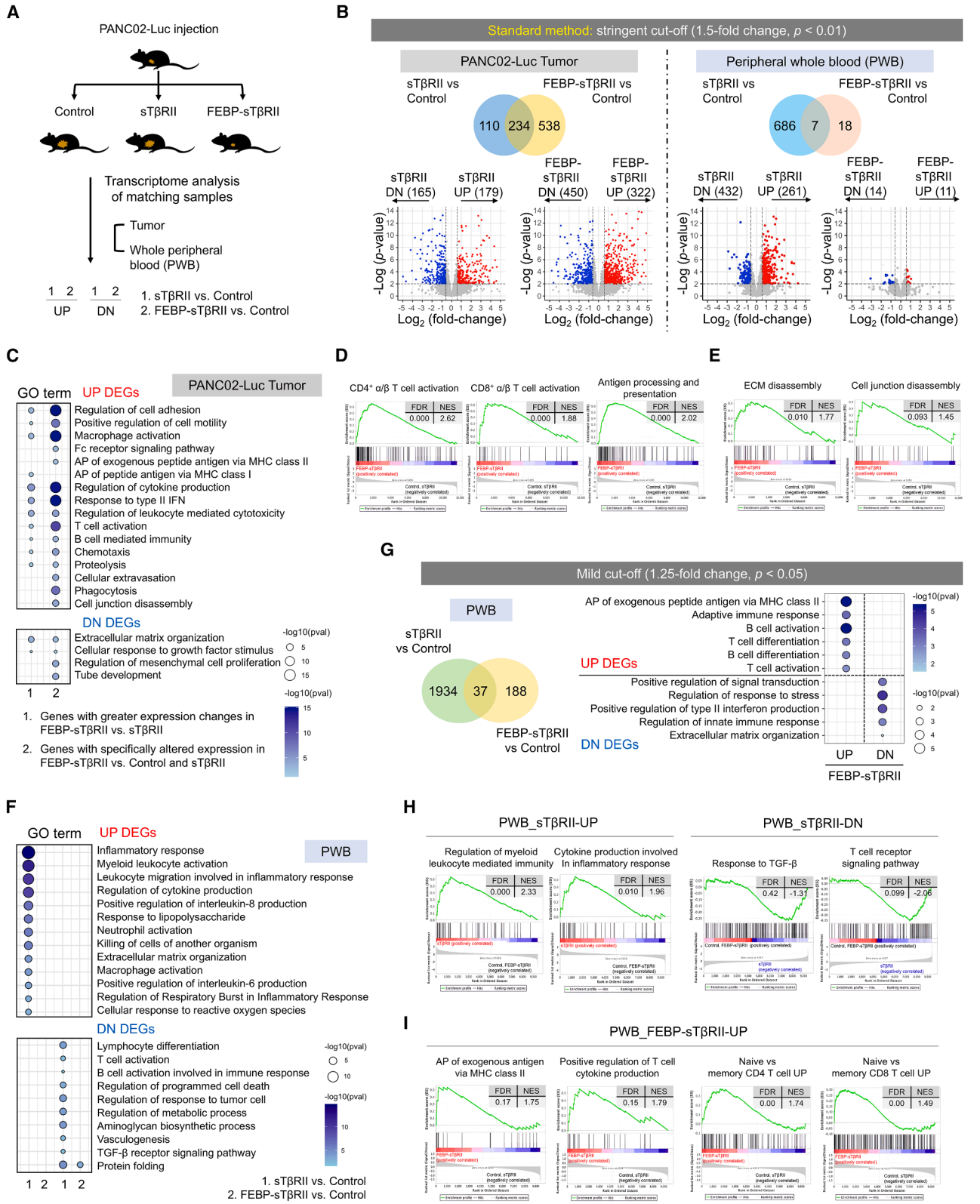
(G and H) Immunofluorescence images and quantification of α-SMA (green) and $CD8^+$ T cells (red) in the tumor edge and inside regions of KPC-Luc tumors (n = 6; scale bars: 100 μm).

(I) Comparison of PANC02 tumor weight in wild-type and *Rag1*$^{-/-}$ mice treated with FEBP-sTβRII. Treatment was started on day 7 at 5-day intervals, and mice were sacrificed on days 50 and 40, respectively (n = 7/group).

(J) Comparison of PKCY-Luc tumor weight in wild-type and *Rag1*$^{-/-}$ mice treated with FEBP-sTβRII with or without adoptive transfer of $CD45.1^+CD3^+$ T cells (4×10^6/mouse, n = 4/group, except the T cell transfer group, n = 6).

Data are presented as mean ± SD; log-rank (Mantel-Cox) test with Holm-Šidák-adjusted pairwise comparisons (B and F); Šidák's multiple comparisons following one-way ANOVA on square-root-transformed data (D and H), two-way ANOVA (I), or one-way ANOVA (J). Each point represents one mouse (≥3 ROIs averaged per mouse) (D and H).

See also Figures S2 and S3.



(legend on next page)

alive at 327 days post-treatment (270 days after drug cessation), with no further deaths observed to date (Figure S3E). Likewise, in the KPC-Luc model, more than 75% of control, sTβRII-treated, and mutFEBP-sTβRII-treated mice died within 10 days of treatment cessation, whereas FEBP-sTβRII markedly delayed progression and significantly prolonged survival (Figure 2F). Together, these data demonstrate that FEBP-sTβRII can induce exceptional, durable tumor control, even in highly aggressive, KRAS/TP53-driven, and SMAD4-intact PDAC models.

Consistent with our findings in the PANC02-Luc model, the antitumor activity of FEBP-sTβRII in KPC-Luc and PKCY-Luc tumors was accompanied by a profound spatial remodeling of the stromal-immune barrier. FEBP-sTβRII virtually eliminated α-SMA expression along the invasive tumor margins, enhanced $CD8^+$ T cell infiltration throughout the tumor parenchyma, and robustly suppressed p-SMAD2/3 signaling across all tumor regions; in contrast, sTβRII and mutFEBP-sTβRII exerted limited or incomplete remodeling activity (Figures 2G, 2H, and S3F–S3I). Whole-tumor α-SMA/CD8 density mapping further confirmed that FEBP-sTβRII uniquely induced broad stromal relaxation, which correlated with the intratumoral redistribution of $CD8^+$ T cells (Figure S3G).

To establish the immune-dependent efficacy of FEBP-sTβRII, PANC02-Luc and PKCY-Luc tumors were evaluated in *Rag1*$^{-/-}$ and wild-type mice. FEBP-sTβRII failed to suppress tumor growth in *Rag1*$^{-/-}$ mice but retained robust antitumor activity in immunocompetent wild-type controls (Figures 2I and 2J). Crucially, the adoptive transfer of $CD45.1^+$ naive T cells into FEBP-sTβRII-treated *Rag1*$^{-/-}$ mice fully restored the therapeutic efficacy. This demonstrates that stromal remodeling alone is insufficient and that T cell-mediated adaptive immunity is indispensable for the therapeutic activity of FEBP-sTβRII (Figure 2J).

In orthotopic PKCY-Luc tumors, FEBP-sTβRII dose dependently reduced tumor weight, while combination with anti-PD-1 therapy achieved near-complete tumor eradication (Figure S3J). Together, these findings establish that FN-EDB-targeted TGF-β blockade overcomes stromal immune exclusion through local p-SMAD2/3 suppression, $\alpha\text{-SMA}^+$ stromal remodeling, $CD8^+$ T cell infiltration, and adaptive antitumor immunity and sensitizes checkpoint-refractory PDAC to PD-1 blockade.

FEBP-sTβRII drives tumor-localized stromal-immune remodeling with limited peripheral disturbance

Next, we performed transcriptome analyses of tumors and peripheral whole blood (PWB) from PANC02-Luc-bearing mice to compare the transcriptional effects of TME-sensing FEBP-sTβRII and systemic sTβRII in tumors and normal tissues (Figures 3A and 3B). In tumors, FEBP-sTβRII induced a broader transcriptional response than sTβRII, yielding 772 differentially expressed genes (DEGs) relative to 344, with 234 DEGs shared between them (Figure 3B; Table S1A). Conversely, sTβRII treatment caused substantial systemic perturbation in PWB (693 DEGs), whereas FEBP-sTβRII altered only 25 genes (7 shared), indicating a substantially narrower peripheral transcriptional footprint (Figure 3B; Table S1B).

In the tumor transcriptome, DEGs (Table S1A) were classified into three groups: genes common to both treatments (Figure S4A), genes with greater alterations under FEBP-sTβRII (Figure S4B), and FEBP-sTβRII-specific genes (Figure S4C). Pathway analysis revealed a coordinated remodeling of the immune and stromal programs. Genes showing greater alterations under FEBP-sTβRII were enriched in pathways associated with T cell and B cell activation, inflammatory responses, MHC class I antigen presentation, type-II interferon (IFN) signaling, and protein degradation. Conversely, FEBP-sTβRII-specific genes were uniquely enriched in pathways related to Fc-receptor signaling, MHC class II (MHC-II) antigen presentation, extravasation, phagocytosis, and ECM/junction disassembly, while suppressing pathways associated with ECM organization, growth factor signaling, tube morphogenesis, and mesenchymal cell proliferation, consistent with the attenuation of TGF-β-driven stromal programs (Figure 3C; Table S1C). Gene set enrichment analysis (GSEA) confirmed this transcriptional architecture, showing the enrichment of T cell activation, antigen presentation, ECM/junction disassembly, and IFN-γ response programs, alongside the suppression of TGF-β, VEGF, hypoxia, Myc, E2F, mTOR, G2M checkpoint, and glycolysis pathways (Figures 3D and 3E; Table S1D).

Despite inducing potent antitumor reprogramming, FEBP-sTβRII exerted minimal impact on gene expression in PWB (Figure S4D; Table S1B). In PWB, sTβRII induced broad neutrophil/inflammatory transcriptional changes and reduced adaptive immune programs (Figure 3F; Table S1E). To detect subtle

Figure 3. FEBP-sTβRII selectively reprograms tumor ECM and immune gene signatures while minimizing peripheral transcriptional perturbation

(A) Paired transcriptomic profiling of PANC02-Luc tumors and peripheral whole blood (PWB) from C57BL/6J mice (n = 3/group) treated with control, sTβRII, or FEBP-sTβRII.

(B) Comparative DEG analysis of tumors (left) and PWB (right) treated with FEBP-sTβRII or sTβRII. Venn diagrams and volcano plots showing DEGs identified with a stringent cut-off versus control (n = 3/group).

(C) GO enrichment analysis of DEGs in PANC02-Luc tumors. AP, antigen processing/presentation; IFN, interferon.

(D and E) Representative GSEA plots of immune cell activation (D) and barrier remodeling and clearance (E) pathways enriched in FEBP-sTβRII-treated tumors relative to control and sTβRII.

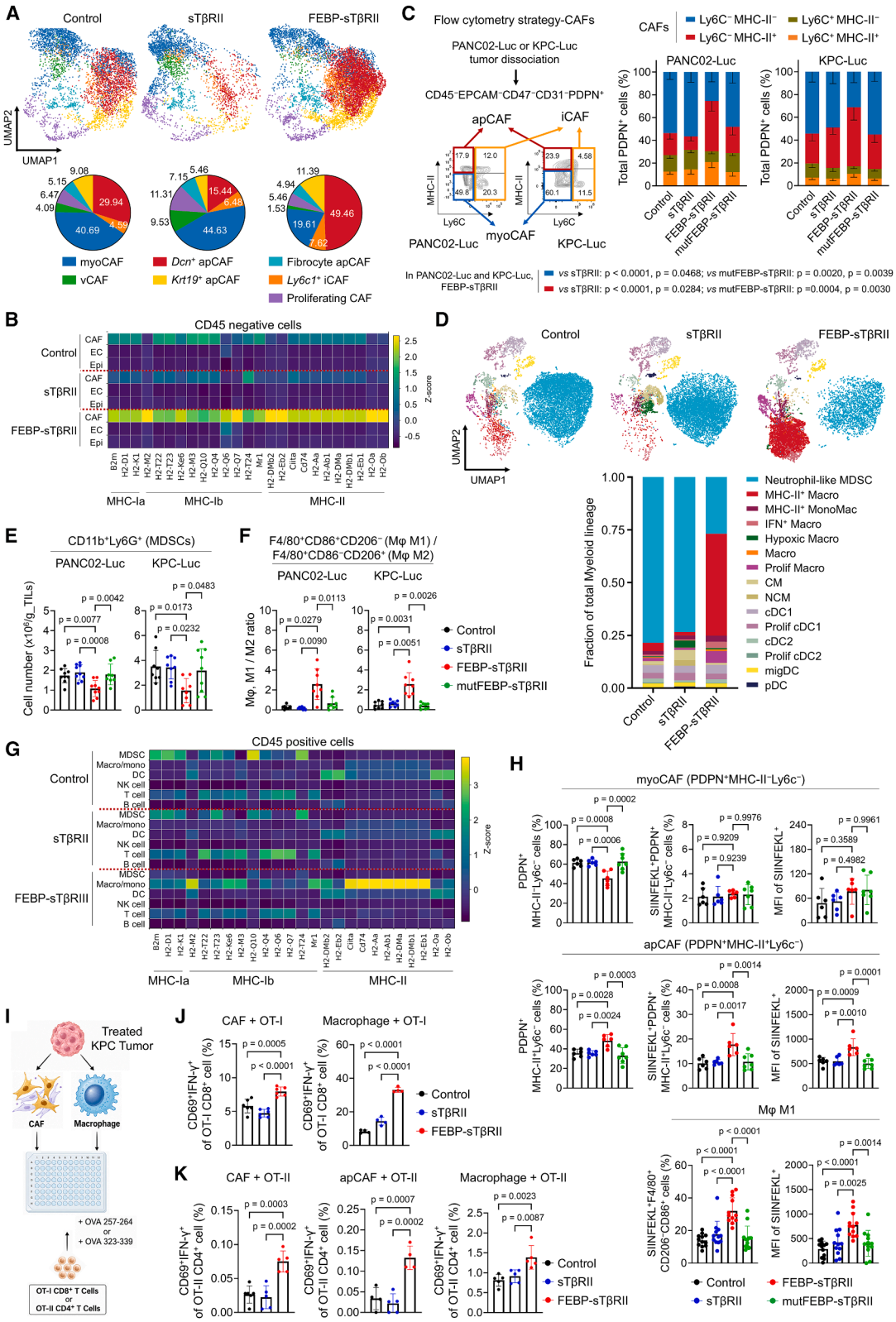
(F) GO term analysis of upregulated and downregulated genes in PWB from FEBP-sTβRII- and sTβRII-treated mice compared with control under a stringent cut-off.

(G) Venn diagrams showing DEGs in PWB identified with a mild threshold versus control for sTβRII and FEBP-sTβRII (n = 3/group). GO enrichment analysis was performed on FEBP-sTβRII-specific DEGs.

(H) Representative GSEA plots of PWBs from sTβRII-treated mice, showing representative upregulated (left) and downregulated (right) pathways.

(I) Representative GSEA plots showing enrichment of pathways and memory CD4/CD8 T cell signatures from ImmuneSigDB in PWB from FEBP-sTβRII-treated mice relative to control and sTβRII.

See also Figure S4 and Table S1.



(legend on next page)

PWB transcriptional changes, we applied a mild threshold (Figure S4E). Using this exploratory threshold, FEBP-sTβRII showed selective enrichment of adaptive immune and MHC class II programs without broad innate inflammatory activation (Figure 3G; Tables S1B and S1F). Consistent with the Gene Ontology (GO) analysis, GSEA revealed that sTβRII induced broad inflammatory activation, reduced T cell and B cell programs, and attenuated TGF-β signaling (Figure 3H; Table S1G). In contrast, FEBP-sTβRII selectively enriched T cell and MHC class II pathways, alongside immune-memory programs (Figure 3I; Table S1G).

To test whether the PANC02-derived pharmacodynamic program extends to a more aggressive PDAC setting, we performed bulk RNA sequencing (RNA-seq) on KPC-Luc tumors. Under a stringent threshold, FEBP-sTβRII-treated KPC-Luc tumors exhibited pathway-level remodeling highly consistent with the PANC02-Luc tumor response. FEBP-sTβRII enriched antigen presentation, IFN response, T cell activation, cytotoxicity, chemotaxis, and phagocytic/tissue-remodeling programs, while suppressing ECM, TGF-β response, mesenchymal, and angiogenic programs (Figures S4F and S4G; Tables S1H and S1I).

These findings define a TME-targeted pharmacodynamic profile distinct from that of systemic sTβRII across different PDAC models. Characterized by local suppression of stromal and TGF-β-driven programs alongside the promotion of immune activation and tissue remodeling, FEBP-sTβRII selectively reshapes the TME, while sparing the peripheral immune system from the broad transcriptional perturbations induced by systemic sTβRII.

Delivery of FEBP-sTβRII to the tumor site reshapes CAF-macrophage plasticity to establish antigen-presenting stromal-myeloid immunity

Because paired tumor/PWB RNA-seq established PANC02-Luc as a robust discovery model for tumor-localized pharmacodynamic remodeling, we performed single-cell RNA sequencing (scRNA-seq) on orthotopic PANC02-Luc tumors treated with control, sTβRII, or FEBP-sTβRII to define the cellular basis of FEBP-sTβRII-induced stromal-immune reprogramming. Integrated analysis resolved major immune, stromal, endothelial, and epithelial lineages (Figures S5A and S5B), and key findings were subsequently validated in KPC-Luc tumors.

Subclustering identified myoCAF, vCAF, *Dcn*$^{+}$-apCAF, *Krt19*$^{+}$-apCAF, fibrocyte-(like)-apCAF, *Ly6c1*$^{+}$-iCAF, and proliferating CAF states (Figure S5C). In control and sTβRII-treated tumors, myoCAFs predominated, consistent with an immune-excluded, matrix-enriched niche. In contrast, FEBP-sTβRII contracted the myoCAF compartment and expanded *Dcn*$^{+}$-apCAFs, with more modest increases in *Ly6c1*$^{+}$-iCAFs and *Krt19*$^{+}$-apCAFs (Figure 4A). FEBP-sTβRII also triggered substantial subset-specific transcriptional remodeling. In myoCAFs, genes associated with ECM deposition and stiffening and matrix-remodeling enzymes were significantly downregulated, consistent with the attenuation of stromal-barrier function (Figure S5D). Conversely, apCAFs, which strongly express IFN- or chemotaxis-responsive genes, were significantly upregulated by FEBP-sTβRII, whereas immune-inhibitory or compensatory mediators remained predominant in control or sTβRII-treated tumors (Figure S5E). Meanwhile, *Ly6c1*$^{+}$-iCAFs showed a modest increase in inflammation-, immunomodulation-, and migration-responsive genes, collectively suggesting a net shift toward an immunostimulatory stromal phenotype (Figure S5F). At the compartment level, pseudobulk profiling across CD45^{-} fractions demonstrated broad upregulation of MHC class Ia (*H2-K1/H2-D1/B2m*) and MHC class II (*H2-Aa/H2-Ab1/Cd74*) under FEBP-sTβRII (Figure 4B), indicating the acquisition of antigen presentation capacity within stromal compartments.

Because apCAF states can support either stimulatory immunity or tolerogenic immunity depending on context,[14,15] we next investigated whether FEBP-sTβRII preferentially induces an immunostimulatory CAF phenotype. *Dcn*$^{+}$-apCAFs, rather than *Krt19*$^{+}$-apCAFs, exhibited stronger IFN-responsive, costimulatory, and stromal-adhesion/matrix programs, consistent with an antigen-presenting-like stromal niche capable of T cell engagement (Figure S5G). Flow cytometry confirmed the expansion of apCAFs (Ly6C^{-}/MHC-II^{+}), with reciprocal contraction of myoCAFs (Ly6C^{-}/MHC-II^{-}) in both PANC02-Luc and KPC-Luc tumors (Figure 4C), demonstrating that this CAF transition is conserved in a genetically engineered, highly refractory PDAC model. Importantly, mutFEBP-sTβRII failed to recapitulate this CAF remodeling, indicating that FN-EDB-dependent matrix retention is strictly required for full stromal reprogramming.

Figure 4. FEBP-sTβRII converts CAF and myeloid compartments into antigen-visible immune-supportive niches

(A–K) Mice were treated with control, sTβRII, FEBP-sTβRII, or mutFEBP-sTβRII as indicated.

(A) UMAP of CAF-cluster and -subset proportions in orthotopic PANC02 tumors, delineating seven transcriptionally distinct CAF states.

(B) Heatmap of MHC class I/II gene expression across CAF, Epi, and EC compartments by pseudobulk analysis of scRNA-seq.

(C) Flow cytometry strategy for CAF phenotyping and quantification of myoCAF/apCAF/iCAF from PDPN^{+} parental gate in PANC02-Luc (n = 5/group) and KPC-Luc (n = 6/group) tumors.

(D) UMAP of tumor-infiltrating myeloid lineages in PANC02-Luc tumors, with proportional shifts in subsets (Macro, macrophage; Mono, monocyte; NCM, non-classical monocyte; CM, classical monocyte).

(E and F) Flow cytometric quantification of MDSCs per gram of tumor (E) and M1/M2 ratios (F) in PANC02-Luc and KPC-Luc tumors (n = 8–9/group; 3 technical replicates).

(G) Heatmap of MHC class I/II expression in CD45^{+} immune subsets across treatment groups by pseudobulk scRNA-seq analysis.

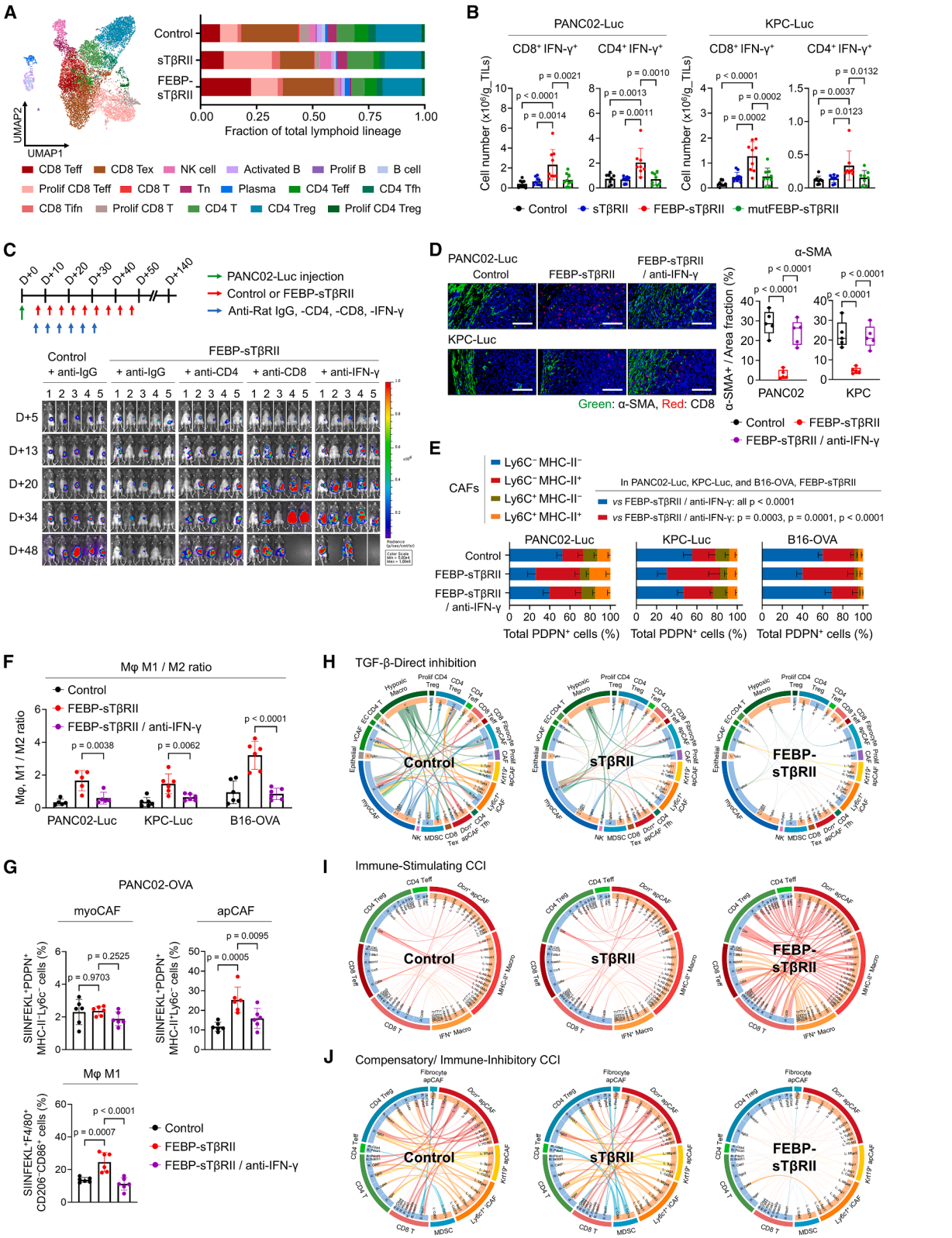
(H) Flow cytometric analysis of myoCAFs, apCAFs, and M1 macrophages in subcutaneous B16-OVA tumors after treatment. Population frequencies and H-2K^{b}-SIINFEKL^{+} cell percentage and MFI were quantified (CAFs, n = 6–7/group; macrophages, n = 12/group).

(I) Schematic of T cell co-culture assays using CAFs or macrophages sorted from treated KPC tumors.

(J and K) Following peptide pulsing, sorted cells were co-cultured with OT-I CD8^{+} T cells (OVA257–264; J) or OT-II CD4^{+} T cells (OVA323–339; K) overnight. CD69^{+}IFN-γ^{+} T cell frequencies were analyzed by flow cytometry (n = 4–6).

Data are presented as mean ± SD; statistical analyses were performed using one-way ANOVA (C, E, H, J, and K) or Welch's unpaired t tests (F), with Šidák-adjusted multiple comparisons.

See also Figures S5 and S8.



(legend on next page)

FEBP-sTβRII also markedly reshaped the tumor myeloid compartment compared with the control or sTβRII treatments. Uniform manifold approximation and projection (UMAP) clustering identified distinct myeloid states, including neutrophil-like myeloid-derived suppressor cells (MDSCs), as well as MHC-II$^+$, IFN$^+$, and hypoxic macrophages (Figure S5H). Control and sTβRII-treated tumors were dominated by neutrophil-like MDSCs, whereas FEBP-sTβRII reduced MDSCs and expanded MHC-II$^+$ and IFN$^+$-responsive macrophage states (Figure 4D).

MDSCs expressing immunosuppressive markers[25,26] were transcriptionally downregulated following FEBP-sTβRII treatment (Figure S5I). Furthermore, at the transcriptional level, FEBP-sTβRII enhanced macrophage antigen presentation and IFN response programs, while suppressing hypoxic and immunosuppressive macrophage features (Figure S5J). Flow cytometry confirmed this shift in both PANC02-Luc and KPC-Luc tumors, demonstrating reduced CD11b$^+$Ly6G$^+$ MDSCs and an increased M1/M2 macrophage ratio (F4/80$^+$CD86$^+$CD206$^-$ versus F4/80$^+$CD86$^-$CD206$^+$) after FEBP-sTβRII treatment (Figures 4E and 4F). Consistently, pseudobulk profiling across the CD45$^+$ immune compartment revealed elevated MHC class II expression on tumor macrophages/monocytes. It also showed a redistribution of MHC class I, characterized by reduced expression on MDSCs and enhanced expression on macrophages/monocytes (Figure 4G). H2-Ab1 immunohistochemistry further confirmed the enrichment of antigen-presenting programs in FEBP-sTβRII-treated tumors (Figure S5K).

To determine whether this CAF-myeloid remodeling translated into functional antigen presentation, we quantified surface H-2K^b–SIINFEKL in B16-OVA tumors.[27] FEBP-sTβRII reduced myoCAF abundance without increasing SIINFEKL presentation within the residual myoCAF population (Figure 4H). In contrast, it expanded apCAFs and markedly enhanced both the frequency of SIINFEKL$^+$ cells and the SIINFEKL mean fluorescence intensity (MFI) within apCAFs, with a similar enhancement observed in M1 macrophages. Crucially, these functional effects were not reproduced by mutFEBP-sTβRII, confirming that FN-EDB-dependent matrix retention is required for the induction of these antigen-presenting stromal and myeloid states (Figure 4H).

Moreover, we tested whether CAFs and macrophages remodeled by FEBP-sTβRII could functionally stimulate antigen-specific T cells. Total CAFs, apCAFs, and macrophages were sorted from treated tumors, peptide-pulsed, and co-cultured with OT-I or OT-II T cells to test antigen-presenting function[14,28,29] (Figure 4I). CAFs and macrophages from FEBP-sTβRII-treated tumors induced significantly higher frequencies of CD69$^+$IFN-γ$^+$ OT-I CD8$^+$ T cells than those from control- or sTβRII-treated tumors, whereas vehicle control conditions without antigen loading showed minimal T cell activation (Figure 4J). Similarly, upon OVA323-339 peptide loading, total CAFs, apCAFs, and macrophages from FEBP-sTβRII-treated KPC tumors enhanced OT-II CD4$^+$ T cell activation significantly more than matched populations from control- or sTβRII-treated counterparts (Figure 4K). This MHC class II-dependent functional enhancement was independently validated in B16-OVA tumors, where CAFs, apCAFs, and macrophages from FEBP-sTβRII-treated environments more effectively stimulated OT-II CD4$^+$ T cells (Figure S5L). Of note, isolated apCAFs were explicitly included in these assays to increase the sensitivity of detecting stromal-mediated OT-II CD4$^+$ T cell activation.

Collectively, these data demonstrate that FEBP-sTβRII converts a myoCAF- and MDSC-dominated, immune-excluded niche into an antigen-presenting stromal-myeloid microenvironment. This remodeling coupled myofibroblast and MDSC contraction to expansion of IFN-responsive apCAF/iCAF and MHC-II$^+$ macrophage states, resulting in enhanced stromal-myeloid activation of antigen-specific CD4$^+$ and CD8$^+$ T cells.

FEBP-sTβRII initiates IFN-γ-dependent T cell feedback, amplifying antigen presentation and stabilizing an immune-instructive stromal-myeloid niche

Next, we investigated whether antigen presentation remodeling required immune-derived IFN-γ feedback. scRNA-seq showed that FEBP-sTβRII increased non-proliferating CD8$^+$ effector T (Teff) cells and shifted the lymphoid compartment toward effector and IFN-producing T cell states (Figures 5A, S6A, and S6B). Flow cytometry validated these findings, confirming increased frequencies of CD8$^+$IFN-γ$^+$ and CD4$^+$IFN-γ$^+$ T cells in both PANC02-Luc and KPC-Luc tumors following FEBP-sTβRII treatment relative to the control, sTβRII, or mutFEBP-sTβRII groups (Figure 5B). Furthermore, FEBP-sTβRII enriched CD8$^+$ T cells for IFN-γ response, activation, and cytotoxicity programs; enhanced IFN and immune activation while dampening TGF-β receptor signaling in CD4$^+$ non-Tregs; and modulated

Figure 5. IFN-γ functions as a secondary amplifier of FEBP-sTβRII-induced antigen presentation and effector immunity

(A) UMAP of lymphoid lineages from PANC02-Luc tumors treated with control, sTβRII, or FEBP-sTβRII.

(B) Flow cytometric quantification of CD4$^+$IFN-γ$^+$ and CD8$^+$IFN-γ$^+$ T cells in PANC02-Luc and KPC-Luc tumors treated with control, sTβRII, FEBP-sTβRII, or mutFEBP-sTβRII, shown as cells per gram of tumor (n = 8–10/group; 2 technical replicates).

(C) *In vivo* depletion assays were performed in orthotopic PANC02-Luc tumor-bearing mice, which were treated with control, FEBP-sTβRII alone, or FEBP-sTβRII in combination with depletion of CD4$^+$ T cells, CD8$^+$ T cells, or IFN-γ (n = 5/group).

(D) Representative α-SMA/CD8 immunofluorescence images and quantification of α-SMA-positive tumor edges in PANC02-Luc (day 26) and KPC-Luc (day 17) tumors following the indicated treatments (n = 5/group; scale bars: 100 μm). Each point represents one mouse (≥3 ROIs averaged per mouse).

(E and F) Flow cytometric analysis of CAF-state distribution (E) and M1/M2 macrophage ratio (F) in PANC02 (n = 5/group), KPC (n = 5–6/group), and B16-OVA (n = 6/group) tumors treated with control, FEBP-sTβRII, or FEBP-sTβRII plus anti-IFN-γ (3 technical replicates).

(G) Flow cytometric quantification of SIINFEKL-H-2K^b presentation (SIINFEKL$^+$ frequency) in myoCAFs, apCAFs, and M1 macrophages from PANC02-OVA tumors (n = 6/group).

(H–J) scRNA-seq-derived CCI networks of TGF-β ligand-receptor (H), immune-stimulatory (I), and compensatory/immune-inhibitory signaling (J) in the TME following the indicated treatments.

Data are presented as mean ± SD; Šidák-adjusted comparisons following one-way ANOVA on square-root-transformed data (B and D), one-way ANOVA (E, F, and G; myoCAF/apCAF), or Welch's unpaired t tests (G; M1 macrophages).

See also Figures S6 and S8 and Table S2.

IL-2/cytokine-related programs in Tregs, collectively indicating a broad relief of T cell suppression (Figure S6B; Tables S2A and S2B). FEBP-sTβRII did not induce a compensatory Treg-dominant state, as assessed by Treg abundance and p-STAT5 activation (Figures S6C and S6D).

We performed immune cell depletion experiments to identify the specific immune subpopulations required for FEBP-sTβRII-mediated tumor suppression. In PANC02-Luc tumor-bearing mice, the antitumor efficacy and prolonged survival achieved by FEBP-sTβRII were completely abolished by the depletion of $CD8^+$ T cells or the neutralization of IFN-γ. Conversely, the depletion of $CD4^+$ T cells exerted a significant but less pronounced effect on efficacy[30,31] (Figures 5C and S6E). Given the absolute requirement for IFN-γ in FEBP-sTβRII-mediated tumor control, we next asked whether IFN-γ also contributes to the observed stromal and myeloid remodeling. In PANC02-Luc tumors, concomitant IFN-γ neutralization substantially reversed the FEBP-sTβRII-induced reduction in α-SMA^+ area fraction, restoring it toward baseline levels. However, the α-SMA^+ stroma remained qualitatively less compact than that of control tumors, suggesting residual remodeling of α-SMA-defined stromal organization despite IFN-γ blockade (Figure 5D). In parallel, p-SMAD2/3 suppression remained detectable under IFN-γ blockade, although it was partially attenuated compared with FEBP-sTβRII treatment alone (Figure S6F). Together, these findings support an IFN-γ-independent layer of local TGF-β signaling inhibition, while indicating that IFN-γ is required for full downstream stromal-myeloid immune amplification.

Anti-IFN-γ co-treatment similarly attenuated both FEBP-sTβRII-induced apCAF enrichment and the associated increase in the M1/M2 macrophage ratio across PANC02-Luc, KPC-Luc, and B16-OVA tumors (Figures 5E and 5F). To distinguish proximal TGF-β target engagement from immune-dependent amplification, we examined the temporal kinetics of CAF and macrophage remodeling following FEBP-sTβRII treatment. FEBP-sTβRII significantly increased apCAFs by day 19, and this remodeled stromal state was maintained through day 35, showing a further increasing trend that did not reach statistical significance. Meanwhile, the macrophage M1/M2 ratio was also significantly elevated by day 19 and became further amplified by day 35, indicating that while both CAF and macrophage remodeling are initiated early, they follow distinct kinetic trajectories (Figure S6G).

Furthermore, anti-IFN-γ co-treatment reduced SIINFEKL-$H2K^b$ presentation in apCAFs and M1 macrophages within the PANC02-OVA and B16-OVA models, whereas presentation by myoCAFs remained largely unaffected (Figures 5G and S6H). Consistently, IFN-γ neutralization decreased the expression of MHC class I/II-related genes, as well as *Cd80* and *Cd86*, in PANC02-Luc tumors (Figure S6I). In *ex vivo* TGF-β1-exposed CAF, tumor-associated macrophage (TAM), or bone marrow-derived macrophage (BMDM) culture systems, FEBP-sTβRII potentiated IFN-γ-driven apCAF-like conversion and M1 macrophage polarization. Similar activation patterns in mono- and co-cultures suggested that these changes can occur, at least in part, without direct CAF-macrophage bidirectional crosstalk (Figure S6J).

We next examined whether these phenotypic shifts were accompanied by a broader remodeling of cell-cell interaction (CCI) networks.[16,32] Ligand-receptor interaction analysis revealed that FEBP-sTβRII reduced TGF-β-mediated inhibitory communication among the stromal, myeloid, and lymphoid compartments, consistent with the direct local inhibition of TGF-β signaling (Figure 5H; Table S2C). Concurrently, within the same tumors, FEBP-sTβRII enhanced immunostimulatory communication between antigen-presenting stromal/myeloid cells and Teff cells, including pathways linked to antigen presentation, leukocyte trafficking, and T cell activation (Figure 5I; Table S2C). Importantly, this immune activation was not accompanied by the broad expansion of compensatory suppressive circuits; rather, immune-inhibitory communication networks[33,34] were comparatively reduced or restrained following FEBP-sTβRII treatment (Figure 5J; Table S2C).

Beyond stromal-immune rewiring, FEBP-sTβRII also reshaped malignant epithelial programs, downregulating transcripts associated with proliferation, epithelial-mesenchymal transition (EMT), drug resistance, and survival (Figure S6K). However, flow cytometry showed no significant expansion of NK-T cells or B lymphocytes in either PANC02-Luc tumors or KPC-Luc tumors (Figure S6L). Similarly, scRNA-seq profiling revealed a reduction in endothelial motility-related genes, which correlated with immunohistochemical validation showing no significant increase in $CD31^+$ endothelial abundance (Figure S6M). Thus, FEBP-sTβRII primarily drives an antigen-visible stromal-myeloid remodeling rather than nonspecific lymphoid, endothelial, or vascular activation.

Together, these findings support a two-layer, feedforward mechanism for FEBP-sTβRII. FN-EDB-retained TGF-β trapping attenuates stromal TGF-β signaling and myofibroblastic barrier features, creating a permissive niche for T cell entry. Once established in the tumor bed, activated T cells provide IFN-γ-dependent feedback that amplifies MHC induction, apCAF remodeling, inflammatory macrophage polarization, and functional antigen presentation. Thus, FEBP-sTβRII links stromal relaxation and immune activation as mutually reinforcing consequences of localized TGF-β neutralization, rather than as a strict linear sequence.

The FEBP-sTβRII-remodeled stromal-immune axis is conserved in human tumors and partially recapitulated in humanized models

To evaluate the translational relevance of FEBP-sTβRII-induced remodeling, we generated cell-type-restricted signatures from the PANC02 scRNA-seq dataset, representing the myoCAF, *Dcn*$^+$-apCAF, MHC-II^+-Macro, and $CD8^+$-Teff states. Signature genes were selected based on their preferential expression within each target population and minimal baseline expression across unrelated lineages. We first validated these signatures in bulk RNA-seq datasets from both the discovery PANC02 and independent KPC PDAC models. In both systems, FEBP-sTβRII suppressed the myoCAF signature, while coordinately enriching the $CD8^+$-Teff, MHC-II^+-Macro, and *Dcn*$^+$-apCAF signatures (Figures 6A and 6B). Crucially, these immune-activating signatures were positively correlated with one another, whereas the myoCAF signature was inversely correlated with this antigen-presenting stromal-myeloid-T cell module, demonstrating a reproducible stromal-immune remodeling architecture across independent murine PDAC models.

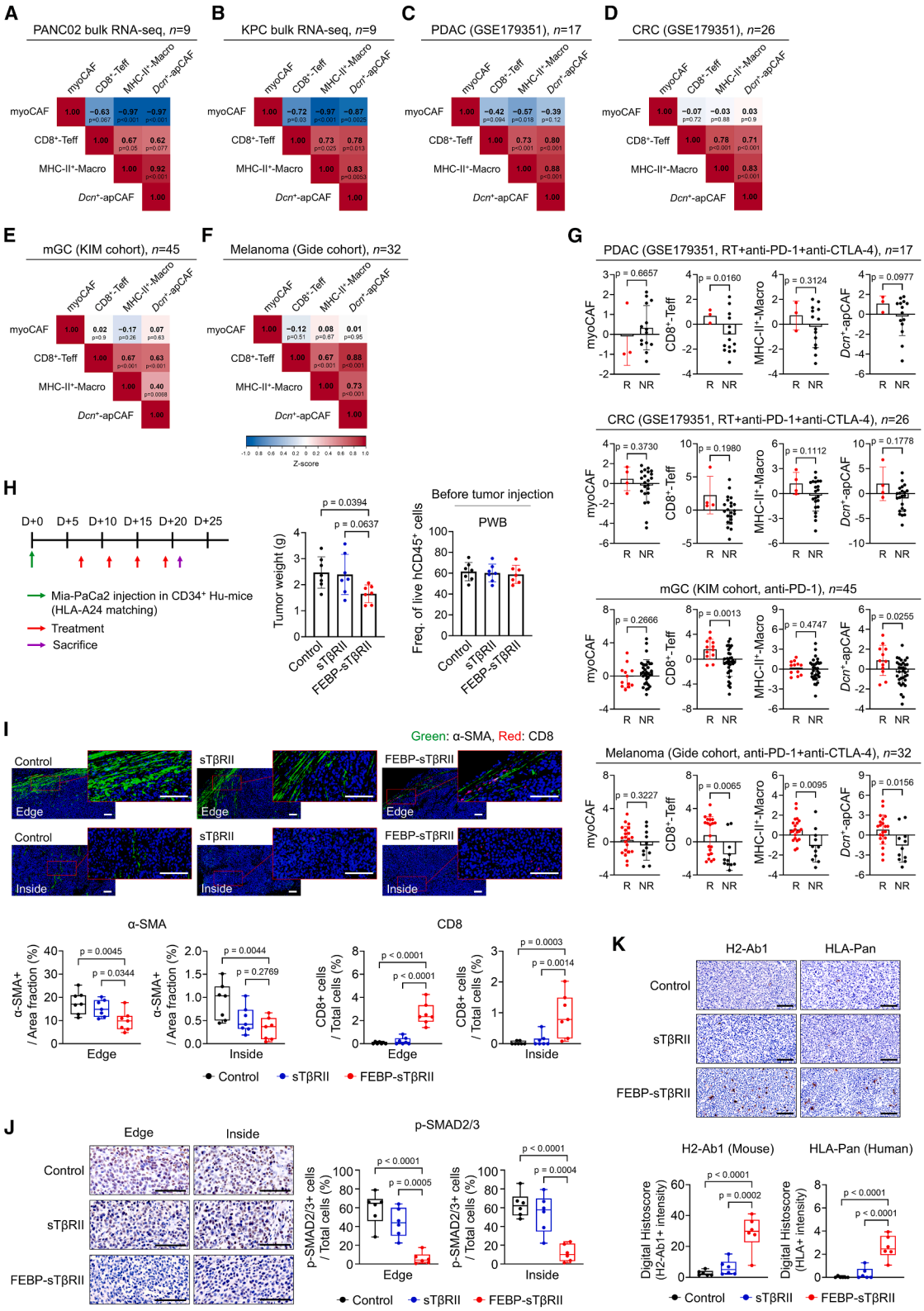


Figure 6. The FEBP-sTβRII-remodeled stromal-immune axis is conserved in human tumors and validated in humanized mice

(A–F) Correlation analysis of myoCAF, CD8$^+$-Teff, MHC-II$^+$-Macro, and *Dcn*$^+$-apCAF signatures in (A) PANC02 and (B) KPC bulk RNA-seq datasets and (C) PDAC, (D) MSS-CRC, (E) mGC, and (F) melanoma cohorts. Correlations were calculated using Spearman's rank correlation coefficient.

(G) Comparison of signature scores between responders (R) and non-responders (NR) in the indicated human cohorts (mean ± SD; Welch's unpaired *t* test).

(legend continued on next page)

We next projected these mouse-derived signatures onto their human orthologs and analyzed datasets from clinical cohorts of patients treated with ICIs, including human PDAC,[35] microsatellite-stable colorectal cancer (MSS-CRC),[35] metastatic gastric cancer (mGC),[36] and melanoma[37] (Figures 6C–6F). Across these clinical datasets, the CD8$^+$-Teff, MHC-II$^+$-Macro, and *Dcn*$^+$-apCAF signatures remained coordinately enriched, supporting conservation of the FEBP-sTβRII-responsive module in human tumors. The inverse association between the myoCAF and immune-activating signatures was the strongest in PDAC and more variable in the other cancers, suggesting tumor-type-dependent coupling between fibrotic stromal restriction and immune activation.

We next examined whether this module was associated with clinical response to ICIs. As expected within the ICI-treated cohorts, CD8$^+$-Teff scores were significantly higher in responders across the PDAC, mGC, and melanoma cohorts, whereas MSS-CRC responders showed a numerically higher, though non-significant, trend. Importantly, this response-associated immune activity was not restricted to CD8$^+$ T cell enrichment alone: *Dcn*$^+$ apCAF scores were significantly higher in mGC and melanoma responders, displayed a favorable trend in PDAC, and showed no significant association in MSS-CRC. MHC-II$^+$ macrophage scores were significantly enriched exclusively in melanoma responders, with no significant differences observed in the other cohorts. In contrast, myoCAF activity defined a separable fibrotic stromal axis; while actively antagonized by FEBP-sTβRII in mouse tumors, it was insufficient on its own to predict checkpoint responsiveness in patients (Figure 6G). Thus, the FEBP-sTβRII-responsive program is best interpreted as a coordinated TME state rather than a single-cell-type biomarker.

We next evaluated FEBP-sTβRII in CD34$^+$ huHSC-NKG-ProF humanized mice bearing orthotopic, HLA-A24-matched MiaPaCa2 tumors. Baseline human CD45$^+$ immune engraftment was comparable across groups, and FEBP-sTβRII significantly reduced tumor weight compared with the control, although the magnitude of tumor restriction at day 21 was modest relative to the robust efficacy observed in fully syngeneic PANC02-Luc and KPC-Luc models (Figure 6H). This attenuated response aligns with a well-documented limitation of conventional humanized xenografts: human T cells and tumor cells are embedded within a predominantly murine stromal and myeloid framework, where human T cell-derived IFN-γ is largely incompatible with native murine IFN-γ receptor signaling on CAFs and myeloid cells.[38,39] Despite this cross-species constraint, FEBP-sTβRII induced clear pharmacodynamic remodeling. Treatment significantly reduced α-SMA$^+$ stromal areas, increased CD8$^+$ T cell infiltration, and suppressed p-SMAD2/3 signaling. Furthermore, it enhanced both murine H2-Ab1 and human pan-HLA staining, indicating local TGF-β pathway inhibition, stromal relaxation, and the induction of antigen presentation programs within humanized tumors (Figures 6I–6K). Together, these data support the translational potential of FEBP-sTβRII in humans, while highlighting that current humanized mouse platforms may underestimate therapies whose full activity depends on IFN-γ-linked CAF-myeloid-lymphocyte reciprocity.

FEBP-sTβRII promotes effector and memory T cell programming and establishes durable antitumor immunity

Next, we investigated whether FEBP-sTβRII-induced complete tumor regression was linked to antigen-recallable immunity. In IFN-γ ELISpot assays, pancreatic lymph node cells from FEBP-sTβRII-treated, PANC02-Luc-bearing mice exhibited robust responses to dendritic cells (DCs)[40] loaded with PANC02 tumor cell lysate, while the control, sTβRII, and mut-FEBP-sTβRII groups showed only weak responses (Figure 7A). Similar tumor-lysate-reactive responses were observed in the KPC model (Figure S7A), supporting homologous tumor-antigen recall across independent PDAC models. In the B16-OVA model, FEBP-sTβRII-treated mice demonstrated increased IFN-γ ELISpot responses to both MHC class I- and MHC class II-restricted OVA peptides, indicating enhanced CD8$^+$ and CD4$^+$ T cell memory responses (Figure S7B).[41,42]

TGF-β regulates inflammatory and memory responses, but whether localized TGF-β neutralization generates durable antitumor recall remains unclear.[43] We, therefore, examined whether FEBP-sTβRII-induced recall responses were associated with a distinct memory phenotype.[44,45] FEBP-sTβRII significantly increased the frequency of CD44^{hi}CD62L^{lo}CD127$^+$ effector-memory-like CD4$^+$ and CD8$^+$ T cells within KPC-Luc and PANC02-Luc tumors, whereas sTβRII and mutFEBP-sTβRII exerted no such effect (Figure 7B). scRNA-seq profiling further identified the coordinated enrichment of effector memory[46–49] and memory T cell survival/niche-maintenance programs,[50] without a broad induction of canonical tissue-resident memory (TRM)-associated genes (Figures S7C and S7D). Consistently, GSEA using the GSE41867 memory-versus-exhausted CD8$^+$ T cell signatures demonstrated a robust enrichment of a memory-like CD8$^+$ program in FEBP-sTβRII-treated tumors relative to the control and sTβRII-treated groups (Figure S7E). This memory-associated program extended systemically, as evidenced by effector memory T (Tem)-related transcriptional enrichment in PWB from FEBP-sTβRII-treated mice, alongside increased frequencies of circulating effector-memory-like CD4$^+$ and CD8$^+$ T cells in both PDAC models (Figures 3I, 7C, and 7D). Crucially, the absence of widespread inflammatory gene induction further supports a model of systemic adaptive priming rather than nonspecific, cytokine-driven activation (Figure 3H).

(H) Treatment scheme and tumor weight after control, sTβRII, or FEBP-sTβRII treatment in the Mia-PaCa2 orthotopic humanized mouse model (n = 7/group; left). Frequency of live human CD45$^+$ cells in PWB before tumor implantation (right).
(I) Immunofluorescence images and quantification of α-SMA (green) and CD8$^+$ T cells (red) in the tumor edge and inside regions of Mia-PaCa2 tumors (n = 7/group; scale bars: 100 μm).
(J) p-SMAD2/3 expression and quantification in the tumor edge and inside regions (n = 6/group; scale bars: 100 μm).
(K) H2-Ab1 and pan-HLA staining and quantification (n = 6/group; scale bars: 100 μm).
Data are mean ± SD analyzed by one-way ANOVA with Šidák's correction (H–K; square-root-transformed for I and K). Each point represents one mouse (≥3 ROIs averaged per mouse) (I–K).

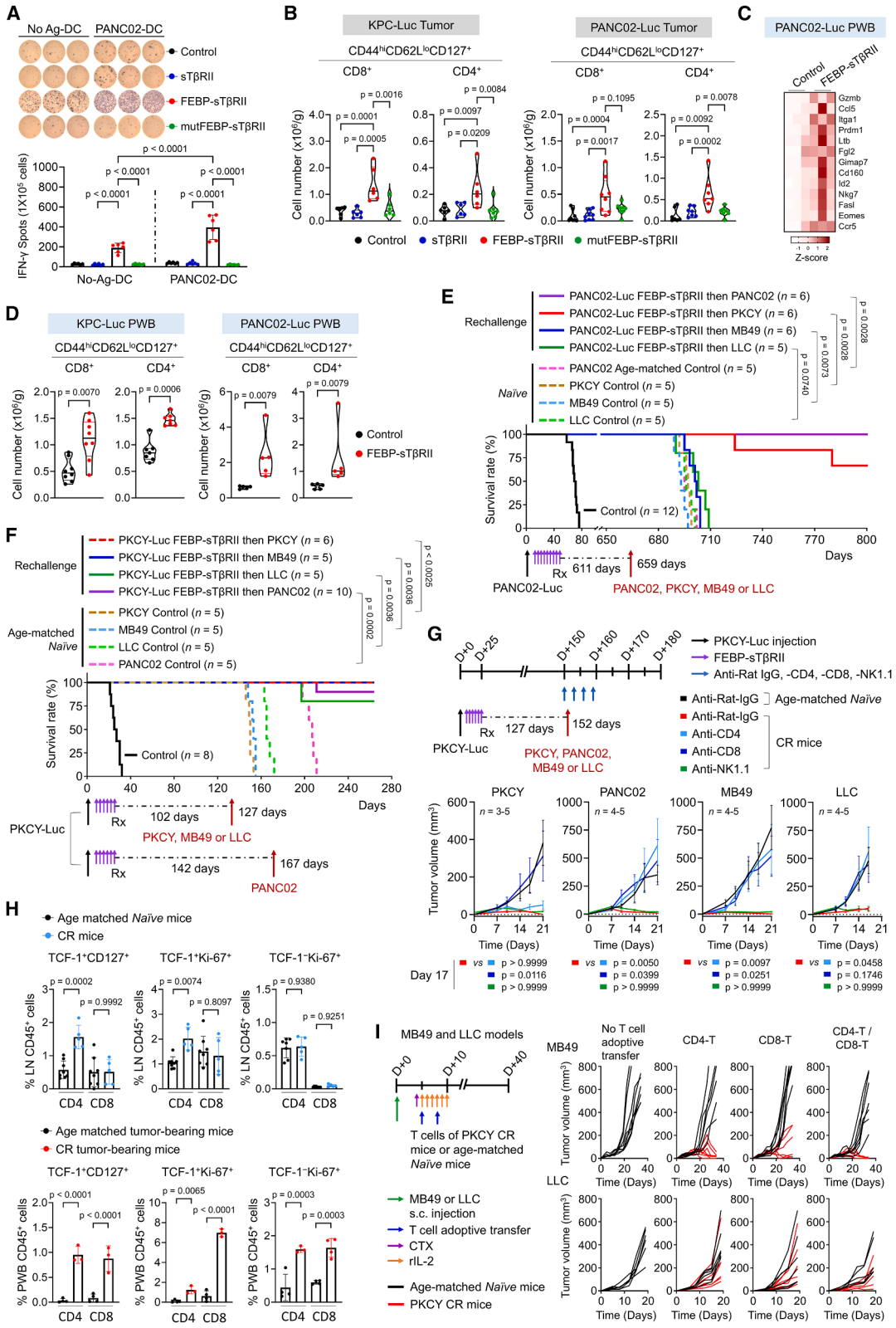


Figure 7. FEBP-sTβRII establishes durable systemic antitumor memory with recall capacity

(A) ELISpot assay of LN cells from orthotopic PANC02-Luc tumor-bearing mice after overnight co-culture with DCs pulsed with or without PANC02 lysate (*n* = 6/group).

(legend continued on next page)

To determine whether this memory program translated into durable functional immunity, the mice cured of orthotopic PANC02 or PKCY tumors were rechallenged with tumor cells without further therapeutic intervention. Remarkably, PANC02 survivors completely rejected homologous tumor challenges on day 122 or day 611, achieving 100% long-term survival, whereas age-matched naive controls developed progressive, lethal tumors (Figures 7E and S7F). Furthermore, among PANC02 survivors rechallenged with heterologous but syngeneic PKCY tumors on day 611, four out of six mice achieved CR by day 40. The remaining two mice exhibited a marked tumor growth delay, resulting in significantly prolonged survival compared with naive controls ($p = 0.0028$). In contrast, heterologous challenges with unrelated MB49 or Lewis lung carcinoma (LLC) cells caused only modest tumor growth delays (Figures 7E and S7G), indicating variable heterologous protection across tumor types.

Unexpectedly, PKCY complete responders also rejected homologous PKCY rechallenge and showed broader heterologous protection, including MB49 rejection, LLC rejection in four of five mice, and PANC02 tumor outgrowth in only one of ten mice (Figures 7F and S7H). Heterologous tumors frequently exhibited initial transient growth followed by subsequent regression. Thus, FEBP-sTβRII induces complete homologous and tumor-context-dependent heterologous protection, which is most prominent in PKCY survivors.

To identify the specific lymphocyte subsets mediating this durable protection, we subjected PKCY-CR mice to *in vivo* depletion of $CD4^+$ T cells, $CD8^+$ T cells, or NK cells 127 days after FEBP-sTβRII treatment, followed by a homologous PKCY or heterologous (PANC02, MB49, or LLC) rechallenge. $CD8^+$ T cell depletion completely abolished homologous PKCY protection, whereas $CD4^+$ T cell depletion exerted only a limited effect. In contrast, the depletion of either $CD4^+$ cells or $CD8^+$ T cells completely abrogated protection against all heterologous tumors, indicating that heterologous protection strictly requires $CD4^+$ T cell help in addition to $CD8^+$ T cells. Conversely, NK cells were dispensable for protective immunity in both homologous and heterologous settings (Figure 7G).

We next assessed whether a durable T cell memory-like state persisted after tumor clearance in PKCY-CR mice.[51,52] Compared with age-matched naive controls, CR mice showed increased $TCF1^+CD127^+$ and $TCF1^+Ki67^+$ populations among $CD4^+$ T cells in the inguinal lymph nodes, without expansion of $TCF1^-Ki67^+$ effector-like cells, whereas $CD8^+$ T cell populations remained largely unchanged (Figure 7H, top). Similar trends were observed in the spleen, indicating preferential maintenance of a $CD4^+$ memory-like compartment during homeostasis. Upon heterologous rechallenge, CR mice showed increased $TCF1^+CD127^+$, $TCF1^+Ki67^+$, and $TCF1^-Ki67^+$ populations in both circulating $CD4^+$ and $CD8^+$ T cells relative to age-matched tumor-bearing controls (Figure 7H, bottom). This shift is consistent with systemic, memory-associated activation during tumor challenge.

To assess the transferability of this antitumor T cell activity, we adoptively transferred $CD4^+$ and $CD8^+$ T cells isolated from PKCY-CR mice into wild-type recipients, which were subsequently challenged with heterologous tumors. In the MB49 model, CR-derived $CD4^+$ T cells induced complete tumor rejection in all recipients following an initial transient outgrowth (CR, 6/6). CR-derived $CD8^+$ T cells also exhibited greater antitumor activity than age-matched naive $CD8^+$ T cells, although they achieved fewer complete responses (CR, 3/6). Notably, the co-transfer of combined $CD4^+$ and $CD8^+$ T cells led to complete rejection in all recipients (CR, 6/6) (Figure 7I, top).

In contrast, within the LLC model, the transfer of CR-derived $CD4^+$ T cells, $CD8^+$ T cells, or both populations combined resulted in only limited tumor suppression and failed to recapitulate the robust protection observed in the original CR hosts (Figure 7I, bottom). Finally, to evaluate antigen cross-reactivity, PANC02-primed splenocytes were restimulated with DCs loaded with PANC02, PKCY, or MB49 cell lysates. Responses were robustly detected against PANC02 and PKCY, but not MB49, indicating shared PDAC antigen recognition, while suggesting that MB49 protection is not explained solely by lysate-level cross-reactivity (Figure S7I).

Collectively, these data demonstrate that FEBP-sTβRII converts local, matrix-restricted TGF-β blockade into systemic, antigen-recallable immunity. This protective memory is characterized by CD8-dependent homologous protection, CD4/CD8-cooperative heterologous protection, and context-dependent transferability shaped by both T cell memory intrinsic features and the immune accessibility of the recipient TME.

(B) Quantification of $CD8^+$ and $CD4^+$ Tem subsets in KPC-Luc and PANC02-Luc tumors ($n = 6$–8/group; 3 technical replicates).
(C) Heatmap of Tem signatures in PWB of PANC02-Luc tumor-bearing mice ($n = 3$/group).
(D) Quantification of $CD8^+$ and $CD4^+$ Tem subsets in PWB of KPC-Luc- and PANC02-Luc-tumor-bearing mice ($n = 5$–8/group).
(E) Tumor-free long-term PANC02-Luc survivors were rechallenged subcutaneously with PANC02 or heterologous tumor cells on day 611 after completion of treatment.
(F) Reciprocal rechallenges were performed in FEBP-sTβRII-cured, long-term tumor-free PKCY-Luc survivors and age-matched naive controls. Mice were rechallenged subcutaneously with PKCY, MB49, or LLC cells on day 102 after completion of treatment or with PANC02 cells on day 142 after completion of treatment.
(G) PKCY-Luc survivors were subcutaneously rechallenged with PKCY ($n = 3$–5), PANC02, MB49, or LLC ($n = 4$–5) tumor cells on day 152. Tumor growth was monitored following *in vivo* depletion of $CD4^+$ T cells, $CD8^+$ T cells, or NK cells.
(H) Frequencies of $CD4^+$ and $CD8^+$ memory-associated T cell subsets in inguinal lymph nodes of age-matched naive and tumor-free CR mice before rechallenge (top, $n = 5$–8/group) and in PWB of age-matched and CR mice bearing MB49 or LLC tumors (bottom, $n = 3$–4/group).
(I) Tumor growth in MB49 and LLC models following adoptive transfer of T cells from age-matched naive or PKCY-Luc CR mice ($n = 5$–8/group).
Quantitative data are presented as mean ± SD; two-way ANOVA with Tukey's test (A and G; log-transformed for A); one-way ANOVA on square-root-transformed data (B) and two-way mixed-effects analysis (H), both with Šidák's correction; two-tailed Mann-Whitney U test (D) and log-rank (Mantel-Cox) test with Holm-Šidák-adjusted pairwise comparisons (E and F).
See also Figures S7 and S8.

DISCUSSION

The ultimate goal of cancer immunotherapy is to establish sustained, systemic tumor control through durable immune protection. However, many solid tumors remain refractory because a dense stromal architecture and immunosuppressive cytokine circuits impair immune priming, restrict T cell trafficking, and dampen tumor-directed effector functions.[53] TGF-β serves as a central regulator of this immune-excluded state, antagonizing T cell activation, myeloid inflammatory polarization, antigen presentation, and stromal accessibility.[5,12,54] While current TGF-β inhibitors broadly block this pathway throughout the body, disrupting TGF-β's tumor-suppressive functions in healthy tissues and causing dose-limiting toxicities,[55] we addressed this hurdle by demonstrating the critical necessity of spatial targeting to specifically neutralize TGF-β within the tumor bed. Here, we show that FEBP-sTβRII successfully translates pleiotropic TGF-β biology into a geographically precise pharmacology by anchoring a soluble TβRII decoy to the oncofetal ECM splice isoform FN-EDB, thereby unlocking a robust and localized antitumor therapeutic program.

A central conclusion of this study is that the anatomical site of TGF-β neutralization, rather than pathway blockade alone, dictates the therapeutic outcome. The binding-defective mut-FEBP-sTβRII control was essential for this conclusion: despite preserved soluble TGF-β trapping, it failed to reproduce FEBP-sTβRII-induced tumor control, stromal-immune remodeling, antigen presentation, or memory phenotypes. Thus, FEBP-sTβRII is not simply a more potent soluble TGF-β inhibitor; rather, its therapeutic activity emerges uniquely from FN-EDB-dependent matrix retention, which converts systemic TGF-β trapping into localized stromal pharmacology. By validating this strategy across SMAD4-impaired PANC02-Luc tumors and KRAS/TP53-driven PKCY-Luc and KPC-Luc tumors, we further demonstrate that matrix-retained TGF-β blockade remains highly effective across PDAC contexts with distinct epithelial TGF-β dependencies.

Mechanistically, FEBP-sTβRII reprogrammed the TME from a myofibroblast- and MDSC-dominant exclusion state into an antigen-visible stromal-myeloid ecosystem. Orthogonal analyses leveraging scRNA-seq, flow cytometry, histology, SIINFEKL-H-2K^b presentation, and OT-I/OT-II adoptive transfer assays demonstrated that FEBP-sTβRII contracts matrix-remodeling myoCAF programs, while expanding immunostimulatory CAF and macrophage states capable of supporting antigen-specific CD4$^+$ and CD8$^+$ T cell activation. Crucially, these effects should not be viewed as exclusively immune mediated; local TGF-β blockade also altered the malignant epithelial, ECM, and vascular-associated programs, which collectively contribute to tumor restraint and metastatic suppression. Accordingly, the near-complete restriction of breast cancer metastasis to the lung is best interpreted as an integrated consequence of primary-tumor control, stromal/vascular remodeling, and systemic immune activation, rather than definitive evidence of post-dissemination immune clearance.

These findings fundamentally refine our understanding of apCAF biology. FEBP-sTβRII does not simply expand a generic antigen-presenting fibroblast state; instead, it orchestrates an IFN-responsive, MHC-enriched stromal-myeloid network embedded within a T cell-inflamed niche. Thus, the therapeutic value of apCAF remodeling appears to depend on whether antigen presentation programs are functionally coupled to co-stimulation, myeloid activation, and CD8$^+$ T cell accessibility, rather than on nominal MHC expression alone. In this context, this localized antigen-presenting capacity becomes an integral part of a coordinated stromal-myeloid circuit, providing a clear mechanistic basis for the downstream epitope spreading and cross-protective immunity observed across our models.

This highly coordinated cell-to-cell interaction supports a feedforward amplification loop. Local TGF-β neutralization relaxes the restrictive stromal barrier, permitting T cell entry into the tumor bed. Once established within the TME, CD8$^+$ T cells and IFN-γ drive an initial wave of antigen presentation, macrophage activation, and stromal immune accessibility, while CD4$^+$ T cells provide an additional layer of helper signals necessary for secondary and heterologous antitumor responses. Rather than dictating a strictly linear sequence, this framework positions FEBP-sTβRII as a localized pharmacologic trigger that unlocks a reciprocal, multicellular stromal-myeloid-T cell amplification loop.

To interrogate the translational durability of this cellular circuit, we examined the long-term immunological architecture after tumor clearance. Complete responders developed long-lived, antigen-recallable immunity that combined CD8-dependent homologous protection with context-dependent heterologous resistance. Heterologous rechallenge and adoptive transfer experiments showed that cross-protection operates as a composite phenomenon, rather than as a simple consequence of strict antigen cross-reactivity or T cell-intrinsic memory alone. Although heterologous protection required both CD4$^+$ and CD8$^+$ T cells, transfer studies revealed context-dependent limits, suggesting that durable protection also depends on host immune conditioning and tumor microenvironmental accessibility. This distinction provides important translational clarity, suggesting that clinical responses may depend not only on antitumor T cell induction but also on the remodelability and immune accessibility of the TME.

Unlike neutrophil-skewed inflammation triggered by untargeted soluble receptors, the PWB transcriptome remains essentially unchanged in FEBP-sTβRII. While formal toxicology and clinical safety evaluations remain mandatory to confirm whether this compartmentalized pharmacodynamic profile translates into reduced immune-related adverse events (irAEs) in patients, these findings establish a mechanistic rationale for testing, in future toxicology studies, whether compartmentalized TGF-β neutralization translates into a reduced peripheral safety burden.

The human relevance of this stromal-immune axis was strongly substantiated by human tumor datasets, in which the FEBP-sTβRII-responsive *Dcn*$^+$-apCAF, MHC-II$^+$-Macro, and CD8$^+$-Teff signatures were highly conserved and linked to immunotherapy-responsive microenvironments. Concurrently, our studies in CD34$^+$ humanized orthotopic pancreatic tumor models exposed a critical methodological constraint of current humanized platforms: while they successfully captured the direct pharmacodynamics of matrix-retained TGF-β neutralization, they only partially reconstructed the IFN-γ-dependent

stromal-immune feedforward circuit defined here. Together, these data support the preservation of the direct pharmacodynamic layer of matrix-retained TGF-β neutralization in the humanized model, while indicating that the complete IFN-γ-dependent immune-amplified mechanism cannot yet be confirmed and will require validation in advanced humanized stromal-immune models or clinical specimens.

Consequently, future clinical development should evaluate whether a biomarker panel comprising baseline FN-EDB expression, the myoCAF signature, antigen-presenting CAF/myeloid status, and the degree of baseline immune exclusion can effectively stratify and identify patients most likely to reap maximal therapeutic benefit from FEBP-sTβRII therapy.

Limitations of the study

This study demonstrates that targeting the TGF-β signaling pathway within the TME could provide a promising therapeutic strategy for difficult-to-treat cancers. However, because this study was conducted primarily in murine tumor models that recapitulate fibrosis and immune exclusion, clinical validation remains essential. Human cancers are molecularly, stromally, and immunologically complex. Therefore, future clinical trials must evaluate whether FN-EDB expression, stromal TGF-β activity, and baseline immune-exclusion signatures can reliably predict clinical responses.

The second limitation is the inherent heterogeneity of apCAF states. While FEBP-sTβRII promotes antigen visibility and T cell activation, apCAF states can shift between the stimulatory and tolerogenic functions depending on the cytokine milieu and myeloid interactions. Therefore, future high-resolution and functional studies are essential to pinpoint the specific stromal subpopulations required for effective antigen presentation and sustained immunity.

Finally, although FEBP-sTβRII induces long-term homologous and heterologous protection, the precise antigenic and cellular mechanisms remain to be fully defined. While TCR profiling suggests clonal expansion, determining absolute antigen specificity requires direct mapping. Furthermore, because heterologous protection was not fully transferable in all models, long-term memory likely depends on a cooperative post-therapy environment that supports antigen presentation, rather than on cross-reactive T cells alone. Therefore, comprehensive spatial and functional analyses are essential to clarify how local, matrix-retained TGF-β blockade coordinates this systemic immune memory.

RESOURCE AVAILABILITY

Lead contact

Requests for further information and resources should be directed to and will be fulfilled by the lead contact, Seong-Jin Kim (jasonsjkim@medpacto.com).

Materials availability

Unique reagents generated in this study are available from the lead contact upon reasonable request and may require a completed materials transfer agreement.

Data and code availability

The bulk RNA-seq and scRNA-seq raw data generated in this study have been deposited in the NCBI Sequence Read Archive (SRA) under BioProject accession number BioProject: PRJNA1241682. These datasets will be made publicly available upon publication. Publicly available immunotherapy cohorts analyzed in this study included the GEO: GSE179351 human PDAC and MSS-CRC cohorts,[35] as well as the Kim mGC[36] and Gide melanoma[37] cohorts obtained from the TIDE database. All data supporting the findings of this study are available within the article and supplemental information. Any additional information required to reanalyze the data reported in this paper is available from the lead contact upon request.

ACKNOWLEDGMENTS

We thank J.W. Woo, S. Kim, E.G. Kwon, and H.J. Kim for insightful discussions and valuable comments. We thank MedPacto bioprocessing team members C.M. Lee and M.W. Kim for assistance with SEC-MALS experiments, HEK293 and CHO cell maintenance, and protein purification. We also thank MedPacto Research Center team members S.Y. Choi, M.K. Kim, B.Y. Seo, H.J. Han, M.J. Cheon, N. Park, Y.J. Kim, S.Y. Kim, J.Y. Jung, J.H. Um, J.H. Lee, J.Y. Jung, and Y.A. Na for assistance with animal pathology support, research administrative support, and animal care support. This research was supported, in part, by the Korea Drug Development Fund, funded by Ministry of Science and ICT, Ministry of Trade, Industry, and Resources, and Ministry of Health and Welfare (2710092899, RS-2025-25449690, Republic of Korea).

AUTHOR CONTRIBUTIONS

D.W.K. conceptualized the project, designed and performed experiments, supervised research, analyzed data, created figures, and wrote the manuscript; J.B.B., J.K., H. Kim, J.S.K., J.M.K., M.G.K., and J.S.L. designed and conducted *in vitro/in vivo* experiments, analyzed data, and performed tumor genotyping; J.S.K., Y.S.K., and H. Kim conducted immunophenotyping; P.K., S.Y., and K.Y. conducted computational analysis for FEBP-sTβRII formats; J.B.B., J.K., J.S.L., and M.J.L. provided histopathological analysis and guidance; S.Y. and C.P.H. conducted bulk RNA-seq or scRNA-seq analysis for tumors/PWBs and DEG network figures; S.Y., J.M., and J.K. conducted scRNA-seq analysis for tumors and cell annotation and DEG and CCI network figures; C.L. contributed to statistics; K.Y., I.Y.K., and J.J.L. contributed to discussions and provided resources; S.-J.K. conceived and supervised the project, designed and supported the experiments, supervised the research, and wrote and edited the manuscript. All authors reviewed and approved the final manuscript.

DECLARATION OF INTERESTS

S.-J.K. is a founder of MedPacto and a co-founder of Celloram and serves on the boards of directors at MedPacto and Celloram. J.J.L. is a co-founder of Celloram and serves on the boards of directors at Celloram. J.J.L. and I.Y.K. are members of the clinical advisory boards of MedPacto. D.W.K., J.B.B., S.Y., J.K., J.S.K., K.Y., H.J.K., J.S.L., J.M.K., Y.S.K., M.G.K., and M.J.L. are employees of MedPacto. C.P.H. is an employee of YiPSCELL. MedPacto holds pending patent applications related to the therapeutic agent described in this study. The GILO Foundation has received research support from MedPacto.

DECLARATION OF GENERATIVE AI AND AI-ASSISTED TECHNOLOGIES IN THE MANUSCRIPT PREPARATION PROCESS

During the preparation of this manuscript, the authors used ChatGPT (OpenAI) and Gemini (Google) in order to improve the readability and language. The authors reviewed and edited the output as needed and take full responsibility for the content of the published article.

STAR★METHODS

Detailed methods are provided in the online version of this paper and include the following:

- KEY RESOURCES TABLE
- EXPERIMENTAL MODEL AND STUDY PARTICIPANT DETAILS

- Syngeneic mice
- Humanized mice
- Orthotopic 4T-1 tumor model in BALB/c mice
- Orthotopic CT26 tumor model in BALB/c mice
- Orthotopic B16F10 luc tumor model in C57BL/6J mice
- Orthotopic GL26 tumor model in C57BL/6J mice
- Orthotopic RM1-Luc tumor model in C57BL/6J mice
- Orthotopic Hepa1-6 tumor model in C57BL/6J mice
- Establishment of orthotopic 4T-1-luc-LMT-2 tumor model with highly metastatic potential
- Orthotopic PANC02-Luc pancreatic tumor model
- Orthotopic PKCY-Luc pancreatic tumor model
- Orthotopic KPC-Luc pancreatic tumor model
- Humanized orthotopic Mia-PaCa2 pancreatic tumor model
- Cell lines

- METHOD DETAILS
  - FEBP-sTβRII computer-generated model
  - Cloning of FEBP-sTβRII formats, sTβRII and antibody fusion formats
  - Expression and purification of FEBP-sTβRII formats, sTβRII and antibody fusion formats
  - Cell isolation from tumors for flow cytometry
  - CRISPR/Cas9-mediated deletion of the Fn1-EDB in murine KP-PSAFs
  - Flow cytometry
  - Adoptive cell transfer in the *Rag1*$^{-/-}$ mice bearing PKCY tumor treated with *FEBP-sTβRII*
  - B16-OVA-luc tumor model
  - PANC02-OVA-luc tumor model
  - Survival analysis
  - Tumor rechallenge studies
  - Memory-phase immune depletion
  - Adoptive transfer of memory T-cells
  - Cancer-associated fibroblasts (CAFs)-like cell isolation
  - Peripheral blood human CD45 analysis in humanized mice
  - TCF1/CD127/Ki67 recall analysis
  - Evaluation of the antigen-presenting capacity of CAFs and macrophages
  - Preparation of splenic dendritic cells and bone marrow-derived dendritic cells
  - *In vitro* stimulation of antigen-specific T-cells
  - Measurement of IFN-γ secretion by ELISPOT assay
  - Preparation of bone marrow-derived macrophages (BMDMs)
  - CAF and macrophage mono- and co-culture assays
  - Flow cytometry-based assay to assess binding of FEBP-sTβRII to FN-EDB *in vitro*
  - Measurement of FEBP-sTβRII binding by ELISA
  - TGF-β/SMAD luciferase reporter assay
  - Lentivirus production and transduction
  - *In vivo* bioluminescence and imaging
  - *In vivo* biodistribution analysis
  - *In vivo* time-course analysis for tissue retention
  - Depletion of immune-cell populations and IFN-γ neutralization
  - Tumor tissue TGF-β1 measurement
  - Immunohistochemistry analysis
  - ROI definitions for tumor-edge and tumor-interior analyses
  - Immunofluorescence staining for tissues and cells
  - Quantitative PCR with reverse transcription
  - Bulk RNA-seq library preparation and data processing
  - Differential expression and pathway analysis of bulk RNA-seq data
  - Single-cell RNA-seq preprocessing, integration, and clustering
  - Cell type annotation and pseudobulk expression analysis
  - scRNA-seq differential expression and functional enrichment
  - Cell–cell communication analysis
  - GTEx to TCGA comparison
  - Human immunotherapy cohorts
  - Signature generation and GSVA analysis
- QUANTIFICATION AND STATISTICAL ANALYSIS
  - Statistical analysis

SUPPLEMENTAL INFORMATION

Supplemental information can be found online at https://doi.org/10.1016/j.ccell.2026.10.007.

Received: January 8, 2026
Revised: August 20, 2026
Accepted: October 9, 2026
Published: November 9, 2026

REFERENCES

1. Schachter, J., Ribas, A., Long, G.V., Arance, A., Grob, J.J., Mortier, L., Daud, A., Carlino, M.S., McNeil, C., Lotem, M., et al. (2017). Pembrolizumab versus ipilimumab for advanced melanoma: final overall survival results of a multicentre, randomised, open-label phase 3 study (KEYNOTE-006). Lancet *390*, 1853–1862. https://doi.org/10.1016/S0140-6736(17)31601-X.

2. Borghaei, H., Paz-Ares, L., Horn, L., Spigel, D.R., Steins, M., Ready, N.E., Chow, L.Q., Vokes, E.E., Felip, E., Holgado, E., et al. (2015). Nivolumab versus Docetaxel in Advanced Nonsquamous Non-Small-Cell Lung Cancer. N. Engl. J. Med. *373*, 1627–1639. https://doi.org/10.1056/NEJMoa1507643.

3. Chan, M.K.K., Chan, E.L.Y., Ji, Z.Z., Chan, A.S.W., Li, C., Leung, K.T., To, K.F., and Tang, P.M.K. (2023). Transforming growth factor-beta signaling: from tumor microenvironment to anticancer therapy. Explor Target Antitumor Ther. *4*, 316–343. https://doi.org/10.37349/etat.2023.00137.

4. Zhang, T., Ren, Y., Yang, P., Wang, J., and Zhou, H. (2022). Cancer-associated fibroblasts in pancreatic ductal adenocarcinoma. Cell Death Dis. *13*, 897. https://doi.org/10.1038/s41419-022-05351-1.

5. Thomas, D.A., and Massagué, J. (2005). TGF-beta directly targets cytotoxic T cell functions during tumor evasion of immune surveillance. Cancer Cell *8*, 369–380. https://doi.org/10.1016/j.ccr.2005.10.012.

6. Tjomsland, V., Niklasson, L., Sandström, P., Borch, K., Druid, H., Bratthäll, C., Messmer, D., Larsson, M., and Spångeus, A. (2011). The desmoplastic stroma plays an essential role in the accumulation and modulation of infiltrated immune cells in pancreatic adenocarcinoma. Clin. Dev. Immunol. *2011*, 212810. https://doi.org/10.1155/2011/212810.

7. Principe, D.R., DeCant, B., Mascariñas, E., Wayne, E.A., Diaz, A.M., Akagi, N., Hwang, R., Pasche, B., Dawson, D.W., Fang, D., et al. (2016). TGFbeta Signaling in the Pancreatic Tumor Microenvironment Promotes Fibrosis and Immune Evasion to Facilitate Tumorigenesis. Cancer Res. *76*, 2525–2539. https://doi.org/10.1158/0008-5472.CAN-15-1293.

8. Achyut, B.R., Bader, D.A., Robles, A.I., Wangsa, D., Harris, C.C., Ried, T., and Yang, L. (2013). Inflammation-mediated genetic and epigenetic alterations drive cancer development in the neighboring epithelium upon stromal abrogation of TGF-beta signaling. PLoS Genet. *9*, e1003251. https://doi.org/10.1371/journal.pgen.1003251.

9. Song, M., He, J., Pan, Q.Z., Yang, J., Zhao, J., Zhang, Y.J., Huang, Y., Tang, Y., Wang, Q., He, J., et al. (2021). Cancer-Associated Fibroblast-Mediated Cellular Crosstalk Supports Hepatocellular Carcinoma Progression. Hepatology *73*, 1717–1735. https://doi.org/10.1002/hep.31792.

10. Grauel, A.L., Nguyen, B., Ruddy, D., Laszewski, T., Schwartz, S., Chang, J., Chen, J., Piquet, M., Pelletier, M., Yan, Z., et al. (2020). TGFbeta-blockade uncovers stromal plasticity in tumors by revealing the existence of a subset of interferon-licensed fibroblasts. Nat. Commun. *11*, 6315. https://doi.org/10.1038/s41467-020-19920-5.

11. Chakravarthy, A., Khan, L., Bensler, N.P., Bose, P., and De Carvalho, D.D. (2018). TGF-beta-associated extracellular matrix genes link cancer-associated fibroblasts to immune evasion and immunotherapy failure. Nat. Commun. *9*, 4692. https://doi.org/10.1038/s41467-018-06654-8.

12. Liu, S., Ren, J., and Ten Dijke, P. (2021). Targeting TGFbeta signal transduction for cancer therapy. Signal Transduct. Targeted Ther. *6*, 8. https://doi.org/10.1038/s41392-020-00436-9.

13. Elyada, E., Bolisetty, M., Laise, P., Flynn, W.F., Courtois, E.T., Burkhart, R.A., Teinor, J.A., Belleau, P., Biffi, G., Lucito, M.S., et al. (2019). Cross-Species Single-Cell Analysis of Pancreatic Ductal Adenocarcinoma Reveals Antigen-Presenting Cancer-Associated Fibroblasts. Cancer Discov. *9*, 1102–1123. https://doi.org/10.1158/2159-8290.CD-19-0094.

14. Song, J., Wei, R., Liu, C., Zhao, Z., Liu, X., Wang, Y., Liu, F., and Liu, X. (2025). Antigen-presenting cancer associated fibroblasts enhance anti-tumor immunity and predict immunotherapy response. Nat. Commun. *16*, 2175. https://doi.org/10.1038/s41467-025-57465-7.

15. Chen, X., Zhou, Z., Xie, L., Qiao, K., Jia, Y., Liu, S., Yazgan, Z., Rossi, F., Liu, Y., Zhang, B., et al. (2025). Single-cell resolution spatial analysis of antigen-presenting cancer-associated fibroblast niches. Cancer Cell *43*, 2224–2240.e9. https://doi.org/10.1016/j.ccell.2025.09.001.

16. Lakins, M.A., Ghorani, E., Munir, H., Martins, C.P., and Shields, J.D. (2018). Cancer-associated fibroblasts induce antigen-specific deletion of CD8 (+) T Cells to protect tumour cells. Nat. Commun. *9*, 948. https://doi.org/10.1038/s41467-018-03347-0.

17. Saw, P.E., Park, J., Jon, S., and Farokhzad, O.C. (2017). A drug-delivery strategy for overcoming drug resistance in breast cancer through targeting of oncofetal fibronectin. Nanomedicine. *13*, 713–722. https://doi.org/10.1016/j.nano.2016.10.005.

18. Saw, P.E., Kim, S., Lee, I.H., Park, J., Yu, M., Lee, J., Kim, J.I., and Jon, S. (2013). Aptide-conjugated liposome targeting tumor-associated fibronectin for glioma therapy. J. Mater. Chem. B *1*, 4723–4726. https://doi.org/10.1039/c3tb20815j.

19. Lieverse, R.I.Y., Marcus, D., van der Wiel, A.M.A., Van Limbergen, E.J., Theys, J., Yaromina, A., Lambin, P., and Dubois, L.J. (2020). Human fibronectin extra domain B as a biomarker for targeted therapy in cancer. Mol. Oncol. *14*, 1555–1568. https://doi.org/10.1002/1878-0261.12705.

20. Chen, S.Y., Kung, H.C., Espinoza, B., Washington, I., Chen, K., Wang, J., Zlomke, H., Loycano, M., Wang, R., Pickup, M., et al. (2024). Targeting heterogeneous tumor microenvironments in pancreatic cancer mouse models of metastasis by TGF-beta depletion. JCI Insight *9*, e182766. https://doi.org/10.1172/jci.insight.182766.

21. Korc, M. (2023). Heparin Prowess: Favorable Vascular-Immune Reprogramming in Pancreatic Cancer. Clin. Cancer Res. *29*, 2348–2350. https://doi.org/10.1158/1078-0432.CCR-23-0346.

22. Garg, P., Pareek, S., Kulkarni, P., Horne, D., Salgia, R., and Singhal, S.S. (2025). Exploring the potential of TGFbeta as a diagnostic marker and therapeutic target against cancer. Biochem. Pharmacol. *231*, 116646. https://doi.org/10.1016/j.bcp.2024.116646.

23. Xiong, W., He, W., Wang, T., He, S., Xu, F., Wang, Z., Wang, X., Guo, H., Ling, J., Zhang, H., et al. (2022). Smad4 Deficiency Promotes Pancreatic Cancer Immunogenicity by Activating the Cancer-Autonomous DNA-Sensing Signaling Axis. Adv. Sci. *9*, e2103029. https://doi.org/10.1002/advs.202103029.

24. Saiki, Y., Jiang, C., Ohmuraya, M., and Furukawa, T. (2021). Genetic Mutations of Pancreatic Cancer and Genetically Engineered Mouse Models. Cancers (Basel) *14*, 71. https://doi.org/10.3390/cancers14010071.

25. Bronte, V., Brandau, S., Chen, S.H., Colombo, M.P., Frey, A.B., Greten, T.F., Mandruzzato, S., Murray, P.J., Ochoa, A., Ostrand-Rosenberg, S., et al. (2016). Recommendations for myeloid-derived suppressor cell nomenclature and characterization standards. Nat. Commun. *7*, 12150. https://doi.org/10.1038/ncomms12150.

26. Kumar, V., Patel, S., Tcyganov, E., and Gabrilovich, D.I. (2016). The Nature of Myeloid-Derived Suppressor Cells in the Tumor Microenvironment. Trends Immunol. *37*, 208–220. https://doi.org/10.1016/j.it.2016.01.004.

27. Dersh, D., Yewdell, J.W., and Wei, J. (2019). A SIINFEKL-Based System to Measure MHC Class I Antigen Presentation Efficiency and Kinetics. Methods Mol. Biol. *1988*, 109–122. https://doi.org/10.1007/978-1-4939-9450-2_9.

28. Mittal, S.K., Cho, K.J., Ishido, S., and Roche, P.A. (2015). Interleukin 10 (IL-10)-mediated Immunosuppression: MARCH-I INDUCTION REGULATES ANTIGEN PRESENTATION BY MACROPHAGES BUT NOT DENDRITIC CELLS. J. Biol. Chem. *290*, 27158–27167. https://doi.org/10.1074/jbc.M115.682708.

29. Lerner, E.C., Woroniecka, K.I., D'Anniballe, V.M., Wilkinson, D.S., Mohan, A.A., Lorrey, S.J., Waibl-Polania, J., Wachsmuth, L.P., Miggelbrink, A.M., Jackson, J.D., et al. (2023). CD8(+) T cells maintain killing of MHC-I-negative tumor cells through the NKG2D-NKG2DL axis. Nat. Cancer *4*, 1258–1272. https://doi.org/10.1038/s43018-023-00600-4.

30. Kerdidani, D., Aerakis, E., Verrou, K.M., Angelidis, I., Douka, K., Maniou, M.A., Stamoulis, P., Goudevenou, K., Prados, A., Tzaferis, C., et al. (2022). Lung tumor MHCII immunity depends on in situ antigen presentation by fibroblasts. J. Exp. Med. *219*, e20210815. https://doi.org/10.1084/jem.20210815.

31. Thelemann, C., Eren, R.O., Coutaz, M., Brasseit, J., Bouzourene, H., Rosa, M., Duval, A., Lavanchy, C., Mack, V., Mueller, C., et al. (2014). Interferon-gamma induces expression of MHC class II on intestinal epithelial cells and protects mice from colitis. PLoS One *9*, e86844. https://doi.org/10.1371/journal.pone.0086844.

32. Efremova, M., Vento-Tormo, M., Teichmann, S.A., and Vento-Tormo, R. (2020). CellPhoneDB: inferring cell-cell communication from combined expression of multi-subunit ligand-receptor complexes. Nat. Protoc. *15*, 1484–1506. https://doi.org/10.1038/s41596-020-0292-x.

33. Pardoll, D.M. (2012). The blockade of immune checkpoints in cancer immunotherapy. Nat. Rev. Cancer *12*, 252–264. https://doi.org/10.1038/nrc3239.

34. Liu, F., Zhang, J., Gu, X., Guo, Q., and Guo, W. (2024). Single-cell transcriptome sequencing reveals SPP1-CD44-mediated macrophage-tumor cell interactions drive chemoresistance in TNBC. J. Cell Mol. Med. *28*, e18525. https://doi.org/10.1111/jcmm.18525.

35. Parikh, A.R., Szabolcs, A., Allen, J.N., Clark, J.W., Wo, J.Y., Raabe, M., Thel, H., Hoyos, D., Mehta, A., Arshad, S., et al. (2021). Radiation therapy enhances immunotherapy response in microsatellite stable colorectal and pancreatic adenocarcinoma in a phase II trial. Nat. Cancer *2*, 1124–1135. https://doi.org/10.1038/s43018-021-00269-7.

36. Kim, S.T., Cristescu, R., Bass, A.J., Kim, K.M., Odegaard, J.I., Kim, K., Liu, X.Q., Sher, X., Jung, H., Lee, M., et al. (2018). Comprehensive molecular characterization of clinical responses to PD-1 inhibition in metastatic gastric cancer. Nat. Med. *24*, 1449–1458. https://doi.org/10.1038/s41591-018-0101-z.

37. Gide, T.N., Quek, C., Menzies, A.M., Tasker, A.T., Shang, P., Holst, J., Madore, J., Lim, S.Y., Velickovic, R., Wongchenko, M., et al. (2019). Distinct Immune Cell Populations Define Response to Anti-PD-1 Monotherapy and Anti-PD-1/Anti-CTLA-4 Combined Therapy. Cancer Cell *35*, 238–255.e6. https://doi.org/10.1016/j.ccell.2019.01.003.

38. Hemmi, S., Peghini, P., Metzler, M., Merlin, G., Dembic, Z., and Aguet, M. (1989). Cloning of murine interferon gamma receptor cDNA: expression in human cells mediates high-affinity binding but is not sufficient to confer sensitivity to murine interferon gamma. Proc. Natl. Acad. Sci. USA *86*, 9901–9905. https://doi.org/10.1073/pnas.86.24.9901.

39. Hemmi, S., Böhni, R., Stark, G., Marco, F.D., and Aguet, M. (1994). A novel member of the interferon receptor family complements functionality of the murine interferon gamma receptor in human cells. Cell *76*, 803–810. https://doi.org/10.1016/0092-8674(94)90355-7.

40. Schnurr, M., Galambos, P., Scholz, C., Then, F., Dauer, M., Endres, S., and Eigler, A. (2001). Tumor cell lysate-pulsed human dendritic cells induce a T-cell response against pancreatic carcinoma cells: an in vitro model for the assessment of tumor vaccines. Cancer Res. *61*, 6445–6450.

41. Yakkala, C., Dagher, J., Sempoux, C., Chiang, C.L.L., Denys, A., Kandalaft, L.E., Koppolu, B., and Duran, R. (2021). Rate of Freeze Impacts the Survival and Immune Responses Post Cryoablation of Melanoma. Front. Immunol. *12*, 695150. https://doi.org/10.3389/fimmu.2021.695150.

42. Rowe, H.M., Lopes, L., Ikeda, Y., Bailey, R., Barde, I., Zenke, M., Chain, B.M., and Collins, M.K. (2006). Immunization with a lentiviral vector stimulates both CD4 and CD8 T cell responses to an ovalbumin transgene. Mol. Ther. *13*, 310–319. https://doi.org/10.1016/j.ymthe.2005.08.025.

43. Travis, M.A., and Sheppard, D. (2014). TGF-beta activation and function in immunity. Annu. Rev. Immunol. *32*, 51–82. https://doi.org/10.1146/annurev-immunol-032713-120257.

44. Masopust, D., Awasthi, A., Bosselut, R., Brooks, D.G., Buggert, M., Chamoto, K., Cui, W., Dong, C., Farber, D.L., Gebhardt, T., et al. (2026). Guidelines for T cell nomenclature. Nat. Rev. Immunol. *26*, 298–313. https://doi.org/10.1038/s41577-025-01238-2.

45. Principe, N., Kidman, J., Goh, S., Tilsed, C.M., Fisher, S.A., Fear, V.S., Forbes, C.A., Zemek, R.M., Chopra, A., Watson, M., et al. (2020). Tumor Infiltrating Effector Memory Antigen-Specific CD8(+) T Cells Predict Response to Immune Checkpoint Therapy. Front. Immunol. *11*, 584423. https://doi.org/10.3389/fimmu.2020.584423.

46. Kaech, S.M., Wherry, E.J., and Ahmed, R. (2002). Effector and memory T-cell differentiation: implications for vaccine development. Nat. Rev. Immunol. *2*, 251–262. https://doi.org/10.1038/nri778.

47. Kaech, S.M., and Cui, W. (2012). Transcriptional control of effector and memory CD8+ T cell differentiation. Nat. Rev. Immunol. *12*, 749–761. https://doi.org/10.1038/nri3307.

48. Dong, H., Ham, H., Barham, W., Wen, T., Hirdler, J.B., Mao, Z., Ashton, D.S., Zhang, W., Lucien-Matteoni, F., Borges da Silva, H., and Billadeau, D.D. (2025). A Dual Role for NKG7 in T-cell Cytotoxicity and Longevity. Cancer Immunol. Res. *13*, 1510–1515. https://doi.org/10.1158/2326-6066.CIR-25-0384.

49. Kohlmeier, J.E., Miller, S.C., Smith, J., Lu, B., Gerard, C., Cookenham, T., Roberts, A.D., and Woodland, D.L. (2008). The chemokine receptor CCR5 plays a key role in the early memory CD8+ T cell response to respiratory virus infections. Immunity *29*, 101–113. https://doi.org/10.1016/j.immuni.2008.05.011.

50. Limoges, M.A., Cloutier, M., Nandi, M., Ilangumaran, S., and Ramanathan, S. (2021). The GIMAP Family Proteins: An Incomplete Puzzle. Front. Immunol. *12*, 679739. https://doi.org/10.3389/fimmu.2021.679739.

51. Wieland, D., Kemming, J., Schuch, A., Emmerich, F., Knolle, P., Neumann-Haefelin, C., Held, W., Zehn, D., Hofmann, M., and Thimme, R. (2017). TCF1(+) hepatitis C virus-specific CD8(+) T cells are maintained after cessation of chronic antigen stimulation. Nat. Commun. *8*, 15050. https://doi.org/10.1038/ncomms15050.

52. Tu, T.H., Grunbaum, A., Santinon, F., Kazanova, A., Rozza, N., Kremer, R., Mihalcioiu, C., and Rudd, C.E. (2024). Decreased progenitor TCF1 + T-cells correlate with COVID-19 disease severity. Commun. Biol. *7*, 526. https://doi.org/10.1038/s42003-024-05922-2.

53. Falcomatà, C., Bärthel, S., Schneider, G., Rad, R., Schmidt-Supprian, M., and Saur, D. (2023). Context-Specific Determinants of the Immunosuppressive Tumor Microenvironment in Pancreatic Cancer. Cancer Discov. *13*, 278–297. https://doi.org/10.1158/2159-8290.CD-22-0876.

54. Mariathasan, S., Turley, S.J., Nickles, D., Castiglioni, A., Yuen, K., Wang, Y., Kadel, E.E., III, Koeppen, H., Astarita, J.L., Cubas, R., et al. (2018). TGFbeta attenuates tumour response to PD-L1 blockade by contributing to exclusion of T cells. Nature *554*, 544–548. https://doi.org/10.1038/nature25501.

55. Tai, S.B., Yang, J.L., Liu, P.F., and Chen, C.L. (2026). TGF-beta inhibitors in cancer therapy: a review of the TGF-beta signal transduction pathway and current developments. EXCLI J. *25*, 550–586. https://doi.org/10.17179/excli2026-9381.

56. Dobin, A., Davis, C.A., Schlesinger, F., Drenkow, J., Zaleski, C., Jha, S., Batut, P., Chaisson, M., and Gingeras, T.R. (2013). STAR: ultrafast universal RNA-seq aligner. Bioinformatics *29*, 15–21. https://doi.org/10.1093/bioinformatics/bts635.

57. Li, B., and Dewey, C.N. (2011). RSEM: accurate transcript quantification from RNA-Seq data with or without a reference genome. BMC Bioinf. *12*, 323. https://doi.org/10.1186/1471-2105-12-323.

58. Love, M.I., Huber, W., and Anders, S. (2014). Moderated estimation of fold change and dispersion for RNA-seq data with DESeq2. Genome Biol. *15*, 550. https://doi.org/10.1186/s13059-014-0550-8.

59. Howe, E.A., Sinha, R., Schlauch, D., and Quackenbush, J. (2011). RNA-Seq analysis in MeV. Bioinformatics *27*, 3209–3210. https://doi.org/10.1093/bioinformatics/btr490.

60. Huang, D.W., Sherman, B.T., and Lempicki, R.A. (2009). Systematic and integrative analysis of large gene lists using DAVID bioinformatics resources. Nat. Protoc. *4*, 44–57. https://doi.org/10.1038/nprot.2008.211.

61. Subramanian, A., Tamayo, P., Mootha, V.K., Mukherjee, S., Ebert, B.L., Gillette, M.A., Paulovich, A., Pomeroy, S.L., Golub, T.R., Lander, E.S., and Mesirov, J.P. (2005). Gene set enrichment analysis: a knowledge-based approach for interpreting genome-wide expression profiles. Proc. Natl. Acad. Sci. USA *102*, 15545–15550. https://doi.org/10.1073/pnas.0506580102.

62. Hänzelmann, S., Castelo, R., and Guinney, J. (2013). GSVA: gene set variation analysis for microarray and RNA-seq data. BMC Bioinf. *14*, 7. https://doi.org/10.1186/1471-2105-14-7.

63. Szklarczyk, D., Gable, A.L., Nastou, K.C., Lyon, D., Kirsch, R., Pyysalo, S., Doncheva, N.T., Legeay, M., Fang, T., Bork, P., et al. (2021). The STRING database in 2021: customizable protein-protein networks, and functional characterization of user-uploaded gene/measurement sets. Nucleic Acids Res. *49*, D605–D612. https://doi.org/10.1093/nar/gkaa1074.

64. Shannon, P., Markiel, A., Ozier, O., Baliga, N.S., Wang, J.T., Ramage, D., Amin, N., Schwikowski, B., and Ideker, T. (2003). Cytoscape: a software environment for integrated models of biomolecular interaction networks. Genome Res. *13*, 2498–2504. https://doi.org/10.1101/gr.1239303.

65. Fleming, S.J., Chaffin, M.D., Arduini, A., Akkad, A.D., Banks, E., Marioni, J.C., Philippakis, A.A., Ellinor, P.T., and Babadi, M. (2023). Unsupervised removal of systematic background noise from droplet-based single-cell experiments using CellBender. Nat. Methods *20*, 1323–1335. https://doi.org/10.1038/s41592-023-01943-7.

66. Wolock, S.L., Lopez, R., and Klein, A.M. (2019). Scrublet: Computational Identification of Cell Doublets in Single-Cell Transcriptomic Data. Cell Syst. *8*, 281–291.e9. https://doi.org/10.1016/j.cels.2018.11.005.

67. Wolf, F.A., Angerer, P., and Theis, F.J. (2018). SCANPY: large-scale single-cell gene expression data analysis. Genome Biol. *19*, 15. https://doi.org/10.1186/s13059-017-1382-0.

68. Polański, K., Young, M.D., Miao, Z., Meyer, K.B., Teichmann, S.A., and Park, J.E. (2020). BBKNN: fast batch alignment of single cell transcriptomes. Bioinformatics *36*, 964–965. https://doi.org/10.1093/bioinformatics/btz625.

69. Dimitrov, D., Türei, D., Garrido-Rodriguez, M., Burmedi, P.L., Nagai, J.S., Boys, C., Ramirez Flores, R.O., Kim, H., Szalai, B., Costa, I.G., et al. (2022). Comparison of methods and resources for cell-cell communication inference from single-cell RNA-Seq data. Nat. Commun. *13*, 3224. https://doi.org/10.1038/s41467-022-30755-0.

70. Meng, E.C., Goddard, T.D., Pettersen, E.F., Couch, G.S., Pearson, Z.J., Morris, J.H., and Ferrin, T.E. (2023). UCSF ChimeraX: Tools for structure building and analysis. Protein Sci. *32*, e4792. https://doi.org/10.1002/pro.4792.

71. Abramson, J., Adler, J., Dunger, J., Evans, R., Green, T., Pritzel, A., Ronneberger, O., Willmore, L., Ballard, A.J., Bambrick, J., et al. (2024). Accurate structure prediction of biomolecular interactions with AlphaFold 3. Nature *630*, 493–500. https://doi.org/10.1038/s41586-024-07487-w.

72. Goldman, M.J., Craft, B., Hastie, M., Repečka, K., McDade, F., Kamath, A., Banerjee, A., Luo, Y., Rogers, D., Brooks, A.N., et al. (2020). Visualizing and interpreting cancer genomics data via the Xena platform. Nat. Biotechnol. *38*, 675–678. https://doi.org/10.1038/s41587-020-0546-8.

73. Tang, Z., Kang, B., Li, C., Chen, T., and Zhang, Z. (2019). GEPIA2: an enhanced web server for large-scale expression profiling and interactive analysis. Nucleic Acids Res. *47*, W556–W560. https://doi.org/10.1093/nar/gkz430.

74. Bankhead, P., Loughrey, M.B., Fernández, J.A., Dombrowski, Y., McArt, D.G., Dunne, P.D., McQuaid, S., Gray, R.T., Murray, L.J., Coleman, H.G., et al. (2017). QuPath: Open source software for digital pathology

image analysis. Sci. Rep. *7*, 16878. https://doi.org/10.1038/s41598-017-17204-5.

75. Johnson, L., Mercer, K., Greenbaum, D., Bronson, R.T., Crowley, D., Tuveson, D.A., and Jacks, T. (2001). Somatic activation of the K-ras oncogene causes early onset lung cancer in mice. Nature *410*, 1111–1116. https://doi.org/10.1038/35074129.

76. Jeong, W.J., Yoon, J., Park, J.C., Lee, S.H., Lee, S.H., Kaduwal, S., Kim, H., Yoon, J.B., and Choi, K.Y. (2012). Ras stabilization through aberrant activation of Wnt/beta-catenin signaling promotes intestinal tumorigenesis. Sci. Signal. *5*, ra30. https://doi.org/10.1126/scisignal.2002242.

77. Wang, R., Wu, J., Lin, Y., Xiao, Y., Yang, B., Yao, S., Pan, T., Fu, Z., Li, S., Wang, C., and Zhu, Y. (2025). An epitope-directed mRNA vaccine inhibits tumor metastasis through the blockade of MICA/B alpha1/2 shedding. Cell Rep. Med. *6*, 101981. https://doi.org/10.1016/j.xcrm.2025.101981.

78. Zhang, Z., Huang, W., Hu, D., Jiang, J., Zhang, J., Wu, Z., Wen, J., Luo, X., Wang, Y., Sun, M., et al. (2025). E-twenty-six-specific sequence variant 5 (ETV5) facilitates hepatocellular carcinoma progression and metastasis through enhancing polymorphonuclear myeloid-derived suppressor cell (PMN-MDSC)-mediated immunosuppression. Gut *74*, 1137–1149. https://doi.org/10.1136/gutjnl-2024-333944.

79. Kang, D.W., Choi, C.Y., Cho, Y.H., Tian, H., Di Paolo, G., Choi, K.Y., and Min, D.S. (2015). Targeting phospholipase D1 attenuates intestinal tumorigenesis by controlling beta-catenin signaling in cancer-initiating cells. J. Exp. Med. *212*, 1219–1237. https://doi.org/10.1084/jem.20141254.

80. Goldsborough, T., Philps, B., O'Callaghan, A., Inglis, F., Leplat, L., Filby, A., Bilen, H., and Bankhead, P. (2024). InstanSeg: an embedding-based instance segmentation algorithm optimized for accurate, efficient and portable cell segmentation. Preprint at arXiv. https://doi.org/10.48550/arXiv.2408.15954.

81. Goldsborough, T., O'Callaghan, A., Inglis, F., Leplat, L., Filby, A., Bilen, H., and Bankhead, P. (2024). A novel channel invariant architecture for the segmentation of cells and nuclei in multiplexed images using InstanSeg. Preprint at bioRxiv. https://doi.org/10.1101/2024.09.04.611150.

82. Paszke, A., Gross, S., Massa, F., Lerer, A., Bradbury, J., Chanan, G., Killeen, T., Lin, Z., Gimelshein, N., and Antiga, L. (2019). PyTorch: An imperative style, high-performance deep learning library. Adv. Neural Inf. Process. Syst. *32*.

83. Zheng, G.X.Y., Terry, J.M., Belgrader, P., Ryvkin, P., Bent, Z.W., Wilson, R., Ziraldo, S.B., Wheeler, T.D., McDermott, G.P., Zhu, J., et al. (2017). Massively parallel digital transcriptional profiling of single cells. Nat. Commun. *8*, 14049. https://doi.org/10.1038/ncomms14049.

CellPress
OPEN ACCESS

STAR★METHODS

KEY RESOURCES TABLE

REAGENT or RESOURCE	SOURCE	IDENTIFIER
Antibodies		
Brilliant Violet 421 anti-Mouse Ly-6G [1A8]; Monoclonal	BioLegend	Cat#127628; RRID: AB_2562567
Brilliant Violet 421 anti-Mouse CD3 [17A2]; Monoclonal	BioLegend	Cat#100228; RRID: AB_2562553
Brilliant Violet 421 anti-Mouse I-A/I-E Antibody [M5/114.15.2]	BioLegend	Cat#107632; RRID: AB_2650896
Brilliant Violet 421 anti-Mouse CD86 Antibody [GL-1]	BioLegend	Cat#105032; RRID: AB_2650895
Brilliant Violet 421 anti-Mouse FOXP3 [MF-14]; Monoclonal	BioLegend	Cat#126419; RRID: AB_2565933
Brilliant Violet 421 anti-Mouse CD8a [53-6.7]; Monoclonal	BioLegend	Cat#100738; RRID: AB_11204079
Brilliant Violet 421 anti-Mouse CD47 [miap301]; Monoclonal	BioLegend	Cat#127527; RRID: AB_2734196
Brilliant Violet 510 anti-Mouse CD25 [PC61]; Monoclonal	BioLegend	Cat#102042; RRID: AB_2562270
Brilliant Violet 510 anti-Mouse CD45 [30-F11]; Monoclonal	BioLegend	Cat#103138; RRID: AB_2561392
Brilliant Violet 510 anti-Mouse CD8a [53-6.7]; Monoclonal	BioLegend	Cat#100752; RRID: AB_2563057
Brilliant Violet 510 anti-Mouse CD4 [GK1.5]; Monoclonal	BioLegend	Cat#100449; RRID: AB_2564587
Brilliant Violet 510 anti-Mouse CD3 [17A2]; Monoclonal	BioLegend	Cat#100234; RRID: AB_2562555
Brilliant Violet 510 anti-Human CD14 Antibody [M5E2]; Monoclonal	BioLegend	Cat#301842; RRID: AB_2561946
Brilliant Violet 605 anti-Mouse I-A/I-E [M5/114.15.2]; Monoclonal	BioLegend	Cat#107639; RRID: AB_2565894
Brilliant Violet 650 anti-Mouse Ly-6C [HK1.4]; Monoclonal	BioLegend	Cat#128049; RRID: AB_2800630
Brilliant Violet 650 anti-Human CD15 Antibody [W6D3]; Monoclonal	BioLegend	Cat#323034; RRID: AB_2563840
PerCP anti-mouse/human CD11b [M1/70]; Monoclonal	BioLegend	Cat#101229; RRID: AB_2129374
PerCP anti-Mouse CD4 [GK1.5]	BioLegend	Cat#100432; RRID: AB_893323
PerCP anti-Mouse CD45 [30-F11]; Monoclonal	BioLegend	Cat#103130; RRID: AB_893339
PerCP anti-Mouse CD90.2 (Thy1.2) [30-H12]; Monoclonal	BioLegend	Cat#105322; RRID: AB_893453
PerCP anti-Human CD45 Antibody [HI30]; Monoclonal	BioLegend	Cat#304026; RRID: AB_893337
FITC anti-Mouse Ly-6C [HK1.4]; Monoclonal	BioLegend	Cat#128006; RRID: AB_1186135
FITC anti-mouse/human CD44 Antibody [IM7]; Monoclonal	BioLegend	Cat#103022; RRID: AB_493685
FITC anti-Mouse Ly-6G/Ly-6C (Gr-1) [RB6-8C5]; Monoclonal	BioLegend	Cat#108406; RRID: AB_313371
FITC anti-Mouse CD25 [PC61]; Monoclonal	BioLegend	Cat#102006; RRID: AB_312855
FITC anti-Mouse CD8a [53-6.7]; Monoclonal	BioLegend	Cat#100706; RRID: AB_312745
FITC anti-Mouse CD11c [N418]; Monoclonal	BioLegend	Cat#117306; RRID: AB_313775
FITC anti-Mouse CD279 (PD-1) [29F.1A12]; Monoclonal	BioLegend	Cat#135214; RRID: AB_10680238
FITC anti-Mouse CD3 [17A2]; Monoclonal	BioLegend	Cat#100204; RRID: AB_312661
BD Pharmingen FITC Rat Anti-Mouse CD31 [MEC13.3]; Monoclonal	BD Biosciences	Cat#553372; RRID: AB_394818
PE anti-Mouse CD49b (pan-NK cells) [DX5]; Monoclonal	BioLegend	Cat#108908; RRID: AB_313415
PE anti-Mouse CD8a [53-6.7]; Monoclonal	BioLegend	Cat#100708; RRID: AB_312747
PE anti-Mouse CD19 [6D5]; Monoclonal	BioLegend	Cat#115508; RRID: AB_313643
PE anti-Mouse CD206 (MMR) [C068C2]; Monoclonal	BioLegend	Cat#141706; RRID: AB_10895754
PE anti-Mouse CD4 [GK1.5]; Monoclonal	BioLegend	Cat#100408; RRID: AB_312693

(*Continued on next page*)

Continued

REAGENT or RESOURCE	SOURCE	IDENTIFIER
PE anti-Mouse IFN-γ [XMG1.2]; Monoclonal	BioLegend	Cat#505808; RRID: AB_315402
PE anti-Mouse F4/80 [BM8]; Monoclonal	BioLegend	Cat#123109; RRID: AB_893498
PE anti-mouse/human CD44 [IM7]; Monoclonal	BioLegend	Cat#103008; RRID: AB_312959
PE anti-Mouse NK-1.1 [PK136]; Monoclonal	BioLegend	Cat#108707; RRID: AB_313394
PE anti-Mouse Podoplanin [8.1.1]; Monoclonal	BioLegend	Cat#127408; RRID: AB_2161928
PE/Cyanine7 anti-Mouse NK-1.1 [PK136]; Monoclonal	BioLegend	Cat#108714; RRID: AB_389364
PE/Cyanine7 anti-Mouse CD11c [N418]; Monoclonal	BioLegend	Cat#117318; RRID: AB_493568
PE/Cyanine7 anti-mouse/human Ki-67 [11F6]; Monoclonal	BioLegend	Cat#151218; RRID: AB_2910305
PE/Cyanine7 anti-Mouse Ly-6G [1A8]; Monoclonal	BioLegend	Cat#127618; RRID: AB_1877261
PE/Cyanine7 anti-Mouse CD4 [GK1.5]; Monoclonal	BioLegend	Cat#100422; RRID: AB_312707
PE/Cyanine7 anti-Mouse CD127 [A7R34]; Monoclonal	BioLegend	Cat#135014; RRID: AB_1937265
PE/Cyanine7 anti-Mouse F4/80 [BM8]; Monoclonal	BioLegend	Cat#123114; RRID: AB_893478
APC anti-Mouse CD3 [17A2]; Monoclonal	BioLegend	Cat#100236; RRID: AB_2561456
APC anti-Mouse CD62L [MEL-14]; Monoclonal	BioLegend	Cat#104412; RRID: AB_313099
APC anti-Mouse F4/80 [BM8]; Monoclonal	BioLegend	Cat#123116; RRID: AB_893481
APC anti-Mouse Ly-6C [HK1.4]; Monoclonal	BioLegend	Cat#128016; RRID: AB_893481
APC anti-Mouse CD49b (pan-NK cells) [DX5]; Monoclonal	BioLegend	Cat#108909; RRID: AB_313416
APC anti-Mouse I-A/I-E [M5/114.15.2]; Monoclonal	BioLegend	Cat#107614; RRID: AB_3741415
APC anti-Mouse CD69 [H1.2F3]; Monoclonal	BioLegend	Cat#104514; RRID: AB_492843
APC/Cyanine7 anti-Mouse CD19 [6D5]; Monoclonal	BioLegend	Cat#115530; RRID: AB_830707
Alexa Fluor 488 anti-Mouse CD74 (CLIP) [In1/CD74]; Monoclonal	BioLegend	Cat#151006; RRID: AB_2750326
Alexa Fluor 488 anti-mouse-TCF1/TCF7; Rabbit mAb	Cell Signaling Technology	Cat#6444; RRID: AB_2797627
PE/Dazzle 594 anti-Mouse H-2K bound to SIINFEKL Antibody	BioLegend	Cat# 141612; RRID: AB_2750522
Alexa Fluor 700 anti-Mouse CD31 [390]; Monoclonal	BioLegend	Cat#102444; RRID: AB_2832289
Alexa Fluor 647, anti-Mouse p-Stat5(pY694) [47/p-Stat5(pY694)]; Monoclonal	BD Biosciences	Cat#562076; RRID: AB_11154412
anti-Mouse CD16/32	BioLegend	Cat#101301; RRID: AB_312800
Anti-Phospho-SMAD2/SMAD3 (Ser465, Ser467, Ser423, Ser425)	Invitrogen	Cat#PA5-110155; RRID: AB_2855566
CD8a Antibody	Invitrogen	Cat#14-0808-82; RRID: AB_2572861
Anti-alpha smooth muscle Actin antibody	Cell Signaling Technology	Cat #19245; RRID: AB_2734735
Anti-Fibronectin antibody	Abcam	Cat#ab2413; RRID: AB_2262874
Anti-CD31 antibody [EPR17259]	Abcam	Cat#ab182981; RRID: AB_2920881
H2-Ab1 Rabbit mAb	Abclonal	Cat#A24650; RRID: AB_3713138
Anti-CD8 alpha antibody [RM1129]	Abcam	Cat#ab316778; RRID: AB_3107047
Recombinant HLA-DP (MHC II) Antibody [rHLA-Pan/3475]	NeoBiotechnologies	Cat# MSM2-3475; RRID: AB_3753785
Alexa 488, Anti-Mouse IgG (H + L), F(ab')2	Cell Signaling Technology	Cat#4408S; RRID: AB_10694704
Alexa 555, Anti-Mouse IgG (H + L), F(ab')2	Cell Signaling Technology	Cat#4409S; RRID: AB_1904022
Alexa 647, Anti-Mouse IgG (H + L), F(ab')2	Cell Signaling Technology	Cat#4410S; RRID: AB_1904023
Alexa 488, Anti-Rabbit IgG (H + L), F(ab')2	Cell Signaling Technology	Cat#4412S; RRID: AB_1904025
Alexa 555, Anti-Rabbit IgG (H + L), F(ab')2	Cell Signaling Technology	Cat#4413S; RRID: AB_10694110
Alexa 647, Anti-Rabbit IgG (H + L), F(ab')2	Cell Signaling Technology	Cat#4414S; RRID: AB_10693544
Alexa 488, Anti-Human IgG (H + L)	Invitrogen	Cat#A11013; RRID: AB_141360
Alexa 555, Anti-Human IgG (H + L)	Invitrogen	Cat#A21433; RRID: AB_1500626
Alexa 647, Anti-Human IgG (H + L)	Invitrogen	Cat#A21445; RRID: AB_2535862
Alexa 647, Anti-Rat IgG (H + L)	Cell Signaling Technology	Cat#4418S; RRID: AB_1904017
human TβRII Biotinylated Antibody	R&D	Cat#BAF241; RRID: AB_356321

(*Continued on next page*)

Continued

REAGENT or RESOURCE	SOURCE	IDENTIFIER
HRP, Anti Mouse IgG (H + L)	Invitrogen	Cat#31430; RRID: AB_228307
HRP, Anti-Rabbit IgG	Cell Signaling Technology	Cat#7074S; RRID: AB_2099233
HRP, Anti-Rat IgG (H&L) Biotin	Abcam	Cat#ab207997
Peroxidase AffiniPure Goat Anti-Human IgG, Fcγ fragment specific	Jackson ImmunoResearch	Cat#109-035-008; RRID: AB_2337579
InVivoMAb anti-Mouse CD4 (clone GK1.5)	Bio X Cell	Cat#BE0003-1; RRID: AB_1107636
InVivoMAb anti-Mouse CD8a (clone 2.43)	Bio X Cell	Cat#BE0061; RRID: AB_1125541
InVivoMAb anti-Mouse IFN-γ (clone XMG1.2)	Bio X Cell	Cat#BE0055; RRID: AB_1107694
InVivoMAb polyclonal rat IgG	Bio X Cell	Cat#BE0094; RRID: AB_1107795
InVivoMAb anti-Mouse NK1.1 (clone PK136)	Bio X Cell	Cat#BE0036; RRID: AB_1107737
InVivoMAb anti-PD-1 (J43) antibody	Bio X Cell	Cat#BE0033-2; RRID: AB_1107747
Ax647-conjugated goat anti-Human IgG	Thermo Fisher Scientific	Cat#A21445; RRID: AB_2535862
human TβRII Biotinylated Antibody	R&D	Cat#BAF241; RRID: AB_356321
Anti-pSMAD2 (Ser465/467), clone 138D4	Cell Signaling Technology	Cat#3108; RRID: AB_490941
Anti-β-actin (clone D6A8)	Cell Signaling Technology	Cat#8457; RRID: AB_10950489
anti-PD-1 (J43) antibody	This paper	N/A
anti-PD-L1 (Avelumab) antibody	This paper	N/A
Bs-*anti*-PD-1 (J43)-sTβRII antibody	This paper	N/A
Bs-*anti*-PD-L1 (Avelumab)-sTβRII antibody	This paper	N/A
Chemicals, peptides, and recombinant proteins		
viability dye 780	Biogems	Cat#62910-00-100
viability dye 450	Biogems	Cat#62510-00-100
anti-CD45 microbeads	Miltenyi Biotec	Cat#130-052-301; RRID: AB_2877061
recombinant human TGF-β1	PeproTech	Cat#100-21C
Mouse IL-4 Recombinant Protein	PeproTech	Cat#214-14
Human IL-7 recombinant Protein	PeproTech	Cat#AF-200-07
Mouse IL-15 recombinant Protein	PeproTech	Cat#210-15
Mouse M-CSF Recombinant Protein	PeproTech	Cat# 315-02
PROLEUKIN (Human IL-2)	CLINIGEN	Cat#076100031R
bovine serum albumin (BSA)	TOCRIS	Cat#5217
FN-EDB-Fc	This paper	N/A
biotinylated TGF-β1	R&D Systems	Cat#NFTG0
Recombinant Mouse GM-SCF Protein	R&D Systems	Cat#415-ML
T-PER Tissue Protein Extraction Reagent	Thermo Fisher Scientific	Cat#78510
cOmplete Mini, EDTA-free protease inhibitor	Roche	Cat#11836170001
PhosStop phosphatase inhibitor	Roche	Cat#4906845001
Ovalbumin (257–264) chicken; SIINFEKL	Sigma-Aldrich	Cat#S7951
Ovalbumin (323–339) (chicken, Japanese quail)	Sigma-Aldrich	Cat#O1641
Lipopolysaccharides from *Escherichia coli* 0111:B4	Sigma-Aldrich	Cat#L2630
control-Fc (Control)	This paper	N/A
control-IgG types	This paper	N/A
Fc-sTβRII (sTβRII)	This paper	N/A
FEBP-Fc-sTβRII (FEBP-sTβRII)	This paper	N/A
Fc-FEBP-sTβRII	This paper	N/A
Fc-sTβRII-FEBP formats	This paper	N/A
FEBP-Fc-FEBP-sTβRII formats	This paper	N/A
FEBP-Fc-sTβRII-FEBP formats	This paper	N/A
Fc-FEBP-sTβRII-FEBP formats	This paper	N/A
2FEBP-Fc-sTβRII formats	This paper	N/A
Fc-2FEBP-sTβRII formats	This paper	N/A

(*Continued on next page*)

Continued

REAGENT or RESOURCE	SOURCE	IDENTIFIER
Fc-sTβRII-2FEBP formats	This paper	N/A
Fc-mutFEBP-sTβRII (mutFEBP-sTβRII)	This paper	N/A
sTβRII-Fc	This paper	N/A
sTβRII-FEBP-Fc	This paper	N/A
sTNFR2-Fc	This paper	N/A
Critical commercial assays		
ExpiCHO expression system kit	Thermo Fisher Scientific	Cat#A29133
Expi293 PRO expression system kit	Thermo Fisher Scientific	Cat#A14635
Mouse tumor-associated fibroblast isolation kit	Miltenyi Biotec	Cat#130-116-474
MidiMACS Separator and Starting Kits (LD)	Miltenyi Biotec	Cat#130-090-329
MiniMACS Separator and Starting Kit	Miltenyi Biotec	Cat#130-090-312
CD11c MicroBeads UltraPure mouse	Miltenyi Biotec	Cat#130-125-835
CD8 (TIL) MicroBeads, mouse	Miltenyi Biotec	Cat#130-116-478
CD4 (TIL) MicroBeads, mouse	Miltenyi Biotec	Cat#130-116-475
Pharmingen Transcription Factor Buffer Set	BD Biosciences	Cat#562725
BD GolgiStop Protein Transport Inhibitor	BD Biosciences	Cat#554724
eBioscience Intracellular Fixation & Permeabilization Buffer Set	Thermo Fisher Scientific	Cat#88-8824-00
eBioscience Foxp3/Transcription Factor Staining Buffer Set	Thermo Fisher Scientific	Cat#00-5523-00
GeneArt Precision gRNA Synthesis Kit	chem	Cat#A29377
AccuPower PCR Premix	Bioneer	Cat#K-2011
Lenti-X Concentrator	TaKaRa	Cat#631232
D-luciferin	PerkinElmer	Cat#122799
Cy5 dye	Abcam	Cat#ab146456
Mouse TGF-β1 DuoSet ELISA kit	R&D Systems	Cat#DY1679
Mouse IFN-gamma ELISpot Kit	R&D Systems	Cat#XEL485
VECTASTAIN Elite ABC-HRP Kit	VectorLabs	Cat#PK-6103
Splink HRP Rabbit DAB Detection kit	ORIGENE	Cat#D03-110
VivoGlo Luciferin	Promega	Cat#P1043
Hybrid-R	GeneAll	Cat#305-101
RiboPure RNA Purification Kit, blood	Invitrogen	Cat#AM1928
PrimeScript RT Master Mix	TaKaRa	Cat#RR036A
TaqMan Gene Expression Master Mix	Applied Biosystems	Cat#4369016
iTaq Universal SYBR Green Supermix	Bio-Rad	Cat#1725121
TruSeq Stranded Total RNA kit with Ribo-Zero H/M/R	Illumina	Cat# 88-8824-00
Chromium GEM-X Single Cell 3′ Kit v4	10× Genomics	Cat#PN1000691
ELISpot Flex: Mouse IFN γ (HRP)	Mabtech	Cat#3321-2H
ELISpot plates, white	Mabtech	Cat#3654-WP-10
ELISpot substrate: TMB for HRP	Mabtech	Cat#3651-10
Deposited data		
RNA-seq raw data	This paper	BioProject: PRJNA1241682
Single-cell RNA-seq raw data	This paper	BioProject: PRJNA1241682
Human PDAC, MSS CRC immunotherapy cohort	NCBI Gene Expression Omnibus (GEO)	GEO: GSE179351[35]
Human metastatic gastric cancer immunotherapy cohort	Kim et al.[36]	TIDE database(http://tide.dfci.harvard.edu/download/); ENA:PRJEB25780
Human melanoma immunotherapy cohort	Gide et al.[37]	TIDE database(http://tide.dfci.harvard.edu/download/); ENA:PRJEB23709

(*Continued on next page*)

Continued

REAGENT or RESOURCE	SOURCE	IDENTIFIER
Mus musculus GRCm38 (Ensembl Release 99)	Ensembl	https://www.ncbi.nlm.nih.gov/datasets/genome/GCF_000001635.20/
Experimental models: Cell lines		
HEK293T (human embryonic kidney)	ATCC	Cat#CRL-3216; RRID: CVCL_0063
MiaPaCa-2 (human pancreatic cancer)	ATCC	Cat#CRL-1420; RRID: CVCL_0428
4T-1-Luc (murine breast cancer expressing Luciferase)	ATCC	Cat#CRL-2539-LUC2; RRID: CVCL_A4BM
4T-1-Luc-LMT-2 (murine breast cancer expressing Luciferase)	This paper	N/A
CT26 (murine colorectal cancer)	ATCC	Cat#CRL-2638; RRID: CVCL_7256
B16F10 (murine melanoma)	ATCC	Cat#CRL-6475; RRID: CVCL_0159
B16F10-Luc (murine melanoma expressing Luciferase)	UBIGENE	Cat#YC-A011-Luc-P; RRID: CVCL_C8XU
B16-OVA MO4 (murine melanoma expressing OVA)	Sigma-Aldrich	Cat#SCC420; RRID: CVCL_WM78
RM1 (murine prostate cancer)	ATCC	Cat#CRL-3310; RRID: CVCL_B459
Lewis lung carcinoma (LLC, murine lung cancer)	ATCC	Cat#CRL-1642; RRID: CVCL_4358
MB49 (murine bladder cancer)	Sigma-Aldrich	Cat#SCC148; RRID: CVCL_7076
PANCO2-OVA-Luc ((murine pancreatic cancer expressing OVA)	Vitro Biotech	Cat#VOA4B040
Hepa1-6 (murine hepatoma)	Vanderbilt University	Cat#CRL-1830; RRID: CVCL_0327
GL26 (murine glioblastoma)	Cedars-Sinai Medical Center	N/A
PANC02 (murine pancreatic cancer)	Chungnam National University, Republic of Korea)	N/A
PANC02-Luc (murine pancreatic cancer expressing Luciferase)	This paper	N/A
PKCY (murine PDAC; Pdx1-cre; LSL-K-Ras$^{G12D/+}$; TP53$^{fl/+}$; R26^{YFP})	UT MD Anderson Cancer Center	N/A
PKCY-Luc (murine PDAC expressing Luciferase; Pdx1-cre; LSL-K-Ras$^{G12D/+}$; TP53$^{fl/+}$; R26^{YFP})	This paper	N/A
KPC-Luc (C57BL/6N.129Cya-Kras$^{tm1(LSL-G12D)}$ Trp53$^{tm1(LSL-R172H)}$Tg(Pdx1-Cre)/Cya, murine PDAC, Custom-synthesized Luciferase)	Cyagen	N/A
KP-PSAFs (K-Ras^{LA1}; TP53$^{-/-}$ Sarcoma associated fibroblasts)	This paper	N/A
KP-PSAFs-ΔEDB (K-Ras^{LA1}; TP53$^{-/-}$ Sarcoma associated fibroblasts with *Fn1-EDB* knockout	This paper	N/A
Experimental models: Organisms/strains		
OT-I mice(C57BL/6-Tg(TcraTcrb)1100Mjb/J [OT-I])	The Jackson Laboratory	Cat#003831; RRID: IMSR_JAX:003831
OT-II mice(B6.Cg-Tg(TcraTcrb)425Cbn/J)	The Jackson Laboratory	Cat#004194; RRID: IMSR_JAX:004194
C57BL/6J mice (male, 6–10 weeks old)	Doo-Yeol Biotech (Seoul, Korea) or Orient Bio Inc. (Seongnam, Korea)	N/A
BALB/c mice (female, 6–10 weeks old)	Doo-Yeol Biotech (Seoul, Korea) or Orient Bio Inc. (Seongnam, Korea)	N/A
Rag1$^{-/-}$ (B6.129S7-*Rag1*$^{tm1Mom/J}$)	The Jackson Laboratory	Cat#002216; RRID: IMSR_JAX:002216
B6.45.1 (B6.SJL-Ptprca Pepcb/BoyJ)	The Jackson Laboratory	Cat#002014; RRID: IMSR_JAX:002014
huHSC-NKG-ProF (female, 11–16 weeks old)	Cyagen	Cat#C001543
K-Ras^{LA1} mice (heterozygous)	Dr. YA Suh (MD Anderson Cancer Center	N/A
TP53$^{-/-}$ mice (homozygous)	Dr. YA Suh (MD Anderson Cancer Center	N/A
K-Ras^{LA1} TP53$^{-/-}$ mice (homozygous)	Dr. YA Suh (MD Anderson Cancer Center	N/A

(*Continued on next page*)

Continued

REAGENT or RESOURCE	SOURCE	IDENTIFIER
APC$^{1638N/+}$ mice (heterozygous)	Dr. KY Choi (Yonsei University)	N/A
APC$^{1638N/+}$/*TP53*$^{-/-}$ (AP)	This paper	N/A
Oligonucleotides		
Genotyping primers (see Table S1)	This paper	N/A
SYBR Green qRT-PCR primers (see Table S1)	This paper	N/A
TaqMan qRT-PCR probes (see Table S1)	Integrated DNA Technologies (IDT)	Various, see Table S1
Recombinant DNA		
psPAX2 (packaging plasmid)	Addgene	Cat#12260; RRID: Addgene_12260
pMD2.G (envelope plasmid)	Addgene	Cat#12259; RRID: Addgene_12259
DNA fragments for control-Fc (mouse IgG1, mouse IgG2a, human IgG4, human IgG1)	Bionics	N/A
DNA fragments for control-IgG types	Bionics	N/A
DNA fragments for Fc-sTβRII	Bionics	N/A
DNA fragments for FEBP-Fc-sTβRII formats	Bionics	N/A
DNA fragments for Fc-FEBP-sTβRII formats	Bionics	N/A
DNA fragments for Fc-sTβRII-FEBP formats	Bionics	N/A
DNA fragments for FEBP-Fc-FEBP-sTβRII formats	Bionics	N/A
DNA fragments for FEBP-Fc-sTβRII-FEBP formats	Bionics	N/A
DNA fragments for Fc-FEBP-sTβRII-FEBP formats	Bionics	N/A
DNA fragments for 2FEBP-Fc-sTβRII formats	Bionics	N/A
DNA fragments for Fc-2FEBP-sTβRII formats	Bionics	N/A
DNA fragments for Fc-sTβRII-2FEBP formats	Bionics	N/A
DNA fragments for Fc-mutFEBP-sTβRII formats	Bionics	N/A
DNA fragments for sTβRII-Fc	Bionics	N/A
DNA fragments for sTβRII-FEBP-Fc	Bionics	N/A
DNA fragments for sTNFR2-Fc	Bionics	N/A
DNA fragments for anti-PD-1 (J43) antibody	Bionics	N/A
DNA fragments for anti-PD-L1 (Avelumab) antibody	Bionics	N/A
DNA fragments for Bs-*anti*-PD-1 (J43)-sTβRII antibody	Bionics	N/A
DNA fragments for Bs-*anti*-PD-L1 (Avelumab)-sTβRII antibody	Bionics	N/A
Software and algorithms		
STAR (v2.4.0b)	Dobin et al.[56]	http://code.google.com/p/rna-star/; RRID: SCR_004463
RSEM (v1.3.1)	Li et al.[57]	https://deweylab.github.io/RSEM/; RRID: SCR_000262
DESeq2 (v 1.44)	Love et al.[58]	https://www.bioconductor.org/packages/release/bioc/html/DESeq2.html; RRID: SCR_015687
MultiExperiment Viewer (MeV)	Howe et al.[59]	https://mev.tm4.org
DAVID (v 6.8)	Huang et al.[60]	https://davidbioinformatics.nih.gov/summary.jsp; RRID: SCR_001881
GSEA (v 4.4.4)	Subramanian et al.[61]	http://software.broadinstitute.org/gsea/index.jsp; RRID: SCR_003199
"GSVA" method	Hanzelmann et al.[62]	https://bioconductor.org/packages/release/bioc/html/GSVA.html; RRID: SCR_021058
STRING	Szklarczyk et al.[63]	https://string-db.org/; RRID: SCR_005223

(*Continued on next page*)

Continued

REAGENT or RESOURCE	SOURCE	IDENTIFIER
Cytoscape (v 3.10.0); with ClueGO/CluePedia	Shannon et al.[64]	https://cytoscape.org/; RRID: SCR_003032
CellRanger (v 9.0.1)	10× Genomics	https://github.com/10XGenomics/cellranger; RRID: SCR_023221
CellBender (v 0.3.2)	Fleming et al.[65]	https://github.com/broadinstitute/CellBender; RRID: SCR_025990
Scrublet (v 0.2.3)	Wolock et al.[66]	https://github.com/swolock/scrublet; RRID: SCR_018098
Scanpy (v 1.10.4)	Wolf et al.[67]	https://github.com/scverse/scanpy; RRID: SCR_018139
BBKNN (v 1.6.0)	Polański et al.[68]	https://github.com/Teichlab/bbknn; RRID: SCR_022807
LIANA framework (v1.5.1), CellPhoneDB	Dimitrov et al.[69]	https://saezlab.github.io/liana/; RRID: SCR_027830
ChimeraX (v1.7.1)	Meng et al.[70]	https://www.rbvi.ucsf.edu/chimerax/; RRID: SCR_015872
AlphaFold3	Abramson et al.[71]	https://alphafoldserver.com/welcome; RRID: SCR_028034
UCSC Xena	Goldman et al.[72]	https://xena.ucsc.edu/; RRID: SCR_018938
GEPIA2	Tang et al.[73]	http://gepia2.cancer-pku.cn/#index RRID: SCR_026154
BD FACSDiva software (v8.0.2)	BD Biosciences	https://www.bdbiosciences.com/sg/instruments/software/; RRID: SCR_001456
CytExpert software (v2.6)	Beckman Coulter	https://www.beckman.com/coulter-flow-cytometers/cytoflex/cytexpert; RRID: SCR_017217
FlowJo (v10.8.1)	TreeStar	https://www.flowjo.com/; RRID: SCR_008520
Living Image software (v.4.7.3)	PerkinElmer	https://www.perkinelmer.com/lab-products-and-services/resources/in-vivo-imaging-software-downloads.html#LivingImage; RRID: SCR_014247
ZEN software (v2.6 blue edition)	Zeiss	https://www.zensoftware.cloud/; RRID: SCR_013672
i-control software (v2.0)	TECAN	RRID: SCR_024562
Amersham Imager 680 Analysis Software (v.2.0)	Cytiva	N/A
quantstudio design and analysis software (v1.4.3).	Applied Biosystems	N/A
GraphPad Prism (v10.1.2).	GraphPad Software	https://www.graphpad.com/scientific-software/prism/; RRID: SCR_002798
QuPath software (v0.5.1)	Bankhead et al.[74]	https://qupath.github.io; RRID: SCR_018257
Other		
NovaSeq 6000	Illumina	Ref#20012850; RRID: SCR_016387
BD Canto II	BD Biosciences	BD FACS CANTO II; RRID: SCR_018056
BD FACSAria Fusion Flow Cytometer	BD Bioscience	Cat#656700; RRID: SCR_025715
CytoFLEX	Beckman Coulter	CytoFLEX S; RRID: SCR_027083
IVIS Spectrum optical scanner	PerkinElmer	Lumina S5; RRID: SCR_025239
Zeiss Axio scan Z1 slide scanner	Zeiss	Axio scan.Z1; RRID: SCR_020927
Zeiss LSM800 confocal microscope	Zeiss	LSM800; RRID: SCR_015963

(*Continued on next page*)

Continued

REAGENT or RESOURCE	SOURCE	IDENTIFIER
Infinite M Plex microplate reader	TECAN	TECAN Microplate Reader M-PI; RRID: SCR_026522
Cytiva Amersham Imager 680	Cytiva	Amersham Imager 680
QuantStudio5	Applied Biosystems	QuantStudio5; RRID: SCR_020240
AKTA Pure M150	Cytiva	AKTA Pure M150; RRID: SCR_019958
Superdex S200 10/300 GL column	Cytiva	Cat#28-9909-44
Endosafe LAL cartridge system (Endosafe MS)	Charles River	Cat#PTS55005F
Protein A prepacked gravity flow column	Cytiva	Cat#28-9852-54
ImmunoSpot S5UV	C.T.L. Analyzer LLC	N/A
TissueLyser III Bead Mill Homogenizer	QIAGEN	Cat#9003240

EXPERIMENTAL MODEL AND STUDY PARTICIPANT DETAILS

Syngeneic mice

Male C57BL/6J *wild-type* CD45.1 and CD45.2 mice and female BALB/c mice about 6–10 weeks old were purchased from Doo-Yeol Biotech (Seoul, Korea) or Orient Bio Inc. (Seongnam, Korea). *Rag1*$^{-/-}$ mice (lacking T- and B-cells; B6.129S7-*Rag1*^{tm1Mom}/J: #002216) and C57BL/6J *wild-type* CD45.1 mice (B6.SJL-*Ptprc*^{a} *Pepc*^{b}/BoyJ: #002214) were purchased from the Jackson Laboratory. The heterozygous *K-Ras*^{LA1} mice[75] were crossed with homozygous *TP53*$^{-/-}$ mice (both kindly provided by Dr. YA Suh, The University of Texas M. D. Anderson Cancer Center, Houston, TX, USA) to generate *K-Ras*^{LA1}/*TP53*$^{-/-}$ (*KP*) and *wild-type* mice. The heterozygous *APC*$^{1638N/+}$ mice[76] (both kindly provided by Dr. KY Choi, Yonsei University, Seoul, Republic of Korea) were crossed with homozygous *TP53*$^{-/-}$ mice to generate *APC*$^{1638N/+}$/*TP53*$^{-/-}$ (AP) and *wild-type* mice. All genotype primers used in this study are listed in Table S1J. All mice were maintained under specific pathogen-free conditions with 10/14 dark/light cycle, 20°C–26°C, and 30–70% humidity. All experimental protocols were approved by the Institutional Animal Care and Use Committee (IACUC) of MedPacto, Inc. (Authorization No. M-IACUC-2020-0024 for *KP* and *AP* mice studies, M-IACUC-2024-0006-02, M-IACUC-2023-0012, M-IACUC-2025-0001 and M-IACUC-2026-0006 for murine breast, melanoma and pancreatic tumor models, M-IACUC-2023-0007 for *Rag1*$^{-/-}$ mice studies).

Humanized mice

All animal procedures using 10-week-old, female huHSC-NKG-ProF mice (Cyagen Biosciences) were approved by the MedPacto Inc. IACUC (M-IACUC-2026-0005-01). Through advanced neonatal transplantation of human donor HSCs (HLA-A: A*24:02), this fully humanized model supports multi-lineage reconstitution of human lymphoid (T, B, NK) and myeloid (DCs, monocytes, macrophages, granulocytes) cells.[77,78] Peripheral blood flow cytometry confirmed successful human leukocyte chimerism, with hCD45^{+}/total CD45^{+} ratios ranging from 48.24% to 75.13%. To ensure balanced baseline characteristics, mice were allocated into experimental groups based on both tumor take rate and human immune cell engraftment levels.

Orthotopic 4T-1 tumor model in BALB/c mice

BALB/c mice were orthotopically inoculated with 0.5×10^4 4T-1 murine advanced breast cancer cells into the mammary fat pad. On day 15, the mice were euthanized, and RNA was extracted from the tumor tissues and matched normal tissues using a tissue homogenizer.

Orthotopic CT26 tumor model in BALB/c mice

BALB/c mice were orthotopically inoculated with 5×10^5 CT26 murine colorectal cancer cells into the submucosal region of the cecum. On day 25, the mice were euthanized, and RNA was extracted from the tumor tissues and matched normal tissues using a tissue homogenizer.

Orthotopic B16F10 luc tumor model in C57BL/6J mice

C57BL/6J mice were orthotopically inoculated with 2×10^5 B16F10-Luc murine melanoma cells (UBIGENE, #YC-A011-Luc-P) into the ear skin. On day 22, the mice were euthanized, and RNA was extracted from the tumor tissues and matched normal tissues using a tissue homogenizer.

Orthotopic GL26 tumor model in C57BL/6J mice

For the intracranial implantation of syngeneic tumor cells, C57BL/6J mice were stereotactically inoculated with 1×10^5 GL26 murine glioblastoma cells/6 μL PBS into the right frontal lobe (2 mm lateral and 1 mm anterior to bregma at 2.5-mm depth from the skull base) using a Hamilton syringe (Hamilton Company) and a microinfusion pump. Tumor burden was monitored by luminescence imaging on

day 7 after implantation. On day 24, the mice were euthanized, and RNA was extracted from the tumor tissues and matched normal tissues using a tissue homogenizer.

Orthotopic RM1-Luc tumor model in C57BL/6J mice

C57BL/6J mice were orthotopically inoculated with 0.5×10^5 RM1-Luc murine prostate carcinoma cells into the anterior prostate lobe. On day 22, the mice were euthanized, and RNA was extracted from the tumor tissues and matched normal tissues using a tissue homogenizer.

Orthotopic Hepa1-6 tumor model in C57BL/6J mice

C57BL/6J mice were orthotopically inoculated with 2×10^5 Hepa1-6 murine hepatoma cancer cells into the left liver lobes. On day 20, the mice were euthanized, and RNA was extracted from the tumor tissues and matched normal tissues using a tissue homogenizer.

Establishment of orthotopic 4T-1-luc-LMT-2 tumor model with highly metastatic potential

Orthotopic advanced breast tumor models are more clinically relevant than their subcutaneous counterparts, because of the establishment of an organ-specific tumor. To establish highly metastatic cell lines, we used the continuous implanting method; 4T-1-Luc cells were implanted into the mammary fat pad of a BALB/c mouse. One month later, lung metastatic nodules were collected and digested into single cells. After the process was repeated twice, the metastatic cancer cells, termed 4T-1-Luc-LMT-2 (Highly metastatic cell lines), were separated and then cultured *in vitro*. The 4T-1-Luc-LMT-2 cell line, which mimics the aggressive and immune-resistant characteristics of TNBC, was used to evaluate monotherapy, combination therapy, and bi-specific fusion antibodies targeting TGF-β and PD-1/PD-L1 pathways (control, 25 mg/kg Vactosertib, 20 mg/kg sTβRII, 10 mg/kg anti-PD-1, 20 mg/kg anti-PD-L1, anti-PD-1/Vactosertib, anti-PD-1/sTβRII, anti-PD-L1/sTβRII, 20 mg/kg Bs-anti-PD-1/sTβRII, 20 mg/kg Bs-anti-PD-L1/sTβRII, and 20 mg/kg FEBP-sTβRII). For efficacy and survival studies, 2.5×10^4 4T-1-Luc-LMT-2 cells were inoculated into the mammary fat pad of a BALB/c mouse on day 0. Where appropriate, mice were selected at random. Treatment was initiated on day 6 at 5-day intervals ($n = 5$ mice/group). For immunofluorescence or immunohistochemical studies, mice were treated on day 6 ($n = 6$ mice/group) and euthanized on day 18. Tumor volumes ($0.5 \times \text{length} \times \text{width}^2$) were measured with calipers on the indicated days. After tumor collection, tumors were weighed and samples were used for immunofluorescence or immunohistochemistry. Also, tumor growth and incidence of lung metastasis in the 4T-1-Luc-LMT-2 tumor model were monitored once (early stage) or twice (late stage) weekly on an *in vivo* bioluminescence imager (PerkinElmer, #Lumina S5).

Orthotopic PANC02-Luc pancreatic tumor model

Eight to ten-week-old *wild-type* mice or *Rag1*$^{-/-}$ mice were anesthetized with Zoletil (40 mg/kg) and xylazine (10 mg/kg) via intraperitoneal injection. Hair on the left flank was removed, and the pancreas was carefully taken out using a tissue forceps following a 10-mm mid-axillary line incision just below the rib cage. Then, 3×10^6 cells of PANC02-Luc in 30 μL PBS without Matrigel were injected into the pancreas tail using an insulin syringe with a 29-gauge needle (BD, #320320). On day 7, mice were randomized into treatment groups with comparable average tumor burden based on bioluminescence imaging, and treatment was initiated on the same day and repeated every 5 days. Tumor progression was monitored at the indicated time points using *in vivo* bioluminescence imaging with the IVIS Lumina system (PerkinElmer).

For efficacy and survival studies, cohorts received intravenous control, sTβRII, or FEBP-sTβRII as indicated (30 mg/kg; $n = 8$ per group). Separate cohorts were used for flow cytometric analysis of tumor samples on days 19 and 35 and PWB on day 35, as well as for IFN-γ ELISPOT analysis of lymph node cells on day 19 and *in vitro*-stimulated T-cells on day 50. Additional cohorts were used for IFN-γ neutralization experiments and transcriptomic analyses. For IFN-γ neutralization, anti-IFN-γ antibody was administered on days 11, 14, and 17, with analysis performed on day 18. Tumors were collected on day 35 for bulk RNA-seq ($n = 3$ per group) and scRNA-seq analyses. For scRNA-seq, tumors from four mice per treatment group were pooled before single-cell library preparation.

For the dose-ranging and mechanistic studies, mice ($n = 4$ per group) received vehicle, control, sTβRII (30 mg/kg), or FEBP-sTβRII (15 or 30 mg/kg), starting on day 7 and repeated every 5 days. To explore the potential contribution of TNF-associated inflammatory signaling to the antitumor activity of FEBP-sTβRII, an additional treatment arm received FEBP-sTβRII (30 mg/kg) in combination with soluble TNFR2-Fc (sTNFR2; 20 mg/kg), administered on days 7, 11, and 14. Separately, mutFEBP-sTβRII was evaluated using two intensified sequential treatment schedules: 5 mg/kg for the first two administrations followed by 20 mg/kg for the subsequent six administrations, or 10 mg/kg for the first two administrations followed by 30 mg/kg for the subsequent six administrations, for a total of eight administrations per group. Thus, the mutFEBP-sTβRII cohorts differed from the FEBP-sTβRII dose-ranging cohorts in both dose sequence and number of administrations and were not designed or analyzed as dose-matched comparators. Tumor progression was monitored longitudinally by *in vivo* bioluminescence imaging on days 5, 13, 20, 34, 48, and 62 after tumor implantation.

For immunofluorescence and immunohistochemical analyses, separate cohorts ($n = 6$ per group) were treated beginning on day 12 and euthanized on days 26, 35, or 43, as indicated. Tumors were collected at the respective endpoints for histological analysis.

Orthotopic PKCY-Luc pancreatic tumor model

PKCY-Luc cells (2×10^5 cells in 30 μL with Matrigel) were implanted orthotopically into the pancreas of C57BL/6J mice using the same surgical procedure described for PANC02-Luc implantation. Mice were randomized into treatment groups with comparable

average tumor burden based on bioluminescence imaging and treated on day 7 and repeated every 4 days. Tumor progression was monitored at the indicated time points using *in vivo* bioluminescence imaging with PerkinElmer's IVIS Lumina system.

For efficacy and survival studies, mice received intravenous treatment with control, sTβRII, or FEBP-sTβRII (30 mg/kg; $n = 8$ per group). For PD-1 blockade combination studies, additional cohorts received anti-PD-1 antibody (clone J43; 10 mg/kg) together with control or FEBP-sTβRII (6.5, 15, or 30 mg/kg). Mice were euthanized on day 26 for tumor collection and tumor weight measurement.

For immunofluorescence or immunohistochemical studies, mice were treated using the same dosing schedule and euthanized on day 14 or 20 for tumor collection ($n = 7$ per group).

Orthotopic KPC-Luc pancreatic tumor model

KPC-Luc cells (1.5×10^6 cells in 30 μL with Matrigel) were implanted orthotopically into the pancreas of C57BL/6J mice using the same surgical procedure described for PANC02-Luc and PKCY-Luc implantation. After baseline bioluminescence imaging, KPC-Luc tumor-bearing mice were randomized into control, sTβRII, FEBP-sTβRII, or mutFEBP-sTβRII groups with comparable average tumor burden. Mice received intravenous treatment with the indicated agents (30 mg/kg; $n = 6$ per group), starting on day 7 and repeated every 4 days. Tumor progression was monitored by serial bioluminescence imaging, and mice were followed for survival. Separate KPC-Luc cohorts were used for flow cytometric analysis of tumor samples and PWB on day 15. Additional cohorts were used for anti-IFN-γ experiments and CAF–myeloid co-culture assays on day 18, and for CAF/macrophage–T-cell co-culture assays evaluating antigen-presenting capacity, IFN-γ ELISPOT analysis of lymph node cells, and bulk RNA-seq validation on day 18. Anti-IFN-γ antibody was administered on days 7, 11 and 15. For histology, tumors were collected at day 15–21 and analyzed by α-SMA/CD8 immunofluorescence using tumor edge and inside ROI definitions.

Humanized orthotopic Mia-PaCa2 pancreatic tumor model

HLA-A: A*24:02-compatible $CD34^+$ humanized mice were used for humanized pancreatic tumor studies. Before tumor implantation, peripheral blood was collected and stained for live human $CD45^+$ cells to confirm human immune reconstitution. Mia-PaCa2 cells (3×10^6 cells) were implanted orthotopically into the pancreas under anesthesia. After tumor establishment, mice were randomized into control, sTβRII, or FEBP-sTβRII treatment groups. Treatment was administered on days 7, 11, 15, and 19, and mice were sacrificed on day 21 for tumor weight and histological analysis. $n = 7$ mice per group. Tumors were weighed and processed for α-SMA/CD8 immunofluorescence, H2-Ab1 immunohistochemistry, pan-HLA immunohistochemistry, and *p*-SMAD2/3 immunohistochemistry.

Cell lines

HEK293T cells (CRL-3216, Female), Mia-PaCa2 (CRL-1420, Male), 4T-1 (CRL-2539-LUC2, Female) murine breast cancer, CT26 (CRL-2638, Female) murine colorectal cancer, B16F10 (CRL-6475, Male) murine melanoma, RM1 (CRL-3310, Male) murine prostate cancer, and Lewis lung carcinoma (LLC, CRL-1642, Male) murine lung cancer cell lines were obtained from the American Type Culture Collection (ATCC; Manassas, VA, USA). MB49 murine bladder cancer (Male) and B16-OVA MO4 (Male, murine melanoma expressing chicken-ovalbumin, SCC420) were purchased from Sigma-Aldrich (St. Louis, MO, USA). PANC02-OVA-Luc (VOA4B040) cell line was purchased from Vitro Biotech (Kowloon, Hong Kong). Luciferase-expressing KPC cell line (KPC-Luc), derived from KPC mice (*C57BL/6N.129Cya-Kras*$^{tm1(LSL\text{-}G12D)}$*Trp53*$^{tm1(LSL\text{-}R172H)}$*Tg(Pdx1-Cre)/Cya,* C001308), was custom-synthesized by Cyagen (Suzhou, China). Hepa1-6 (CRL-1830) murine liver cancer was purchased from Professor Sachiyo Nomura through her collaborator Dr. James R. Goldenring of Vanderbilt University School of Medicine, TN. GL26 murine glioblastoma cell line was provided by Dr. John S. Yu (Cedars Sinai Medical Center, Los Angeles, CA), PANC02 murine pancreatic cancer cell line (Male) was provided by Professor Kyu Lim (Chungnam National University, Republic of Korea). Murine PDAC cell lines (PKCY cells) derived from a genetically engineered PKCY mouse (*Pdx1-cre*;*LSL-K-Ras*$^{G12D/+}$;*TP53*$^{fl/+}$;*R26*^{YFP} mouse) were provided by Dr. Andrew D. Rhim (University of Texas, MD Anderson Cancer Center). 4T-1, PANC02, CT26, Hepa1-6, B16F10, PKCY, MiaPaCa-2, and GL26 cells were cultured in 5% CO_2 at 37°C and maintained in Dulbecco's modified Eagle medium (DMEM) supplemented with 10% heat-inactivated FBS, 2 mM L-glutamine, 100 U/mL penicillin-streptomycin. HEK293T and RM1 cells were cultured in R10 medium (RPMI1640 supplemented with 10% heat-inactivated FBS). 4T-1, PANC02, CT26, B16F10, PKCY-Luc, GL26, RM1, and Hepa1-6 cells were passaged 2 to 21 times before *in vivo* implantation and harvested with TrypLE Express (Gibco) or 0.25% trypsin. Before experiments, trypan blue exclusion staining was used to determine the number of viable cells.

METHOD DETAILS

FEBP-sTβRII computer-generated model

FEBP-sTβRII structural predictions were performed using AlphaFold3,[71] and final models were visualized in UCSF ChimeraX (v1.7.1).[70] The model shows the crystal structure of an Fcγ4 (PDB ID: 4D2N) (Davies, A.M.) linked by a computer-generated (Molecular Operating Environment [MOE]) $(G_4S)_4G$ linker to the extracellular domain of TβRII (sTβRII); both of the sTβRII moieties can simultaneously bind a disulfide-linked TGF-β homodimer (PDB ID: 1KTZ). [Fc-sTβRII as a systemic TGF-β trap] is a structure in which TβRII ectodomain is fused to the C terminus of the heavy chain Fc region, [FEBP-Fc-sTβRII] is a general dual target fusion system, in which a fibronectin EDB binding peptide (FEBP) polypeptide is fused to the N-terminal of Fc region, and a TβRII ectodomain is fused to the

C-terminal of Fc region, [Fc-FEBP-sTβRII] is a form in which the dual N-terminal FEBP polypeptides with TβRII ectodomain is fused to the C-terminal of the FEBP polypeptide linked below Fc region, and [Fc-sTβRII-FEBP] is a structure in which the FEBP polypeptide is fused to the C-terminal of the TβRII ectodomain linked below Fc region. [sTβRII-Fc and sTβRII-FEBP-Fc] were designed as Fc-fusion formats in which the sTβRII moiety alone, or the sTβRII-FEBP module, respectively, is positioned at the N-terminus relative to the Fc region. [FEBP-Fc-FEBP-sTβRII, FEBP-Fc-sTβRII-FEBP, and Fc-FEBP-sTβRII-FEBP] are engineered dual-target fusion proteins in which two FEBP polypeptides are positioned in different orientations within the Fc-sTβRII (sTβRII) backbone, thereby enabling multivalent FN-EDB recognition while preserving TGF-β trapping capacity. [2FEBP-Fc-sTβRII, Fc-2FEBP-sTβRII, and Fc-sTβRII-2FEBP] were designed to compare EDB-binding affinity and positional effects through a tandem FEBP arrangement strategy, while the sTβRII or mutFEBP-sTβRII version serves as a negative control.

1) Structural prediction of Fc-soluble TβRII and FEBP-sTβRII formats

The amino acid sequences of Fc-soluble TβRII and the nine FEBP-sTβRII formats were used as dimeric inputs for structural modeling with AlphaFold3. This configuration allowed for the prediction of potential inter-domain interactions critical to fusion protein stability. For each construct, five independent predictions were generated to ensure reproducibility. The final models were selected based on high ipTM (interface predicted TM-score) and pTM (predicted TM-score) values, which quantitatively reflect the reliability of inter-domain interfaces and the overall accuracy of the structural models. These models were subsequently visualized and analyzed using UCSF ChimeraX (v1.7.1) to evaluate domain organization, relative orientation, and overall structural integrity.

2) FN-EDB binding analysis for FEBP-sTβRII formats

To evaluate FN-EDB binding interactions, a second round of AlphaFold3 predictions was performed, incorporating the FN-EDB sequence alongside the FEBP-sTβRII formats in the same dimeric configuration. Models were ranked based on ipTM and pTM scores, and Predicted Aligned Error (PAE) plots were extracted to assess the spatial accuracy of FN-EDB and fibronectin EDB-binding peptide (FEBP) interactions. Lower PAE values (darker regions) indicate higher confidence in the predicted binding interface. The x- and y axes of the PAE plots were annotated to correspond to FN-EDB (yellow) and FEBP (red) regions, respectively.

Cloning of FEBP-sTβRII formats, sTβRII and antibody fusion formats

DNA fragments for control-Fc (mouse IgG1, mouse IgG2a, human IgG4, human IgG1), control-IgG types, sTβRII/FEBP-sTβRII formats, anti-PD-1 (J43) antibody, anti-PD-L1 (Avelumab) antibody, and FN-EDB-Fc were synthesized by Bionics. To reduce immunogenicity in preclinical animal studies, mouse IgG2a D265A/N297A (DANA) and human IgG1 N297A variant constant regions were used. Additionally, to prevent Fab arm exchange in human IgG4, Serine 228 in the hinge region was substituted with Proline. The DNA fragments FEBP-sTβRII and mutFEBP-sTβRII included constant regions from mouse IgG1 or human IgG4 (S228P), fused with FEBP (also known as APT^{EDB}) and the TβRII ectodomain. Anti-PD-1 and anti-PD-L1 antibody protein fusion formats were generated through overlapping PCR using DNA fragments encoding mouse IgG1 or IgG2a (DANA) and human IgG1 (N297A) or IgG4 (S228P) constant regions. Additionally, a DNA fragment encoding the human TβRII ectodomain was synthesized and fused to the corresponding IgG constant regions. For FN-EDB target-binding ELISA, a DNA fragment encoding the fibronectin EDB domain was fused to the IgG1 constant region to generate FN-EDB-Fc fusion protein.

Expression and purification of FEBP-sTβRII formats, sTβRII and antibody fusion formats

Plasmids encoding control-Fc molecules (mouse IgG1, mouse IgG2a, rabbit IgG1, human IgG4, and human IgG1), FEBP-Fc-sTβRII, Fc-FEBP-sTβRII, Fc-sTβRII-FEBP, sTβRII-FEBP-Fc, FEBP-Fc-FEBP-sTβRII, FEBP-Fc-sTβRII-FEBP, Fc-FEBP-sTβRII-FEBP, 2FEBP-Fc-sTβRII, Fc-2FEBP-sTβRII, Fc-sTβRII-2FEBP, FEBP-sTβRII, mutFEBP-sTβRII (lacking FN-EDB binding ability), sTβRII-Fc, sTβRII (Fc-sTβRII), anti-PD-1 (J43), Bs-anti-PD-1/sTβRII, anti-PD-L1 (avelumab), Bs-anti-PD-L1/sTβRII, and FN-EDB-Fc were transiently transfected into CHO-S cells using the ExpiCHO Expression System Kit (Thermo Fisher Scientific, #A29133) according to the manufacturer's protocol. In parallel, additional format variants, including Control-Fc, sTβRII, FEBP-Fc-sTβRII, Fc-FEBP-sTβRII, Fc-sTβRII-FEBP, and mutFEBP-sTβRII, were transiently produced using the Expi293 Pro Expression System Kit (Thermo Fisher Scientific, #A14635) according to the manufacturer's protocol and purified using the same downstream workflow as CHO-S-derived proteins. Culture supernatants were harvested 8–10 days after transfection for CHO-S cultures and 4–6 days after transfection for Expi293 cultures. Supernatants were clarified by low-speed centrifugation and filtered through 0.45-μm filters. Clarified supernatants were supplemented with 10× binding buffer (0.2 M Na_3PO_4, pH 7.0) and loaded onto Protein A prepacked gravity-flow columns (Cytiva, #28-9852-54). Bound proteins were eluted with 0.1M glycine-HCl (pH 2.7) into a neutralizing buffer (1M Tris-HCl, pH 9.0), concentrated by centrifugation, and buffer-exchanged into PBS (pH 7.4). The purified proteins were quantified using spectrophotometry, and purity was assessed by SDS-PAGE followed by Coomassie blue staining. To evaluate physicochemical homogeneity, size exclusion chromatography (SEC) was performed using an AKTA purifier system (Cytiva) equipped with a Superdex S200 10/300 GL column (Cytiva, #28-9909-44) and PBS as the mobile phase at a flow rate of 0.5 mL/min. The percentage of monomeric species was calculated as the area under the monomeric peak divided by the total area of monomeric and non-monomeric peaks at 280 nm. All purified formats were filtered through 0.22-μm filters and validated for low endotoxin levels using the Endosafe LAL cartridge system (Charles River Endosafe MS, #PTS55005F) before being used in experiments. In addition, a subset of the Fc-FEBP-sTβRII material used in this study was produced from a research cell bank (RCB)-derived CHO-K1 production batch manufactured at Chime

Biologics, and material from this independent batch was incorporated into efficacy studies in the PANC02-OVA, B16-OVA, and KPC tumor models.

Cell isolation from tumors for flow cytometry

Tumor tissues and peripheral whole-blood (PWB) samples were collected from mice bearing PANC02-Luc or KPC-Luc tumors following the indicated treatments. Tumor tissues alone were collected from mice bearing PANC02-OVA or B16-OVA tumors. For tumor cell analysis, tumor tissues were excised and cut into the smallest possible fragments by using ophthalmic scissors. The tumor fragments were incubated for 30 min at 37°C in RPMI medium containing 1 mg/mL collagenase type I (Worthington), 50 U/mL DNase I (Enzynomics) and 2% FBS with constant shaking. After incubation, the digestion reaction was stopped by adding cold FACS buffer (2% FBS, 1mM EDTA in PBS), and the fragments were filtered through a 100-μm nylon mesh cell strainer (BD Falcon). Red blood cells were lysed in ammonium-chloride-potassium (ACK) buffer (150 mM ammonium chloride, 10 mM potassium chloride, 0.1 mM sodium EDTA, pH 7.4), followed by filtering through a 40-μm cell strainer (BD Falcon).

CRISPR/Cas9-mediated deletion of the Fn1-EDB in murine KP-PSAFs

For generation of *Fn1-EDB* knockout cells (*KP*-PSAFs-ΔEDB) by CRISPR/Cas9-mediated gene targeting, we targeted the upstream and downstream intronic regions of exon 25 of *Fn1* (RefSeq Accession number: NM_010233.2): 5′-GGACGTCTTTTCAGATAATT-3' (front intron of exon 25, FI-E25) and 5′-AGTCTTCTGTGTTTGAGACATGG-3' (behind intron of exon 25, BI-E25) using GeneArt Precision gRNA Synthesis Kit (Invitrogen) according to the manufacturer's protocol. *KP*-PSAFs at passage 2–4 were transfected with the gRNAs and Cas9 protein (Toolgen) using the Neon Transfection System following the manufacturer's protocol. These primary cancer-associated fibroblastic cells generally show senescence over the course of serial passaging; thus, cells with fewer than 10 passages were used in all experiments. Since *KP*-PSAFs were unable to form colonies from individual cells, the pools of edited cells were used for further FEBP-sTβRII binding assays, protein and mRNA isolation. Genomic DNA from *KP*-PSAFs was extracted, and the region encompassing exon 25 of the *Fn1-EDB* gene was amplified using primers targeting the flanking intronic sequences of exon 25 with AccuPower PCR Premix (Bioneer). The CRISPR/Cas9-mediated *Fn1-EDB* gene knockout efficiency in *KP*-PSAFs was determined by ICE knockout analysis (www.synthego.com) using the PCR products. *Fn1-EDB*-depleted *KP*-PSAFs with ICE and KO scores exceeding 70%, indicating a high percentage of indels and frameshift mutations, were selected for further experiments.

Flow cytometry

For staining of cell surface markers, cell suspensions were blocked with anti-Mouse CD16/32 (BioLegend, #101301). Live/dead cell discrimination was performed using Viability Dye (BioGems, #62910-00-100, #62510-00-100), followed by the surface antibody cocktail for 30 min in the dark at 4°C. For phosphorylated STAT5 staining, cells were serum-starved for 45 min at 37°C and subsequently stimulated with IL-2 (100 U/mL) for 30 min at 37°C. For Foxp3 and phosphorylated STAT5 staining, cell suspensions were stained for the cell surface marker as described above, and then fixed and stained using BD Pharmingen Transcription Factor Buffer Set (BD Biosciences, #562725) or eBioscience Foxp3/Transcription Factor Staining Buffer Set (Thermo Fisher Scientific, #00-5523-00) according to the manufacturer's instructions. For intracellular cytokine staining, single cells were re-suspended in complete RPMI with 25 ng/mL Phorbol 12-myristate 12-acetate (PMA, Sigma-Aldrich, #P1585), 1 μg/mL ionomycin (Sigma-Aldrich, #10634) and BD GolgiStop (BD Biosciences, #554724). The suspensions were incubated for 4 h at 37°C. At the end of the stimulation, cells were stained for surface antigens as described above, followed by intracellular staining for cytokines using the eBioscience Intracellular Fixation & Permeabilization Buffer Set (Thermo Fisher Scientific, #88-8824-00) according to the manufacturer's instructions. CAF- and immune-profile mapping was performed by flow cytometry (Figures S8B and S8C). To evaluate the inhibition of FN-EDB-dependent TGF-β-induced signaling by FEBP-sTβRII, 4T-1-Luc-LMT-2 cells with low FN-EDB expression were seeded on Matrigel-coated plates either unmodified or further coated with sarcoma-derived *KP*-PSAFs, which exhibit high FN-EDB expression. Cells were pre-treated with control, sTβRII, FEBP-sTβRII, or mutFEBP-sTβRII (300 ng/mL) for 1 hour to permit simultaneous binding to matrix-anchored FN-EDB, followed by three washes with PBS and subsequent stimulation with TGF-β1 (5 ng/mL, PeproTech, #100-21C) for 1 hour. Following treatment, cells were fixed, permeabilized, and stained with an antibody recognizing phospho-SMAD2 (Ser465/467)/SMAD3 (Ser423/425), and phospho-SMAD2/3 levels were quantified by flow cytometry. Samples were measured with BD Canto II using BD FACSDiva 8.0.2 software (BD Biosciences) or CytoFLEX (Beckman) using CytExpert 2.0 software and data subsequently analyzed with FlowJo 10.8.1 software (TreeStar). All antibodies used in this study are listed in key resources table.

Adoptive cell transfer in the *Rag1*$^{-/-}$ mice bearing PKCY tumor treated with *FEBP-sTβRII*

When orthotopic PKCY-Luc tumors in *Rag1*$^{-/-}$ mice reached the treatment stage, mice were administered control or FEBP-sTβRII every 4 days for a total of four doses. A subset of FEBP-sTβRII-treated mice additionally received adoptive transfer of CD45.1^{+}CD3^{+} T-cells. CD45.1^{+} congenic mice were used as T cell donors to distinguish donor from host lymphocytes. Spleens were harvested from 8 to 10-week-old CD45.1^{+} mice, and CD3^{+} T-cells were isolated using the CD3ε MicroBead Kit (Miltenyi Biotec, #130-094-973) and LS columns (Miltenyi Biotec, #130-042-401) according to the manufacturer's instructions. The purity and phenotype of the isolated T-cells were verified by flow cytometry. Purified CD3^{+} T-cells (4.5×10^{6} cells per mouse) were injected intravenously on days 8, 12, and 16 after tumor inoculation. Recombinant IL-2 (10,000 IU per mouse, CLINIGEN, #076100031R) was administered intraperitoneally once daily for three consecutive days following each T cell transfer to support T cell activation and persistence.

B16-OVA-luc tumor model

C57BL/6 mice were subcutaneously inoculated with B16-OVA cells (1×10^6 cells) on day 0 and intravenously treated with control (30 mg/kg), sTβRII (30 mg/kg), mutFEBP-sTβRII (30 mg/kg), or FEBP-sTβRII (30 mg/kg) on days 8, 11, and 14. Anti-IFN-γ antibody was administered on days 6, 9, and 12. Mice were euthanized on day 16, and tumors and spleen were harvested for subsequent flow cytometric and functional co-culture analyses.

PANC02-OVA-luc tumor model

C57BL/6 mice were orthotopically inoculated with PANC02-OVA cells (2×10^6 cells) on day 0 and intravenously treated with control (30 mg/kg) or FEBP-sTβRII (30 mg/kg) on day 26 and every 5 days thereafter. Anti-IFN-γ antibody was administered on days 24, 27, and 30. Mice were euthanized on day 35, and tumors were harvested for subsequent flow cytometry analyses.

Survival analysis

Mice bearing 4T-1-Luc-LMT-2 orthotopic tumors were randomized into 11 treatment groups: control ($n = 6$); Vactosertib (25 mg/kg, $n = 6$); sTβRII (20 mg/kg, $n = 6$); anti-PD-1 (10 mg/kg, $n = 6$); anti-PD-L1 (20 mg/kg, $n = 6$); anti-PD-1/Vactosertib ($n = 5$); anti-PD-1/sTβRII ($n = 5$); anti-PD-L1/sTβRII ($n = 5$); Bs-anti-PD-1/sTβRII (20 mg/kg, $n = 6$); Bs-anti-PD-L1/sTβRII (20 mg/kg, $n = 6$); and FEBP-sTβRII (20 mg/kg, $n = 5$). For the PANC02-Luc orthotopic model, mice were randomized into five groups: control ($n = 8$), sTβRII (30 mg/kg, $n = 8$), FEBP-sTβRII (30 mg/kg, $n = 8$), anti-PD-1 (10 mg/kg, $n = 4$), and anti-PD-1/sTβRII ($n = 4$). For the KPC-Luc orthotopic model, mice were randomized into four groups: control ($n = 16$), sTβRII (30 mg/kg, $n = 13$), FEBP-sTβRII (30 mg/kg, $n = 20$), and mutFEBP-sTβRII (30 mg/kg, $n = 9$). Two independent cohorts of mice bearing orthotopic PKCY-Luc tumors were similarly randomized into control, sTβRII, and FEBP-sTβRII treatment groups ($n = 8$ per group). Treatments were administered subcutaneously initiating on day 5 for the 4T-1-Luc-LMT-2 model or intravenously initiating on day 7 for the PANC02-Luc (5-day intervals), KPC-Luc (4-day intervals) and PKCY-Luc (4-day intervals) models, and then discontinued (“Stop to treat”). Tumor progression was monitored by serial bioluminescence imaging, and mice were euthanized upon reaching humane endpoints. Long-term survivors were defined as animals with no detectable luminescence for at least 90 consecutive days. Overall survival was analyzed using Kaplan-Meier curves, and statistical significance was determined by the log-rank (Mantel-Cox) test, with Holm–Šidák adjustment for multiple prespecified pairwise comparisons where applicable.

Tumor rechallenge studies

Long-term functional immunity was evaluated by subcutaneous tumor rechallenge of FEBP-sTβRII-cured mice derived from the PANC02-Luc and PKCY-Luc orthotopic PDAC models. “Cured” denoted complete regression of the primary orthotopic tumor with no detectable disease for ≥90–100 days after the final treatment. For each rechallenge cohort, age-matched or -unmatched naive C57BL/6 mice served as controls. To exclude any confounding immunogenicity from luciferase, all rechallenge inoculations used the parent (luciferase-negative) cell lines. No additional therapy was administered after rechallenge. All procedures were approved by the institutional IACUC. In both models, mice that achieved complete regression after FEBP-sTβRII were rechallenged to evaluate tumor growth in the absence of further treatment. Syngeneic cell lines included PANC02, PKCY, MB49 (bladder carcinoma), and LLC (Lewis lung carcinoma). Cells were resuspended in PBS and injected subcutaneously into the shaved flank under brief isoflurane anesthesia using 29-gauge needles. PDAC lines and MB49 were implanted at 1×10^6 cells in 100 μL, whereas LLC were implanted at 2×10^6 cells in 100 μL. Each mouse received a single tumor type at rechallenge (no bilateral co-implantation). For PANC02-Luc survivors, durability of protection was tested by same-tumor rechallenge at day 122 or day 611 after therapy ($n = 6$ per time point), with age-matched naive controls ($n = 5$) receiving identical PANC02 inoculation. Breadth of protection was assessed in an independent cohort of day-611 PANC02 survivors rechallenged with PKCY ($n = 6$), MB49 ($n = 6$), or LLC ($n = 5$), each with matched naive controls ($n = 5$ per tumor). For PKCY-Luc survivors, durability of protection and reciprocity were tested by rechallenge at day 102 with PKCY, MB49, or LLC ($n = 5$–6 per arm; naive $n = 5$ each), and in a second cohort at day 141 with PANC02 ($n = 10$; naive $n = 5$). Tumor dimensions (length, width) were measured twice weekly with calipers, and volumes were calculated as $(length \times width^2)/2$. Individual growth trajectories are reported for all rechallenge arms. Mice were monitored at least three times weekly for health and euthanized at prespecified humane endpoints (tumor volume ≥2,000 mm^3, ulceration, >20% body-weight loss, or signs of distress). Survival was analyzed from the date of rechallenge using Kaplan-Meier curves and compared by log-rank (Mantel-Cox) tests (two-sided). Where indicated, group differences in tumor volume were assessed by two-way ANOVA with Šidák’s correction.

Memory-phase immune depletion

Lineage-depletion studies were initiated in PKCY-Luc CR mice 127 days after cessation of FEBP-sTβRII treatment. CR mice were subcutaneously rechallenged with PKCY ($n = 3$–5), PANC02 ($n = 4$–5), MB49 ($n = 4$–5), or LLC ($n = 4$–5) cells, with matched naive controls included for each tumor model ($n = 5$ per group), in the absence of further FEBP-sTβRII treatment. For $CD8^+$ or $CD4^+$ T cell depletion, mice received intraperitoneal injections of purified anti-CD8α antibody (Bio X Cell, 53-6.7 clone, #BE0004-1) or anti-CD4 antibody (Bio X Cell, YTS191 clone, #BE0119), respectively, at 200 μg per mouse. Antibody administration was initiated 2 days before tumor-cell inoculation and repeated on days 3, 6, 9, and 12 after inoculation. Control mice received anti-Rat IgG antibody (Bio X Cell, #BE0094) according to the same schedule. For NK-cell depletion, mice received an intraperitoneal injection of purified anti-NK1.1 antibody (Bio X Cell, PK136 clone, #BE0036) at 0.5 mg per mouse 2 days and 1 day before tumor-cell inoculation,

followed by additional injections at 0.25 mg per mouse on days 6, 9, and 12 after inoculation. Depletion of $CD8^+$ T-cells, $CD4^+$ T-cells, and NK-cells was confirmed by flow cytometric analysis of peripheral blood collected by retro-orbital bleeding 3 days after the final antibody injection.

Adoptive transfer of memory T-cells

C57BL/6J mice were subcutaneously inoculated with MB49 or LLC tumor cells. Spleens were harvested from PKCY CR mice or matched naive mice, and $CD8^+$ and $CD4^+$ T-cells were isolated using $CD8^+$ MicroBeads (Miltenyi Biotec, #130-116-478) or $CD4^+$ MicroBeads (Miltenyi Biotec, #130-116-475), respectively, in combination with LS Columns (Miltenyi Biotec, #130-042-401), according to the manufacturer's instructions. The purity and phenotype of the isolated T-cells were verified by flow cytometry. Recipient mice received an intraperitoneal injection of cyclophosphamide (CTX; 100 mg/kg, Sigma-Aldrich, #C7397) 1 day before the first T cell transfer. Purified $CD8^+$ or $CD4^+$ T-cells from PKCY CR mice or matched naive mice were intravenously administered at 2×10^6 cells per mouse on days 5 and 8 after tumor inoculation. For the combined-transfer group, $CD4^+$ and $CD8^+$ T-cells were each administered at 2×10^6 cells per mouse. Recombinant IL-2 (10,000 IU per mouse, CLINIGEN, #076100031R) was administered intraperitoneally once daily for 3 consecutive days following each T cell transfer.

Cancer-associated fibroblasts (CAFs)-like cell isolation

Aggressive sarcomas were harvested from spontaneous $KRas^{LA1}/TP53^{-/-}$ (*KP*) male mice (12 weeks old). The tumors were minced and digested in 1 mg/mL collagenase type I (Worthington, # CLS-1), 50 U/mL DNase I (Enzynomics, #M059S) and 2% FBS at 37°C with vigorous shaking for 30 min. Following digestion, tissues were further homogenized through a 100 μm cell strainer and pelleted by centrifugation at 500 x *g*. Red blood cells were lysed in ammonium-chloride-potassium (ACK) buffer (150 mM ammonium chloride, 10 mM potassium chloride, 0.1 mM sodium EDTA, pH 7.4) and resuspended in magnetic-activated cell sorting (MACS) buffer (0.5% BSA and 2 mM EDTA in PBS). $CD45^+$ cells were depleted using anti-CD45 microbeads (Miltenyi Biotec #130-052-301) and subsequently cultured in primary culture. To isolate CAFs from the acquired $CD45^-$ primary cultured cells, the mouse tumor-associated fibroblast isolation kit (Miltenyi Biotec #130-116-474) was used in a two-step strategy according to the manufacturer's protocol. Briefly, samples were first pre-enriched by removing non-target cells, followed by isolation using the marker CD90.2. For pre-enrichment, LD Columns on a MidiMACS Separator (Miltenyi Biotec, #130-090-329) were used and for the subsequent CAF-like cell isolation, MS Columns on a MiniMACS Separator (Miltenyi Biotec, #130-090-312) were used. Isolated CAFs were cultured in α-MEM medium supplemented with 10% FBS, β-mercaptoethanol and 100 U/mL penicillin-streptomycin. Murine *KP* primary sarcoma-associated fibroblast-like cells (*KP*-PSAFs) were isolated from aggressive sarcomas of spontaneous *KP* mice (Figure S8A).

Peripheral blood human CD45 analysis in humanized mice

Peripheral whole blood was collected from $CD34^+$ huHSC-NKG-ProF humanized mice (Cyagen Biosciences Inc. China) before orthotopic Mia-PaCa2 implantation and/or before treatment. Red blood cells were lysed, and leukocytes were stained with viability dye and anti-Human CD45 and anti-Mouse CD45 antibodies. Live human $CD45^+$ cell frequency was quantified by flow cytometry. Humanized mice with comparable human $CD45^+$ reconstitution were randomized into treatment groups.

TCF1/CD127/Ki67 recall analysis

Lymph nodes and peripheral blood were collected from age-matched naive mice, tumor-free complete responder mice, age-matched tumor-bearing mice, and complete responder mice after tumor rechallenge. $TCF1^+CD127^+$, $TCF1^+Ki67^+$, and $TCF1^-Ki67^+$ populations were quantified within $CD4^+$ and $CD8^+$ T cell gates. All antibodies used in this study are listed in the key resources table.

Evaluation of the antigen-presenting capacity of CAFs and macrophages

Total CAFs ($CD45^-EpCAM^-CD31^-PDPN^+$), MHC-$II^+$ CAFs ($CD45^-EpCAM^-CD31^-PDPN^+MHC\text{-}II^+$), and TAMs ($CD45^+CD11b^+F4/80^+$) were isolated from KPC or B16-OVA tumors using a FACSAria Fusion cell sorter (BD Biosciences, #656700). Sorted CAFs and macrophages were seeded in 96-well plates at 2×10^3 cells per well for OT-I co-culture experiments or 1×10^4 cells per well for OT-II co-culture experiments in RPMI-1640 medium supplemented with 10% FBS.

For antigen loading, sorted CAFs and macrophages were incubated for 1 h with OVA 257–264 peptide (1 μg/mL) or OVA 323–339 peptide (2 μg/mL). Following Ag loading, cells were washed to remove unbound peptides before co-culture with OT-I $CD8^+$ T-cells or OT-II $CD4^+$ T-cells, respectively.

OT-I $CD8^+$ T-cells and OT-II $CD4^+$ T-cells were isolated from the spleens of 8–10-week-old OT-I and OT-II transgenic mice, respectively. Following red blood cell lysis using ACK lysis buffer, OT-I $CD8^+$ T-cells were purified using $CD8^+$ MicroBeads (Miltenyi Biotec, #130-116-478), whereas OT-II $CD4^+$ T-cells were purified using $CD4^+$ MicroBeads (Miltenyi Biotec, #130-116-475), according to the manufacturer's instructions.

Purified OT-I $CD8^+$ T-cells or OT-II $CD4^+$ T-cells were added at 5×10^4 cells per well to peptide-pulsed CAFs or macrophages and co-cultured overnight in complete RPMI-1640 medium supplemented with 10% FBS, 1× antibiotic-antimycotic solution, 1% sodium pyruvate, 1% non-essential amino acids, and 55 μM β-mercaptoethanol. BD GolgiStop Protein Transport Inhibitor was added during the final 4 h of co-culture to facilitate intracellular cytokine accumulation. Cells were then harvested and analyzed by flow cytometry for the expression of CD69 and intracellular IFN-γ.

Preparation of splenic dendritic cells and bone marrow-derived dendritic cells

For the isolation of splenic dendritic cells (DCs), splenocytes were prepared by mechanical dissociation of spleen tissues, followed by red blood cell lysis. Splenocytes were washed and resuspended in magnetic separation buffer. $CD11c^+$ DCs were isolated using CD11c MicroBeads UltraPure, mouse (Miltenyi Biotec, #130-125-835), according to the manufacturer's instructions. Briefly, splenocytes were incubated with anti-CD11c magnetic microbeads and subjected to magnetic separation using a MACS separation system. Positively selected $CD11c^+$ cells were collected, washed, and used for subsequent experiments.

For the generation of bone marrow-derived dendritic cells (BMDCs), bone marrow cells were isolated from the femurs and tibiae by flushing the marrow cavities with culture medium, followed by red blood cell lysis. Bone marrow cells were cultured in complete RPMI-1640 medium supplemented with recombinant murine GM-CSF (20 ng/mL; R&D Systems, #415-ML) and recombinant murine IL-4 (10 ng/mL; PeproTech, #214-14). Cells were cultured for 7 days, with half of the culture medium replaced every 2 days with fresh cytokine-containing medium. At the end of the differentiation period, non-adherent and loosely adherent cells were collected and used as BMDCs.

In vitro stimulation of antigen-specific T-cells

To expand antigen-specific T-cells *in vitro*, splenocytes were seeded at 5×10^6 cells per well in 12-well plates and cultured in RPMI-1640 medium supplemented with 10% FBS, 50 μM β-mercaptoethanol, 10 mM HEPES, 1% antibiotic-antimycotic solution, and non-essential amino acids.

For the B16-OVA model, splenocytes were stimulated with either OVA 257–264 peptide (1 μg/mL; Sigma-Aldrich, #S7951) or OVA 323–339 peptide (2 μg/mL; Sigma-Aldrich, #O1641) in the presence of recombinant murine IL-7 (20 ng/mL; PeproTech, #AF-200-07). After 3 days of culture, the medium was replaced with fresh medium containing IL-7 (20 ng/mL) and IL-2 (20 U/mL; CLINIGEN, #076100031), and the cells were cultured for an additional 2 days. On day 5, expanded *in vitro*-stimulated (IVS) T-cells were harvested and used for mouse IFN-γ ELISPOT assays.

For the PANC02-Luc model, splenocytes isolated from PANC02-Luc tumor-bearing mice were co-cultured with splenic DCs pulsed with PANC02-Luc tumor cell lysate (100 μg/mL). Cells were cultured in the presence of recombinant IL-7 (20 ng/mL) and recombinant murine IL-15 (10 ng/mL; PeproTech, #210-15). After 3 days of culture, the medium was replaced with fresh medium containing IL-7 (20 ng/mL) and IL-2 (20 U/mL), and the cells were cultured for an additional 2 days. Expanded IVS T-cells were harvested on day 5 and used for mouse IFN-γ ELISPOT assays.

Measurement of IFN-γ secretion by ELISPOT assay

Antigen-specific T cell responses were evaluated using a mouse IFN-γ ELISPOT assay. Depending on the experiment, either the Mabtech Mouse IFN-γ ELISPOT kit (#3321-2H) or the R&D Systems Mouse IFN-γ ELISPOT kit (#XEL485) was used according to the manufacturer's instructions. Briefly, 96-well PVDF plates were prepared with anti-Mouse IFN-γ capture antibody and blocked with RPMI-1640 medium containing 10% FBS for 30 min at room temperature. For ELISPOT restimulation, DCs were cultured in complete RPMI-1640 medium and stimulated overnight with lipopolysaccharide (LPS; 100 ng/mL; Sigma-Aldrich, #L2630) in the presence of the indicated antigen. For the B16-OVA model, DCs were loaded with either OVA 257–264 peptide (1 μg/mL) or OVA 323–339 peptide (2 μg/mL). For the PANC02-Luc and KPC-Luc models, DCs were loaded with the indicated tumor cell lysate (100 μg/mL). IVS cells or draining lymph node cells were co-cultured overnight with antigen-loaded DCs or no-antigen control DCs at an effector cell-to-DC ratio of 5:1 at 37°C in a humidified CO_2 incubator. After incubation, the plates were washed and incubated with biotinylated anti-Mouse IFN-γ detection antibody for 2 h at room temperature. Following washing, the plates were incubated with streptavidin-HRP for 1 h at room temperature. Spots were developed using the substrate provided with each kit, rinsed with distilled water, and air-dried. Spot-forming units (SFUs) were enumerated using an automated ELISPOT reader (ImmunoSpot S5UV; Cellular Technology Limited).

Preparation of bone marrow-derived macrophages (BMDMs)

Bone marrow cells were isolated from the femurs and tibiae by flushing the marrow cavities with culture medium. Erythrocytes were removed using ACK lysis buffer. Cells were cultured at a density of 3.5×10^6 cells/mL in DMEM supplemented with 10% FBS, 100 U/mL penicillin, 100 μg/mL streptomycin, and recombinant murine M-CSF (20 ng/mL; PeproTech, #315-02). After 5 days of culture, fresh M-CSF-containing medium was added, and the cells were cultured for an additional 2 days. On day 7, non-adherent cells were removed by washing with PBS, and adherent BMDMs were gently detached using a cell scraper and harvested for subsequent co-culture experiments.

CAF and macrophage mono- and co-culture assays

For CAF–macrophage co-culture assays, total CAFs ($CD45^-EpCAM^-CD31^-PDPN^+$) and total TAMs ($CD45^+CD11b^+F4/80^+$) were isolated from KPC tumors using a FACSAria Fusion cell sorter. CAFs were co-cultured with either BMDMs or TAMs at a 1:1 ratio and treated for 24 h with recombinant murine IFN-γ (10 ng/mL; PeproTech, #315-05), FEBP-sTβRII (10 μg/mL), and/or recombinant murine TGF-β1 (5 ng/mL; PeproTech), as indicated. Following treatment, cells were harvested and analyzed by flow cytometry to assess phenotypic changes in CAFs and macrophages.

Flow cytometry-based assay to assess binding of FEBP-sTβRII to FN-EDB *in vitro*

For the binding of FEBP-sTβRII to FN-EDB *in vitro*, one million cells were stained with Viability Dye 780 (BioGems) to exclude dead cells, followed by intracellular staining with FEBP-sTβRII, mutFEBP-sTβRII, sTβRII, and control, each prepared at a 1:100 dilution or with serial dilutions. In the case of *KP*-PSAF-wild-type and ΔEDB (*Fn1-EDB* KO) cells, intracellular staining was performed using the eBioscience Intracellular Fixation & Permeabilization Buffer Set (Thermo Fisher Scientific) in the dark at room temperature for 30 min. After staining, cells were washed, resuspended, and incubated with Ax647-conjugated goat anti-Human IgG (Thermo Fisher Scientific, #A21445) in the dark at room temperature for 30 min. Following incubation, cells were washed again and analyzed by flow cytometry.

Measurement of FEBP-sTβRII binding by ELISA

To determine whether FEBP-sTβRII formats bind to plate-bound TGF-β1, 96-well plates (Corning, #2592) were coated with 500 ng/mL recombinant human TGF-β1 (PeproTech) in PBS and incubated overnight at 4°C. The following day, the plates were washed and blocked with 1% bovine serum albumin (BSA) (TOCRIS, #5217) in PBS at room temperature for 2 h. After washing three times, serial 1:2 dilutions of FEBP-sTβRII formats starting from 200 ng/mL were incubated at room temperature for 2 h. Subsequently, 200 ng/mL human TβRII Biotinylated Antibody (R&D Systems, #BAF241) was added to the plate and incubated at room temperature for 1 h. The plates were further washed and incubated with streptavidin-HRP (R&D Systems, #DY998) at room temperature for 20 min. After washing, TMB substrate (R&D Systems, #DY999) was added, and the reaction was stopped with 2N H_2SO_4 (SAMCHUN, #7664-93-9). To assess whether FEBP-sTβRII formats bind to plate-bound FN-EDB, 96-well plates (Corning) were coated with 3 μg/mL of FN-EDB-Fc in PBS and incubated overnight at 4°C. Plates were washed three times with PBS containing 0.05% Tween 20 and blocked with 1% BSA (TOCRIS) in PBS for 2 h at room temperature. After discarding the blocking solution, serial 1:2 dilutions of FEBP-sTβRII were added in duplicate and incubated at 37°C for 2 h. Subsequently, 200 ng/mL of human TβRII biotinylated antibody (R&D Systems) was added and incubated for 1 h at room temperature. After further washing, plates were incubated with streptavidin-HRP (R&D Systems) for 20 min at room temperature. The reaction was developed with TMB substrate and stopped with 2N H_2SO_4. To evaluate simultaneous binding to FN-EDB and TGF-β1 *in vitro*, 96-well ELISA plates (Corning) were coated with 3 μg/mL FN-EDB-Fc in PBS and incubated for 24 h at 4°C. Plates were washed three times with PBS containing 0.05% Tween 20 and blocked with 1% BSA (TOCRIS) in PBS for 2 h at room temperature. Serial 1:4 to 1:8 dilutions of FEBP-sTβRII formats, sTβRII, and control were added and incubated at 37°C for 2 h. After washing, plates were incubated with 0.5 μg/mL biotinylated TGF-β1 (R&D Systems, #NFTG0) for 2 h at room temperature. Plates were washed again and incubated with HRP-conjugated streptavidin (Thermo Fisher Scientific, #21130, 1:10,000 dilution in PBS) for 1 h at room temperature. After washing four times, 100 μL of TMB substrate (R&D Systems) was added to each well, and the reaction was terminated with 2N H_2SO_4. Absorbance in all assays was measured at 450 nm using a microplate reader (Infinite M Plex, TECAN).

TGF-β/SMAD luciferase reporter assay

Cells were transfected with the pGL4.17-CAGA12-Luc vector using PEI (Polyethylenimine, Sigma-Aldrich, #408727). Stably transfected cells were selected by treatment with Geneticin Solution (WELGENE, #LS205-01) at a concentration of 500 μg/mL. The cells carrying the CAGA12-Luc reporter were plated in 48-well plates (SPL Life Sciences, #30048) at a density of 3×10^4 cells per well and incubated overnight at 37°C in a humidified 5% CO_2 atmosphere. Cells were pre-incubated with the FEBP-sTβRII construct or serial dilutions of sTβRII for 30 min, followed by treatment with TGF-β1 (PeproTech; 5 ng/mL) for 12 h. To prepare the samples for luciferase measurement, cell suspensions in 100 μL of PBS were prepared and mixed with 100 μL of 150 μg/mL Luciferase assay reagent (VivoGlo Luciferin, Promega, #P1043) and plates were incubated for at least 5 min at room temperature. Luminescence was measured using a microplate reader (TECAN). RLU, relative unit of normalized firefly luciferase activity to Renilla luciferase activity.

Lentivirus production and transduction

Lentiviruses were produced by cotransfecting HEK293T cells with lenti plasmids expressing Luciferase, the packaging plasmid psPAX2 (Addgene #12260) and the envelope plasmidpMD2G (Addgene #12259), in a ratio of 4:3:1, respectively. Transfection medium was removed 24 h after transfection and fresh medium was added to the plate. Virus-containing medium was collected at 48 h and concentrated using Lenti-X Concentrator (TaKaRa, #631232). PANC02, PKCY, and 4T-1 were seeded 24 h prior to infection and then transduced with virus-containing supernatant supplemented with 8 μg/mL polybrene (Millipore) as shown previously.[79]

In vivo bioluminescence and imaging

An IVIS Spectrum optical scanner (PerkinElmer) was used to acquire the bioluminescence images at 10 min after intraperitoneal injection of D-luciferin (PerkinElmer) in PBS (15 mg/mL) into the animals (10 μL/g body weight). Exposure time was 5 min for the bioluminescence imaging. The imaging system was also used to track Fc fusion protein distribution.

In vivo biodistribution analysis

To investigate the biodistribution, isotype control Fc, sTβRII, and FEBP-sTβRII were labeled with Cy5 dye (Abcam, #ab146456). The Cy5 in DMSO was added to the protein dissolved in sodium bicarbonate buffer using a molar ratio 15:1 of Dye NHS ester-to-protein. The conjugation reactions were performed at room temperature for 1 h with mild stirring. The conjugates were purified chromatographically using a gel filtration column and a phosphate buffer as eluent. The Cy5 conjugated products were concentrated and

the buffer exchanged with PBS. An orthotopic 4T-1-Luc-LMT-2 tumor: *in vivo* fluorescence imaging (PerkinElmer) was performed to track Fc fusion protein distribution. On day 0, 7 days after tumor implantation, orthotopic 4T-1-Luc-LMT-2 tumor-bearing BALB/c mice were subcutaneously treated with Cy5-conjugated mouse IgG1 or human IgG4 control, sTβRII, or FEBP-sTβRII at 10 mg/kg. At 6 days post-injection, mice were sacrificed and a) *ex vivo* Cy5 fluorescence images of tumor as well as organs (brain, heart, lung, liver, bone, spleen, kidney, small (S) intestine, and muscle) were measured. b) Quantification of Cy5-radiance efficiency of tumor as well as organs, with autofluorescence and dye-related artifacts excluded. For Cy5-free detection of construct localization, a separate cohort bearing orthotopic 4T-1-Luc-LMT-2 tumors was intravenously dosed on day 0 with non-labeled mFc sTβRII or FEBP-sTβRII (10 mg/kg). At 6 h post-dose, mice were euthanized and transcardially perfused with ice-cold PBS to remove intravascular signal. Tumors and organs (brain, bone, heart, kidney, liver, lung, skeletal muscle, small intestine) were fixed in 4% paraformaldehyde (2 h, 4°C), cryoprotected in 30% sucrose (overnight), embedded in OCT, and sectioned at 8–10 μm. Cell nuclei were stained with 2 μM DAPI, and tissue-bound constructs were detected using Alexa Fluor 647 goat anti-Mouse IgG (Cell Signaling Technology). Also, mice bearing orthotopic KPC-Luc tumors implanted on day −16 were intravenously treated with sTβRII, FEBP-sTβRII, or mutFEBP-sTβRII at 15 mg/kg, a dose selected based on the efficacy study. Tumors and normal organs were harvested 6 h after injection and subjected to histological analysis. Whole-section images were acquired on Axio scan Z1 slide scanner (Zeiss) under identical exposure and processing settings across groups. Biodistribution measurements obtained from multiple tissues of the same mouse were treated as repeated observations. Data were analyzed by two-way repeated-measures ANOVA with treatment as the between-subject factor and tissue as the within-subject factor, followed by Šidák-adjusted comparisons between FEBP-sTβRII and sTβRII within each tissue.

In vivo time-course analysis for tissue retention

Mice were orthotopically implanted with PANC02-Luc cells and on day 20, after tumor establishment was confirmed by IVIS-based bioluminescence imaging, mice with comparable tumor burden were randomized to receive a single intravenous injection of sTβRII or FEBP-sTβRII (30 mg/kg). At 3, 72, and 144 h post-injection, mice were euthanized and transcardially perfused with ice-cold PBS to remove intravascular signal, and major normal organs and tumor tissues were collected. Tissues were homogenized using a TissueLyser III (Qiagen), followed by protein extraction with T-PER buffer (Thermo Fisher Scientific, #78510) containing protease inhibitor cocktail (Roche, #11836153001). Extracted lysates were stored at −80°C until further analysis. To quantify sTβRII or FEBP-sTβRII in tissue lysates, 96-well plates were coated with 500 ng/mL recombinant human TGF-β1 (PeproTech) overnight at 4°C. Plates were washed with PBST and blocked with blocking/diluent buffer consisting of PBS containing 3% BSA and 0.05% Tween 20 for 2 h at room temperature. After washing, diluted tissue lysates were added and incubated for 2 h at room temperature. Following additional washes, HRP-conjugated goat anti-IgG Fcγ antibody (Jackson ImmunoResearch, #109-035-008) was added and incubated for 1 h at room temperature. After washing, colorimetric reactions were developed using TMB substrate (R&D Systems) and terminated with sulfuric acid. Absorbance was measured using an Infinite 200 Pro plate reader (Tecan), and construct concentrations were calculated by interpolation from standard curves using GraphPad Prism software. After correction for dilution factors, calculated concentrations were normalized to tissue weight and expressed as ng/mg tissue. To compare tissue retention kinetics across organs with different initial exposure levels, concentrations at 72 and 144 h were normalized to the corresponding 3-h concentration for each tissue.

Depletion of immune-cell populations and IFN-γ neutralization

Control and FEBP-sTβRII were administered every 5 days for a total of nine doses, starting on day 7, in the PANC02-Luc orthotopic tumor model. For immune-cell depletion, mice received intraperitoneal injections of anti-CD4 antibody (clone YTS191; 150 μg) or anti-CD8 antibody (clone 53-6.7; 150 μg) 1 day before the first dose of FEBP-sTβRII (20 mg/kg), followed by additional injections every 5 days for a total of six doses. For IFN-γ neutralization, mice received intraperitoneal injections of anti-IFN-γ antibody (clone XMG1.2; 500 μg) 1 day before the first dose of FEBP-sTβRII, followed by additional injections every 5 days for a total of six doses. All antibodies were purchased from Bio X Cell.

Tumor progression was monitored on days 5, 13, 20, 34, and 48 using *in vivo* bioluminescence imaging with the IVIS Lumina system (PerkinElmer). A separate cohort of C57BL/6J mice ($n = 5$ per group) received PBS, anti-CD4, anti-CD8, or anti-IFN-γ antibodies on days 6, 11, and 16. $CD4^+$ and $CD8^+$ T cell depletion was verified by flow cytometric analysis of peripheral blood collected by retro-orbital bleeding, and IFN-γ neutralization was assessed by measuring serum IFN-γ levels, 3 days after the final antibody injection.

Tumor tissue TGF-β1 measurement

Levels of TGF-β1 in tumor tissues were measured using the Mouse TGF-β1 DuoSet ELISA kit (R&D Systems, #DY1679) according to the manufacturer's instructions, with modifications in sample preparation. Briefly, 96-well ELISA plates were coated with 2 μg/well of mouse TGF-β1 capture antibody in PBS and incubated overnight at 4°C. After washing and blocking with TBST for 1 h at room temperature, tumor lysates (50 μg/mL) and standards, diluted in 1.4% Reagent Diluent Concentrate 1 (R&D Systems, #DY997) with PBST, were added without acid activation and incubated for 2 h at room temperature. Subsequent steps, including incubation with biotinylated detection antibody, Streptavidin-HRP, and signal development with TMB substrate (R&D Systems), were performed according to the manufacturer's protocol. Absorbance was measured at 450 nm using an Infinite M Plex reader (TECAN).

Immunohistochemistry analysis

Tissues were fixed for 24 h in 4% PFA and stored in 70% ethanol until further processing. Five-micrometer sections of formalin-fixed, paraffin-embedded tissues were deparaffinized with xylene, rehydrated, and subjected to antigen retrieval with heated antigen unmasking solution (1.0 mM EDTA, 0.05% Tween 20, pH 8.0). After 1 h in horse serum blocking buffer, primary antibodies were applied for 3 h at room temperature or overnight at 4°C. Anti-phospho-SMAD2/3 (S465/467 and S423/425, 1:100, Invitrogen, #PA5-110155), anti-CD8a (1:50, Invitrogen, #14-0808-82), Anti-CD31 (1:200, EPR17259, abcam, #ab182981), anti-HLA-Pan (1:200, NeoBiotechnologies, #MSM2-3475) and Anti-H2-Ab1 (1:250, Abclonal, #A24650) were used. Detection was carried out with anti-Mouse, anti-rabbit, or anti-Rat secondary antibodies conjugated to biotin (VECTASTAIN Elite ABC-HRP Kit), and visualized using DAB substrate (Splink HRP Rabbit DAB Detection kit). Images were acquired with an Axio scan Z1 slide scanner (Zeiss). Quantitative analyses were performed using QuPath[74] software (v0.7.0). Cells were segmented using InstanSeg[80] and classified with a Random Trees object classifier as described above. The proportion of positive cells was expressed relative to the total number of segmented cells. Digital Histoscore for H2-Ab1 and pan-HLA expression was determined using positive cell detection, with predefined DAB intensity thresholds for 1+/2+/3+ classes applied uniformly across all samples (Σ intensity level [1–3] $\times$ percentage of cells in that class; range 0–300).

ROI definitions for tumor-edge and tumor-interior analyses

Because immune-excluded tumors exhibit marked spatial heterogeneity, tumor-edge and tumor-interior regions were quantified separately for all α-SMA, CD8, and *p*-SMAD2/3 analyses. Tumor-edge ROIs were defined as viable tumor regions located within approximately 0–400 μm of the invasive tumor boundary, stromal capsule, tumor–stroma interface, or outer desmoplastic margin. Tumor-interior ROIs were defined as viable tumor regions located more than 400 μm from the tumor boundary and spatially separated from the invasive margin. Necrotic areas, hemorrhagic regions, large vessels, tissue folds, cautery artifacts, and poorly preserved tissue areas were excluded from the analysis. For each tumor, at least three non-overlapping tumor-edge ROIs and three non-overlapping tumor-inside ROIs were analyzed. When tumor size allowed, $\geq$3 ROIs per region were quantified. ROI size was kept constant within each staining experiment and magnification. The same tumor ROI definitions were also applied to quantification of CD31, HLA-Pan, and H2-Ab1 staining, where indicated. Quantification was performed by an investigator blinded to the treatment group whenever possible.

Immunofluorescence staining for tissues and cells

Tissues were frozen in OCT medium (Sakura Finetek) and cut into 10-μm sections. Tumor sections were fixed and stained with antibodies and mounted with Vectashield anti-fade mounting media (Vector Laboratories). Rat anti-CD8a (1:100, Invitrogen, #14-0808-82), rabbit anti-hCD8a (1:100, Abcam, #ab316778) and rabbit anti-α-SMA (1:300, Abcam, #ab7817) were used. The secondary antibodies were produced in either donkey or goat and targeted against mouse and rabbit (Cell Signaling Technology), and human (Invitrogen) with conjugation to Alexa Fluor 488, 555 or 647. To detect FEBP-sTβRII formats on tumor, tissue sections were stained using a secondary antibody specific to the appropriate species. *KP*-PSAFs were washed in PBS and fixed in 3% paraformaldehyde for 5 min. Cells were permeabilized with PBS containing 0.25% Triton X-100 (Sigma-Aldrich, #T8787) for 10 min. After washing 3 times with PBS to remove the permeabilization buffer, cells were blocked with 1% BSA (TOCRIS) in PBST (0.01% Triton X-100) for 1 h. Anti-fibronectin (Abcam, #ab2413) was used at a 1:100 dilution as the primary antibody and incubated at 4°C overnight. As the secondary antibody, Alexa Fluor 488 Goat anti-Rabbit IgG (Cell Signaling Technology, #4408S) was used and it was treated at room temperature for 1 h. Cell nuclei were stained with 2 μM DAPI. In the case of FEBP-sTβRII (200 μg/mL), Alexa Fluor 647 Goat anti-Human IgG (Invitrogen, #A21445) was used at a 1:100 dilution. Images were acquired with an Axio scan Z1 slide scanner (Zeiss) or LSM800 confocal microscope (Zeiss). QuPath software (v0.7.0) was used for quantitative image analysis.[74] Cells were segmented using InstanSeg[81] implemented through the Deep Java Library extension with a PyTorch[82] backend. $CD8^+$ cells were identified using a Random Trees object classifier trained on representative annotated cells and applied uniformly across all images. The proportion of $CD8^+$ cells was calculated as the percentage of $CD8^+$ cells among total segmented cells. Spatial density maps were generated from $CD8^+$ cell centroids by calculating summed cell counts within a 200 μm radius and visualized using a jet colormap. α-SMA^+ area was quantified using a pixel classifier trained on the α-SMA channel and applied uniformly across all samples, and expressed as the percentage positive area of annotated tissue. For each mouse tumor, at least three ROIs from the tumor edge and inside regions were analyzed, and the averaged value was used as a single biological replicate for statistical analysis. $CD8^+$ cells were quantified as the percentage of total cells, whereas α-SMA was quantified as the percentage of ROI area.

The primary and secondary antibodies used in immunofluorescence and immunohistochemistry are listed in the key resources table.

Quantitative PCR with reverse transcription

Total RNA from tissues or cells was extracted with Hybrid-R (GeneAll, #305-101). Isolated RNA was quantified using NanoDrop 8000 Spectrophotometer (Thermo Fisher Scientific). To synthesize cDNA, reverse transcription was performed using the PrimeScript RT Master Mix (TaKaRa, #RR036A) with 50 ng/μL of isolated RNA. Gene expression levels of EDB_Ex24-25 (Mm.PT.58.5160215) were quantified by qPCR using TaqMan probes and Gene Expression Master Mix (Applied Biosystems, #4369016), with expression levels normalized to the housekeeping gene 18S rRNA (Hs.PT.39a.22214856.g). qPCR for antigen-presentation-related genes was performed using the iTaq Universal SYBR Green Supermix (Bio-Rad, #1725121) according to the manufacturer's protocol, and relative

expression was normalized to Actb (β-actin) or Gapdh. All qPCR reactions were run on a QuantStudio 5 Real-Time PCR System (Applied Biosystems). Relative gene expression was calculated using the $2^{-\Delta\Delta Ct}$ method, and all primers used in this study are listed in Table S1J. Statistical analyses were performed on log2-transformed data using two-sided Welch's t-tests with Holm–Šidák adjustment for multiple comparisons.

Bulk RNA-seq library preparation and data processing

Tumors and matched peripheral whole blood were collected from PANC02-Luc tumor-bearing mice treated with control, sTβRII, or FEBP-sTβRII. The source therapeutic cohort contained $n = 10$ mice per group for sample collection, and $n = 3$ representative biological replicates per group were sequenced for the primary tumor/PWB RNA-seq analysis unless otherwise indicated. Tumors were harvested at day 35, snap-frozen or stabilized in RNA-preserving reagent, and homogenized. Peripheral whole blood was collected into RNA-stabilizing or anticoagulant-containing tubes and processed for total RNA extraction. For KPC validation RNA-seq, tumors from control, sTβRII, and FEBP-sTβRII-treated mice were collected at day 20. $n = 3$ biological replicates per group were sequenced.

Total RNA from tumors was extracted using Hybrid-R (GeneAll #305-101). PWB RNA was purified with the RiboPure RNA Purification Kit, blood (Invitrogen #AM1928). Libraries were prepared with the TruSeq Stranded Total RNA kit with Ribo-Zero H/M/R (Illumina) and sequenced as paired-end 2 × 151 bp on a NovaSeq 6000 after qPCR QC. Reads with mean base quality ≥ Q20 were aligned to the Mus musculus reference GRCm38 (Ensembl Release 99) using STAR v2.4.0b.[56] Gene-level counts were generated with RSEM v1.3.1.[57] Protein-coding genes with TPM ≥0.5 in at least one condition were retained.

Differential expression and pathway analysis of bulk RNA-seq data

Differential expression analysis was performed using DESeq2 (v1.44).[58] For the PANC02 orthotopic model, genes with $p < 0.01$ and |fold change (FC)| ≥ 1.5 in the sTβRII versus control and FEBP-sTβRII versus control comparisons were considered differentially expressed. Based on their expression patterns, DEGs were classified into three groups: sTβRII & FEBP-sTβRII common genes (altered in both comparisons), greater-altered in FEBP-sTβRII genes (common genes with |FC| ≥ 1.5 in sTβRII versus control and additional changes in FEBP-sTβRII versus sTβRII with |FC| ≥ 1.25), and FEBP-sTβRII-specific genes (identified only in the FEBP-sTβRII versus control comparison). Candidate genes were further selected based on Z-score-normalized expression patterns.

For the KPC orthotopic model, DEGs were identified using an adjusted p-value (Padj) < 0.01 and |FC| > 2. Because transcriptional differences between control and sTβRII-treated tumors were limited, DEGs were classified into two categories: FEBP-sTβRII-specific genes (1), which were differentially expressed in both FEBP-sTβRII versus control and FEBP-sTβRII versus sTβRII comparisons, and greater-altered genes (2), which were identified only in the FEBP-sTβRII versus control comparison.

For PWB, DEGs were identified in the sTβRII versus control and FEBP-sTβRII versus sTβRII comparisons using a stringent cutoff ($p < 0.01$ and |FC| ≥ 1.5). To capture subtle peripheral transcriptional responses, an exploratory analysis was additionally performed using a mild cutoff ($p < 0.05$ and |FC| ≥ 1.25), followed by filtering based on Z-score-normalized expression patterns. Expression patterns were visualized as hierarchical heatmaps in MeV (Manhattan correlation; complete linkage).[59]

Gene Ontology enrichment analysis was performed using DAVID (EASE <0.05). Differentially expressed genes from tumor tissues and PWB are provided in Table S1. Gene set enrichment analysis (GSEA, v4.4.4) was performed by comparing FEBP-sTβRII-treated tumors with the remaining groups (control and sTβRII) or sTβRII-treated tumors with the remaining groups (control and FEBP-sTβRII). See also Table S1.

Single-cell RNA-seq preprocessing, integration, and clustering

Fresh tumors were minced and enzymatically dissociated under RNase-free conditions, filtered to remove debris and doublets, and red blood cells were lysed. scRNA-seq libraries were subsequently generated following the manufacturer's protocol (10× Genomics), which includes reverse transcription, cDNA amplification, and library construction using the Chromium GEM-X Single Cell 3′ Kit v4 (10× Genomics, PN1000691). The quality and size distribution of the resulting cDNA and final libraries were assessed, and concentrations were quantified. Libraries were sequenced on a NovaSeq 6000 platform (Illumina) using a paired-end configuration, with read lengths structured to capture the cell barcode, Unique Molecular Identifier (UMI), and the transcript sequence. Raw fastqs were processed with CellRanger (v9.0.1)[83] against GRCm38 (Ensembl Release 99) to produce gene–barcode matrices. To reduce ambient RNA, matrices were denoised with CellBender remove-background (v0.3.2)[65] using dataset-specific expected-cell settings. Putative doublets were identified with Scrublet (v0.2.3)[66] and excluded according to dataset-specific thresholds inferred from simulated distributions. Analyses were performed in Scanpy (v1.10.4)[67] using the AnnData framework. Cells were filtered according to standard quality-control criteria: those with fewer than 200 or more than 7,000 detected genes were excluded to remove low-complexity barcodes and potential multiplets; cells with fewer than 1,000 total UMI counts were discarded as low-quality. In addition, cells in which more than 20% of transcripts mapped to mitochondrial genes were removed to avoid artifacts derived from stressed or dying cells. Count matrices were library-size normalized to a target depth of 10,000 UMIs per cell and log-transformed. Highly variable genes (HVGs) were identified using a batch-aware procedure (batch_key = 'Sample'); all other parameters were left at defaults. Across the combined dataset, 5,000 HVGs were retained for downstream analyses. Expression matrices were scaled prior to PCA, for which 50 components were retained. To account for batch effects across libraries, a batch-balanced k-nearest neighbor graph was constructed using BBKNN (v1.6.0).[68] Clustering was performed on the corrected neighbor graph using the Leiden algorithm with a resolution parameter tuned empirically for biological separability and cluster stability. For visualization, two-dimensional embeddings were generated with UMAP (min_dist = 0.5).

Cell type annotation and pseudobulk expression analysis

Ten major lineages: T-cells, B-cells, NK-cells, macrophages/monocytes (Macro/Mono), dendritic cells (DC), myeloid-derived suppressor cells (MDSC), cancer-associated fibroblasts (CAFs), epithelial cells (Epi), endothelial cells (EC), and red blood cells (RBC) were annotated using curated markers and cluster-specific differential expression. Each lineage was then re-embedded for subclustering. For lineage-level comparisons, pseudobulk expression profiles were generated by summing raw counts of cells grouped by sample and cell type. Aggregated matrices were library-size normalized and scaled to per-gene z-scores for visualization and comparative analyses across lineages.

scRNA-seq differential expression and functional enrichment

Differential expression within T-cells was assessed using the rank_genes_groups function in Scanpy (Wilcoxon rank-sum test, Benjamini-Hochberg FDR correction; default). Genes with FDR <0.01 and $|\log_2 FC| \geq 0.5$ were defined as DEGs. For downstream GO enrichment, up- and down-regulated DEGs were submitted to DAVID. GO terms with an EASE score <0.05 were considered significantly enriched. See also Table S2.

Cell–cell communication analysis

Ligand–receptor interactions were inferred using the CellPhoneDB method within the LIANA framework (v1.5.1).[69] The analysis was performed on a normalized expression matrix with curated cell-type annotations. Interactions with a permutation-based $p < 0.05$ and mean expression >0 in both interacting cell types were considered significant and retained for downstream analysis.

Significant interactions among major immune populations, CAF subtypes, and epithelial cells were categorized into TGF-β-direct inhibitory, immune-stimulatory, and compensatory/immune-inhibitory communication programs. Representative interactions and complete ligand–receptor pairs are provided in Table S2.

GTEx to TCGA comparison

GTEx and TCGA (normal and primary tumor only) total gene and transcript RNA-seq datasets were obtained from UCSC Xena (https://xena.ucsc.edu/)[72] and were used for pan-normal and cancer analysis of whole *FN1* mRNA expression and four *FN1-EDB* mRNA isoform expression.

Human immunotherapy cohorts

Publicly available transcriptomic datasets from patients treated with immune checkpoint blockade were used for cross-cohort validation analyses. The metastatic pancreatic ductal adenocarcinoma (PDAC; $n = 17$) and microsatellite-stable colorectal cancer (MSS-CRC; $n = 26$) cohorts were obtained from GSE179351. Pretreatment samples included both pre-Tx and pre-xRT biopsies. Pre-xRT biopsies were collected after one cycle of ipilimumab (anti-CTLA-4) plus nivolumab (anti-PD-1) and prior to radiation therapy. The metastatic gastric cancer (mGC) cohort (Kim cohort; $n = 45$) consisted of patients treated with anti-PD-1 therapy, whereas the melanoma cohort (Gide cohort; $n = 32$) consisted of patients treated with combined anti-PD-1 and anti-CTLA-4 therapy. Processed expression matrices and clinical annotations for these cohorts were obtained from the Tumor Immune Dysfunction and Exclusion (TIDE) database (http://tide.dfci.harvard.edu/download/). For all cohorts, only pretreatment samples were included. GSVA scores were calculated using mouse-derived signatures after conversion to human orthologs, and their associations with each other and with clinical responses were evaluated across cohorts.

Signature generation and GSVA analysis

Cell type-specific signatures were derived from PANC02 scRNA-seq analyses and further refined based on concordant expression patterns observed in bulk RNA-seq datasets. The myoCAF signature (*CLIC4*, *ACVR1*, *BMPR1A*, *LMO7*, *ITGB4*, *HS2ST1*, *ITGA6*, *FLNB*, *VDR*, and *FOXP1*) represented TGF-β-driven myofibroblastic programs that were reduced following FEBP-sTβRII treatment. The CD8-Teff signature (*CD8B*, *NKG7*, *GZMB*, *GZMK*, *CCL5*, *CCR5*, and *CD226*), MHC-II$^+$-Macro signature (*CXCL9*, *FCGRT*, *LST1*, *DAP10*, *FPR1*, *CX3CR1*, and *MS4A7*), and *Dcn*$^+$-apCAF signature (*HLA-DRA*, *CD74*, *HLA-DRB1*, *HLA-DPA1*, *HLA-DPB1*, *CD80*, *PDGFRA*, *ICOSL*, *CD40*, *SELK*, *IFNG*, *CIITA*, and *HLA-DQB1*) comprised genes associated with cytotoxic effector T-cells, antigen-presenting inflammatory macrophages, and antigen-presenting CAFs with immune-interacting properties, respectively, and were enriched following FEBP-sTβRII treatment. Treatment-associated changes in each signature were confirmed by pseudobulk analyses within the corresponding cell populations. Mouse genes were converted to human orthologs, and GSVA scores[62] were calculated using the GSVA package.

QUANTIFICATION AND STATISTICAL ANALYSIS

Statistical analysis

Statistical analyses were performed using Prism software (v10.1.2; GraphPad). The experimental unit and statistical model were defined according to the corresponding experimental design. Comparisons between two independent groups were performed using two-tailed unpaired Student's *t*-tests or unpaired Welch's *t*-tests, as appropriate. For comparisons among multiple groups, one-way or two-way ANOVA followed by Šidák's or Tukey's multiple comparisons test was used as appropriate.

For experiments in which multiple measurements were obtained from the same mouse, repeated-measures ANOVA was used to account for within-subject dependence. For repeated-measures datasets for which a mixed-effects framework was appropriate, including those containing incomplete observations, mixed-effects analysis was used to account for within-subject dependence.

Where substantial heterogeneity of variance and/or mean-dependent variability was observed, square-root, log2, or log10 transformation was applied before statistical analysis, as indicated in the corresponding figure legends. For datasets showing substantial heterogeneity of variance, prespecified pairwise comparisons were performed using unpaired Welch's *t*-tests followed by Šidák adjustment for multiple comparisons. Multiple-comparison families were defined according to the prespecified biological comparisons within each analysis.

Survival analyses were performed using the log-rank (Mantel–Cox) test, with Holm–Šidák adjustment for multiple prespecified pairwise comparisons where applicable. Spearman's rank correlation coefficient was used to assess correlations. Data are presented as mean ± SD, as indicated. Statistical significance was defined as $p < 0.05$.

For bulk RNA-seq analysis, gene counts were quantified using RSEM (v1.3.1),[57] and differential expression analysis was performed using DESeq2 (v1.44)[58] with the Wald test. For single-cell RNA-seq analysis, raw FASTQ files were processed using CellRanger (v9.0.1),[83] and differential gene expression analysis was performed using Scanpy (v1.10.4)[67] with the sc.tl.rank_genes_groups function and the Wilcoxon method. Ligand–receptor interactions were inferred using CellPhoneDB with permutation testing (1,000 iterations).

For digital pathology, each biological replicate corresponded to one mouse tumor. Multiple ROIs from the same tumor were treated as technical fields and averaged to generate one biological replicate value per mouse before group-level statistical analysis, unless otherwise specified. For flow cytometry, each tumor or blood sample was treated as one biological replicate. For *in vitro* ELISA, reporter, binding, and co-culture assays, biological and technical replicate numbers are specified in the figure legends or the STAR Methods subsections.